ARISTOTLE UNIVERSITY OF THESSALONIKI
Interinstitutional Program of Postgraduate Studies in
PALEONTOLOGY – GEOBIOLOGY

STYLIANOS KOUTALIS
Geologist

A VIRTUAL RECONSTRUCTION OF THE DEFORMED DFN3-150 EARLY PLEISTOCENE *Paradolichopithecus* CRANIUM FROM DAFNERO-3, GREECE

MASTER THESIS

DIRECTION: Macropalaeontology
Directed by: Aristotle University of Thessaloniki

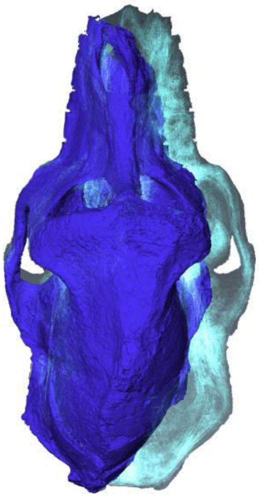

THESSALONIKI
2022

Interinstitutional
Program of
Postgraduate
Studies in
PALAEONTOLOGY – GEOBIOLOGY

supported by:

SCHOOL OF GEOLOGY A.U.TH.

Τμήμα Γεωλογίας ΑΠΘ
School of Geology AUTh

school of biology

Τμήμα Βιολογίας ΑΠΘ
School of Biology AUTh

National and
Kapodistrian
University of Athens
Faculty of Geology and
Geoenvironment

Τμήμα Γεωλογίας & Γεωπεριβάλλοντος
ΕΚΠΑ
School of Geology & Geoenvironment
NKUA

Department of GEOLOGY

Τμήμα Γεωλογίας Παν/μίου Πατρών
School of Geology, Patras Univ.

UNIVERSITY OF THE AEGEAN

Τμήμα Γεωγραφίας Παν/μίου Αιγαίου
School of Geography, Aegean Univ.

In collaboration with:

EBERHARD KARLS
UNIVERSITÄT
TÜBINGEN

EBERHARD KARLS
University
of Tuebingen, Germany

1431
Université
de Poitiers

University of Poitier, France

STYLIANOS KOUTALIS
ΣΤΥΛΙΑΝΟΣ ΚΟΥΤΑΛΗΣ
Πτυχιούχος Γεωλογίας

A VIRTUAL RECONSTRUCTION OF THE DEFORMED DFN3-150 EARLY PLEISTOCENE *Paradolichopithecus* CRANIUM FROM DAFNERO-3, GREECE

ΨΗΦΙΑΚΗ ΑΝΑΚΑΤΑΣΚΕΥΗ ΤΟΥ ΠΑΡΑΜΟΡΦΩΜΕΝΟΥ ΚΡΑΝΙΟΥ DFN3-150 ΤΟΥ ΚΑΤΩ-ΠΛΕΙΣΤΟΚΑΙΝΙΚΟΥ *Paradolichopithecus* ΑΠΟ ΤΗΝ ΘΣΗ ΔΑΦΝΕΡΟ-3, ΕΛΛΑΔΑ

Υποβλήθηκε στο ΔΠΜΣ Παλαιοντολογία-Γεωβιολογία

Ημερομηνία Προφορικής Εξέτασης:05/05/2022
Oral Examination Date: 05/05/2022

Three-member Examining Board

Professor Dimitrios Kostopoulos, Supervisor
Professor Katerina Harvati-Papatheodorou, Member
Researcher A’ Dr. Frank Guy, Member

Τριμελής Εξεταστική Επιτροπή

Καθηγητής Δημήτριος Κωστόπουλος, Επιβλέπων
Καθηγήτρια Κατερίνα Χαρβάτη-Παπαθεωδώρου, Μέλος Τριμελούς Εξεταστικής Επιτροπής
Ερευνητής Α’ Δρ. Frank Guy, Μέλος Τριμελούς Εξεταστικής Επιτροπής

External Assistant/ Εξωτερικός Συνεργάτης (σύμφωνα με ΕΔΕ5/ 15-7-2019)
Carolin Röding, M.Sc.

Cover figure: LGPUT DFN3-150 *and its warped mirror ghost superimposed. Dorsal view. Unscaled.*

A VIRTUAL RECONSTRUCTION OF THE DEFORMED DFN3-150 EARLY PLEISTOCENE *Paradolichopithecus* CRANIUM FROM DAFNERO-3, GREECE – *Master Thesis*

ΨΗΦΙΑΚΗ ΑΝΑΚΑΤΑΣΚΕΥΗ ΤΟΥ ΠΑΡΑΜΟΡΦΩΜΕΝΟΥ ΚΡΑΝΙΟΥ DFN3-150 ΤΟΥ ΚΑΤΩ-ΠΛΕΙΣΤΟΚΑΙΝΙΚΟΥ *Paradolichopithecus* ΑΠΟ ΤΗΝ ΘΕΣΗ ΔΑΦΝΕΡΟ-3, ΕΛΛΑΔΑ – *Μεταπτυχιακή Διπλωματική Εργασία*

Citation:
Koutalis, S., 2022. – A virtual reconstruction of the deformed DFN3-150 Early Pleistocene *Paradolichopithecus* cranium from Dafnero-3, Greece. Master Thesis, Interinstitutional Program of Postgraduate Studies in Palaeontology-Geobiology. School of Geology, Aristotle University of Thessaloniki, 84pp.

CONTENTS

ACKNOWLEDGMENTS

ABSTRACT

ΠΕΡΙΛΗΨΗ

ABBREVIATIONS

BIBLIOGRAPHY

SUPPLAMENTARY MATERIAL

ACKNOWLEDGMENTS

To begin with, it would be an enormous omission not to memorize in the first place my supervisor, Department Director Prof. Dr. Dimitrios Koustopoulos for giving me the chance to be one of his students. His patience, good spirits and constant support was more than vital, and even extends beyond the straight academic concept, as was witnessed by all of us under his instructions. The same amount of enthusiasm should of course be attributed to the rest of LGPUT members, for their hospitality, advice and support would follow each step of my presence here, from classes to Laboratory.

I would also like to personally thank the other members of the examination board, Prof. Dr. Katerina Harvati-Papatheodorou for giving me the chance to visit University of Tuebingen and granted me access to Senckenbergs' laboratory facilities. Without her kind invitation this introductory work wouldn't be able to start at all. In respect to this, I would like to mention and sincerely thank researcher Dr. Frank Guy from PALEVOPRIM, University of Poitier, CNRS. The fossil studied was unearthed in collaboration with members of the PALEVOPRIM, and access to the fossil was partly granted by them. Adding on, his, and PALEVOPRIM Labory Directors' Dr. Gildas Merceron first look and evaluation on the models extracted were significant.

It would be unfair in turn to neglect Dr. Giorgos Konidaris for his support during my stay in Tuebingen. His hospitality, advice, and overall assistance created an appropriate environment and for that I am grateful. He was also to find and share Prof. Connoly's (1950) Michigan University's e-text reprint. Gratitude should also be attributed to my brother Rafael, as well as to my flatmate Christos Vergidis for their unconditional support and help. I hope the "outcome" of this effort will satisfy them. I also thank Krystallia Chitoglou, M.Sc., a fellow student of mine, who was a companion through this entire Master's Program, and assisted me on editing plates and figures, as well as Dr. C. A. Plastiras, for sharing his time with me talking on matters of my thesis and paleontology in general.

Finally, I want to notably mention Carolin Röding, M.Sc. from University of Tuebingen. Her assistance was constant from the very begining to the very end, and she was always willing to contribute to the best degree possible when she was called upon. Without her help and instructions, this work would not be able to be accomplished. That for, these models presented here are partly hers. Thank you Carol. For all those I forgot to mention I sincerely apologize. It was a great great time.

ABSTRACT

The present thesis deals with the virtual reconstruction of the Early Pleistocene LGPUT DFN3-150 *Paradolichopithecus* aff. *arvernensis* deformed cranium from Dafnero-3 site, Greece. The tessellated presence of the *Paradolichopithecus* species across Eurasia in the Early Pleistocene and its abrupt disappearance from the record in the late Early Pleistocene, places the studied cranium in the front of paleontological interest, both in a taxonomical and evolutionary context.

It has been more than a hundred years since Wilhelm C. Röntgen introduced X-rays to the public, and a little less than a generation that Computed Tomography was exploited for the reconstruction of fossil crania. A brief description of the history, the principles and configurations that allowed the present workflow to be a well-established framework of research is provided. Here, utilizing two basic principles of skeletal biological samples, namely bilateral symmetry and smoothness of a craniums' initial outer surface curvature, LGPUT DFN3-150 was firstly submitted to the segmentation process in Avizo® 9.2.0 Lite and Avizo® 7.0.0 (Visualization Sciences Group).

The segmentation procedure applies directly on CT data, and allows to separate the sediment matrix from the bone, as well as to divide the latter in different groups, namely labels. Then, those labels can be manipulated independently, thus any examined structure can be restored by repositioning the fragments. For LGPUT DNF3-150 cranium, twenty-five fragments where extracted from the initial fossil, but not all are result of clear breakage. Most of them were segmented in preserved sutures or in some cases partially following sutures.

In order to eliminate syn- and post-burial deformation, and in parallel to study the results of different tactics on the reconstruction, three virtual models were created. The first two deal with minimizing the effect that deformation had on the right side of the cranium, by correcting the displacement of the right maxillary fragment. The third model constitutes a mirror reconstruction were all left fragments were duplicated. Then, following a sagittal relocation of the left frontal fragment and its mirrored counterpart, the rest of the left fragments followed the position acquired in the previous two models.

When the reconstructions are considered in relation to the original fossil, the most evident difference is the new width. This may have an effect on foramen magnum shape, giving it a more circular contour. This is observed in all three reconstructions provided. In terms of deformation, between the original and the mirror model, it is clear that the later differentiates in the shape of the supraorbital torus, and its curved contour is a matter of discussion, whether it is a valuable morphological signal or rather an effect of the plastic deformation that couldn't be eliminated by the currently used techniques.

Concluding, a thorough application of retrodeformation methods could be more useful in providing a solid shape restoration for LGPUT DFN3-150, since plastic deformation accounts for the majority of the syn- and post-burial damage of this fossil.

ΠΕΡΙΛΗΨΗ

Η παρούσα εργασία ασχολείται με την ψηφιακή ανακατασκευή του παραμορφωμένου κρανίου LGPUT DFN3-150 του Κάτω Πλειστοκαινικού *Paradolichopithecus* aff. *arvernensis* της θέσης Δαφενρό-3, Ελλάδα. Η αποσπασματική παρουσία του *Paradolichopithecus* στην Ευρασία στο Κάτω Πλειστόκαινο και η απότομη εξαφάνιση του από το αρχείο απολιθωμάτων στα τέλη του Κάτω Πλειστοκαίνου, τοποθετεί το παρόν κρανίο στο κέντρο του παλαιοντολογικού ενδιαφέροντος, τόσο σε ταξινομικό όσο και εξελικτικό επίπεδο.

Έχουν περάσει περισσότερα από εκατό χρόνια από όταν ο Wilhelm C. Röntgen εισήγαγε τις ακτίνες Χ στο κοινό, και λιγότερο από μια γενιά που η αξονική τομογραφία αξιοποιήθηκε στην ανακατασκευή απολιθωμένων κρανίων. Παρέχεται μια σύντομη περιγραφή της ιστορίας, των αρχών και των μηχανισμών που επιτρέπουν στο εργασιακό οργανόγραμμα να αποτελεί ένα καλώς διαμορφωμένο πλαίσιο έρευνας. Αξιοποιώντας δύο βασικές αρχές της βιολογίας σκελετικών δειγμάτων στην παρούσα εργασία, την πλευρική αμφισυμμετρία και την αρχικά ομαλή ακολουθία καμπύλωσης των εξωτερικών επιφανειών των κρανίων, το LGPUT DFN3-150 υποβλήθηκε αρχικά στην διαδικασία της «κατάτμησης», στο υπολογιστικό περιβάλλον των εφαρμογών Aviso® 9.2.0 Lite και Aviso® 7.0.0 (Visualization Sciences Group).

Η διαδικασία αυτή εφαρμόζεται απευθείας στα δεδομένα της αξονικής τομογραφίας, επιτρέποντας τον διαχωρισμό του ιζήματος από τα οστά, όπως επίσης την διαίρεση του οστού σε διαφορετικές ομάδες. Οι ομάδες θα μπορέσουν στη συνέχεια να διαχειριστούν αυτόνομα, ώστε οποιαδήποτε δομή να μπορεί να ανακατασκευαστεί επανατοποθετώντας τα επιμέρους τμήματά της. Για το LGPUT DFN3-150 διαχωρίστηκαν είκοσι πέντε τμήματα από το αρχικό απολίθωμα, αλλά δεν αποτελούν όλα προϊόντα πλήρους διάρρηξης. Τα περισσότερα από αυτά σχεδιάστηκαν και «αποσπάσθηκαν» ψηφιακά μεταξύ διατηρημένων ραφών, ή ακολουθώντας κάποιες ζώνες ραφών.

Για να μειωθεί η διαγενετική συν- και μετά-ταφική παραμόρφωση, ενώ παράλληλα να μελετηθούν τα αποτελέσματα εφαρμογής διαφορετικών τακτικών ανακατασκευής, δημιουργήθηκαν τρία μοντέλα. Τα πρώτα δύο αναφέρονται στην προσπάθεια ελαχιστοποίησης της παραμόρφωσης στη δεξιά πλευρά του κρανίου, διορθώνοντας την μετατόπιση που υπέστη η δεξιά άνω γνάθος. Το τρίτο μοντέλο αποτελεί ένα μοντέλο «αντικατοπτρισμού» όπου όλα τα θραύσματα της αριστερής πλευράς αντιγράφηκαν και αναστράφηκαν. Έπειτα, ακολουθώντας την επανατοποθέτηση του αριστερό μετωπικού θραύσματος με το αντίγραφό του, σε ένα οβελιαίο επίπεδο συμμετρίας, τα υπόλοιπα θραύσματα επανατοποθετήθηκαν ακολουθώντας την θέση τους στο άλλα δύο μοντέλα.

Όταν αυτά τα μοντέλα αντιπαραβάλλονται με το αρχικό απολίθωμα, η εντονότερη διαφορά έγκειται στο νέο διευρημένο πλάτος. Αυτό επηρεάζει το σχήμα του ινιακού τρήμματος, προσδίδοντάς του ένα πιο κυκλικό περίγραμμα, χαρακτήρας που παρατηρείται και στα τρία μοντέλα. Σχετικά με την παραμόρφωση μεταξύ του αρχικού απολιθώματος και του μοντέλου αντικατοπτρισμού, το τελευταίο διαφοροποιείται στο σχήμα της υπερόφριας ακρολοφίας, το καμπύλο περίγραμμα της οποίας συνιστά ένα θέμα προς συζήτηση, κατά πόσο δηλαδή αποτελεί αυθεντικό μορφολογικό χαρακτήρα ή είναι το προϊόν της πλαστικής παραμόρφωσης που δεν μπορούσε να εξαλειφθεί με τις παρούσες τεχνικές.

Καταλήγοντας, μια ενδελεχής εφαρμογή μεθόδων «αντιστροφής» της παραμόρφωσης θα ήταν χρήσιμη για την εξαγωγή ενός πλήρως ανακατασκευασμένου μοντέλο του LGPUT DFN3-150 καθώς η πλαστική παραμόρφωση ευθύνεται για την πλειονότητα της συν- και μετά-ταφικής επίδρασης στο απολίθωμα.

ABBREVIATIONS

LGPUT	Laboratory of Geology and Paleontology, University of Thessaloniki
DFN	Dafnero
MSC	Messinian Salinity Crisis
CT	Computed Tomography
GM	Geometric Morphometrics
μCT	micro Computed Tomography
DEL	Detector Element
2-3-4D	two-three-four Dimensional
CBCT	Cone Beam Computer Tomography
HU	Hounsfield Units
MC	Marching Cubes

CHAPTER 1. INTRODUCTION

Aim of this master thesis is to consolidate a new basis of research and to contribute to the ongoing study and interpretation of the ecological and taxonomic affinities of the cranium LGPUT DFN3-150 of *Paradolichopithecus* aff. *arvernensis* Necrasov et al., 1961 from the Lower Pleistocene fossil site of Dafnero (NW Greece) (Kostopoulos et al., 2018). In this thesis, a virtual, reconstructed model of the deformed DFN3-150 cranium will be provided and presented, with a potential to further enable a complete paleoneurological study of the specimen (Beaudet et al., 2016; Falk, 1978; Gonzales et al., 2015; Radinsky, 1974) that may trigger a series of paleontological questions regarding the species ancestry, short presence in the fossil record and its phylogenetic relationships. This study will be followed by the further improvement of the virtual model, using computational and statistical tools as well (Amano et al., 2015; Benazzi et al., 2011; Cirilli et al., 2020; Gunz et al., 2009b; Senck et al., 2015). Through this thesis, the main aspects of the workflow will be pinpointed, with concern to some theoretical manifestations of that kind of virtual research.

The fossiliferous site of Dafnero, named after the eponymous village in the prefecture of Kozani, Western Macedonia Region, Greece, was discovered in 1990 (DFN-1) (Koufos et al., 1991) and is positioned in a deep ravine system, in the eastern banks of Aliakmon river. It consists of fluvio-terrestrial clastic deposits (clays, sands, conglomerates and gravels), while the fossiliferous layer is a 2 m thick and 10 to 12 m long argillaceous lens. DFN locality, nowadays, includes three excavation sites (DFN-1, DFN-2, DFN-3) (Kostopoulos et al., 2018; Koufos et al., 1991), all belonging in the base of a 60 m thick lithostratigraphic formation that overlies uncomformably on the mollasic deposits of the Tsotylion Formation of the Mesohellenic Trench (Grevena Basin) (Benammi et al., 2020; Fountoulis et al., 2001).

The initial excavation site, DFN-1 (DNF-3 shares the same fossiliferous layer of silty sands with DFN-1) bared a fauna including characteristic taxa, such as *Nyctereutes megamastoides*, *Chasmaporthetes lunensis*, *Vulpes alopecoides*, *Mitilanotherium inexpectatum* and *Equus stenosis* ("*vireti*" morphotype), all indicating a middle to late Villafranchian (Early Pleistocene) age, while this assumption was verified when DFN-1 is opposed and calibrated to known similar faunas of Saint Vallier (France), La Puebla de Valverde (Spain), Olivola (Italy), Volax, Vatera and Sesko (Greece). In general, the middle Villafranchian stage is characterized by faunal turnovers in the genus level for many taxa (Koufos et al., 1991, Koufos, 2001). According to biochronological data (combined DFN sites including so far 19 taxa, with bovids, cervids, ursids, giraffids and carnivores) a bulk age for the fauna was set at 2.5- 2.2 Ma representing the middle Villafranchian large mammal assemblage in Greece. The fossil site DFN-3 was recently correlated by a magnetostratigraphic study at 2.4-2.3 Ma (MN17a, representing a diachronous biochronological "scale" of relevant reliability across Europe, following the Elephant-*Equus* turnover) (Benammi et al., 2020; Koufos and Kostopoulos, 2016; Nomade et al., 2014).

While DFN-1 fauna was the first to be excavated and studied, DFN-2 and DFN-3, adding so far over 1000 specimens in the "Dafnero fauna" collection, are the product of the Franco- Hellenic paleontology collaboration between the Laboratory of Geology and Paleontology, Aristotle University of Thessaloniki (LGPUT), Greece and the Laboratoire Paleontologie, Evolution, Paleoecosystemes, Paleoprimatologie (PALEVOPRIM, CNRS and Université de Poitiers, France) starting the field expedition in 2010. The subject of this thesis, the Old World Monkey cranium

LGPUT DFN3-150, was unearthed in DFN-3 site in the summer of 2014, "upgrading" it now on of paleoprimatological interest (Benammi et al., 2020; Kostopoulos et al., 2018).

The importance of studying Old World Monkeys, and the innovative methods applied onto fossil primates, derives from the need to sufficiently understand their evolutionary principles, intrinsic (phylogenetic) or environmental (adaptive) aspects and factors generating change, as being subjects of great comparative value. This would further enlighten the context of some of the most important, so far eternal questions regarding human origins, which guide forward in the emergence of what is called human intelligence and Mind, terms traditionally bonded to our brains great relative size, and internal organization complexity (Beaudet and Gilissen, 2018; Chung et al., 2019; Falk, 1978, 2015; Lemert and Spocter, 2018; Tung and Barreiro, 2017). Tracing down proof and establishing theory, regarding *Homo* biological trajectories, couldn't leave behind an extensive study of our closest relatives, in terms of homology, shared environment, and evolutionary paths.

1.1 DFN3-150 among Cercopithecidae

Primates are an extremely varied group of mammals, comprising more than 400 species since a 2013 record inquiry. This number has been enriched partly by the use of novel DNA techniques in the study of phylogeny, that way immediately influencing the Phylogenetic Species Concept (Mittermeier et al., 2013; Springer et al., 2012; Zinner and Roos, 2014). The Superfamilies of Cercopithecoidea and Hominoidea consist of the two clades of the Infraorder Catarhini. Cercopithecidae is the sole Family in the Cercopithecoidae, and is further divided into two Subfamilies, Cercopithecinae and Colobinae (Fleagle, 2013). Genetic data indicate that Cercopithecidae diverged as a clade of Catarhini in Africa near the Eocene/ Oligocene boundary, 30 to 25 Ma ago, while extinct representatives of the Cercopithecidae descent from the Family Victoriapthecidae (once consider as a third Subfamily), following retrieved samples from African Miocene sites, dated at 19 to 12.5 Ma. Recent findings of a single lower third molar (*Nsungwepithecus* gen. nov.) in Tanzania, may postpone the Cercopithecidae ancestry to the late Oligocene, 25.2 Ma, in accordance with genetic studies (Frost, 2017; Koufos, 2019; Stevens et al., 2013). In the same notion, Cercopithecinae and Colobinae clades diverged around middle Miocene, 13.2- 16.2 Ma (Koufos, 2019), differentiation that is strongly related to dietary adaptions (Jablonski and Frost, 2010).

Cercopithecinae Subfamily is divided into two tribes, Cercopithecini and Papioni, the latter of which, was further diversified in the late Miocene (approximately between 8 and 11 Ma) in the Subtribes Macacina (*Macaca* lineage) and Papionina (baboons/ *Papio* lineage) (Harris, 2000; Raaum et al., 2005; Takai et al., 2008). The wide intra macaque speciation started between 4.5 Ma and 5.5 Ma, with fossils indicating a northeast African ancestor for *Macaca* at 7-8 Ma (Raaum et al., 2005; Springer et al., 2012; Tosi et al., 2003). Divergent degrees in body size and other morphological heterogeneities in those subtribes, may be due to the exclusion of an ancestral Papionina population (with cranial proportions close to *Parapapio*), in the sub-Saharan territory, following the ecological turbulence of the Messinian Salinity Crisis (MSC) in the latest Miocene/ earliest Pliocene (Szalay and Delson, 1979). This hypothesis is to be further interpretated, as opposes to the Maschenko (1994) and Kostopoulos et al. (2018) studies, which various criteria interpret the Eurasian DFN3-150 as a possible, primitive, European Papionina. Cercopithecoids' wide post Miocene presence in the fossil record, in addition to the "great apes" (Primates: Hominidae) is a result of their opportunistic nature, in terms of dietary preferences and of habitual residence, as they retain both terrestrial and arboreal aspects of locomotion (Frost et al., 2011 and references therein).

Cercopithecids (Primates: Cercopithecidae), appear in the Eurasian fossil record in the Late Miocene. The two Subfamilies coexisted during the Pliocene until the earliest Pleistocene, while in Europe, a mixed occurrence of those clades (cf. *Macaca* sp. and *Mesopithecus pentelicus*) is recognized in an uppermost Miocene locality of Moncucco Torinese (MN13, 5.4-5.33 Ma), Italy (Alba et al., 2014). The oldest -out of Africa- Cercopithecinae specimen, attributed to Cercopithecini sp. indet. (due to the lack of sufficient comparative material), comes from the late Miocene of Abu Dhabi, 6.5-8 Ma, adding the potential of an Arabic- South Asian route of migration for early members of Cercopithicinae, before the passing through Gibraltar was possible (Gilbert et al., 2014). Gibraltar pathway is the predominant way that other Eurasian Late Miocene macaques (cf. *Macaca* sp.), from Italy and Spain followed (Alba et al., 2014; Köhler et al., 2000), although this "Gibraltar exchange" has been placed in the earliest Pliocene (Szalay and Delson, 1979). It is almost clear that MSC time interval played an important role in the North African - Eurasia cercopithecine exchange (Alba et al., 2018; Köhler et al., 2000). Soon after macaques reached Eurasia, their dispersal was rapid, and they appear already in the Early Pliocene of China (Alba et al., 2014), while a Central Asian dispersal route across Eurasia in the begining of the Pliocene cannot be excluded (Takai et al., 2008).

While *Macaca* lineage descends from North Africa in the Late Miocene at about 8 Ma (Raaum et al., 2005) and later entered Eurasia, extant Papionina inhabit the central region of the African continent (expanding the borders in Southern Arabia) with fossil representatives mainly found in the sub-Saharan Plio-Pleistocene of Africa as well (Gilbert et al., 2018).

Descended from South Africa, there are currently three taxa considered to gave rise to the modern *Papio* ssp; *?Papio izodi*, *P. robinsoni*, *P. hamaydras angusticeps* (taxon with similar proportions to extant representatives), the first one representing a potentially more primitive Papionina form, that could be assigned in a different genus. The origins of *Papio* are then placed in the Pliocene of South Africa, around 2.5-2 Ma, from where a population migrated to the East and North (Gilbert et al., 2018; Szalay and Delson, 1979). While *Parapapio lothagamensis* (with no extant representatives) is the oldest occurrence of the lineage to date in Africa, latest Miocene, 7.4-6,1 Ma (Gilbert et al., 2014), *Papio* sensu stricto appeared much later in the Papionina clade.

Theropithecus, first appearing at 4.2 Ma, is another quadrapedal member of the Papionina (Jablonski and Frost, 2010) closely related to *Papio*. It is well documented in the Plio-Pleiostocene African fossil record (the modern representative is the *Theropithecus gelada*), but findings are also reported from India (Jablonski et al, 2002), Southern Europe (Elton, 2014; Kostopoulos et al., 2018) and Israel (Belmaker, 2010). It shares some morphological features with both Macacina and Papionina, so that it is placed in its own subtribe (Szalay and delson, 1979). Nevertheless, genetic evidence may exclude it as a sister taxon of *Papio* (Harris, 2000), or at least it is not closer than *Lophocebus*, when compared morphologically (Gilbert et al., 2018).

The great variety of econitches inhabited by modern representatives of both Macacina and Papionina (from grasslands to tropical forests and snowy mountains), as well as their social and reproductive strategies, encountering in many cases intergeneric hybridization (Eronen and Rook, 2004; Gilbert et al., 2018), leaves no doubt that a complete and definite clarification of the Cercopithicoid phylogeny is yet to be achieved. Adding to the complexity of this study, the taxonomic position of the large-bodied, terrestrial adapted, fossil Eurasian representatives of the Cercopithicine clade, *Paradolichopithecus* and *Procynocephalus*, are still an open front in paleontological research, while a synonymy or a taxonomical proximity between those two genera is accepted by some authors (Kostopoulos et al., 2018; Nishimura et al., 2007, 2014; Takai et al., 2008). Members of the Papionini Tribe, it is uncertain if an absolute relationship to Macacina or Papionina is at large to be proved, since many of the traits featured across the samples, resemble as much to a *Macaca* species as to a *Papio* one (Kostopoulos et al., 2018; Maschenko, 2005; O 'Shea et al., 2016).

Paradolichopithecus is the largest cercopithicine in the Eurasian fossil record, covering a timespan from middle Pliocene to Early Pleistocene. The European forms are assigned to the species *Paradolichopithecus arvernensis* Depéret 1929, and *Paradolichopithecus geticus* Necrasov, Samson and Radulesko 1961. *Paradolichopithecus sushkini* Trofimov 1977 is known from Central Asia, and *Paradolichopithecus gansuensis*, Qui, Deng and Wang, 2004 from China, all together covering much of the entire latitudinal sub-Alpine belt, from Spain to China (Kostopoulos et al., 2018; Takai et al., 2008).

In the easternmost and Southern Eurasia, large papionins are assigned to the genus *Procynocephalus*, for which two species are recognized, *Procynocephalus wimani*, Schlosser, 1924, and *Procynocephalus subhymalayanus*, von Meyer, 1928, from China and India/ Pakistan respectively (Kostopoulos et al., 2018; Nishimura et al., 2014). An interesting note on *Pro. subhymalayanus*, is that the initial report of the findings, is probably the first publication of a fossil primate (Szalay and Delson, 1979). While there is a major possibility that *Paradolichopithecus* and *Procynocephalus* represent the same taxon, some researchers argue that differences in dental morphology favor their distinction (Nishimura et al., 2014).

The holotype of *Paradolichopithecus arvernensis* is an almost complete cranium and mandible of a female individual, found in the Lower Pleistocene site of Senéze, France (Depéret, 1929; Szalay and Delson, 1979). *Paradolichopithecus* is often described as a "baboon-like" macaque, featuring macaque-like characters cranially and baboon-like characters postcranially, with a straight indication for terrestrial adaption (Fleagle, 2013; Takai et al., 2008; Szalay and Delson, 1979). Rounded and low molar cusps, broad palate, a small maxillary sinus, the absence of maxillary fossae, as well as the presence of a thick maxillary body are macaque like characters, also occurring in *Procynocephalus* specimens, placing the genus closer to *Macaca* lineage than Papionina. Adding to the complexity, a maxillary sinus is also found in *Papio* and *Theropithecus* specimens, and the absence of maxillary fossae is identified in primitive Papionina as well (Kostopoulos et al., 2018; Nishimura et al., 2014).

Despite the fact that, typical baboon-like cranial features, like the complete engulfment of the lacrimal fossa in Oss lacrimale, are expected to be less stereotypical in *Paradolichopithecus* specimens, probably due to the primitive nature of this taxon, *Paradolichopithecus sushkini*, revealed a close relation to baboons, based in the presence of deep mandibullar and pronounced maxillary fossae, and a lacrimal fossa located completely in the lacrimal bone. This would furhter harden the development of a strong maxillary sinus, which indeed is present in the adult specimen (Nishimura et al., 2007), but in the same time, absent or weakly expressed in other *Paradaolichopithecus* species (Kostopoulos et al., 2018; Nishimura et al., 2014). These and other features of this species, allow an almost certain and justified emergence of the *Paradolichopithecus-Papio* clade hypothesis (Maschenko, 2005; Takai et al., 2008). While much of the study on specimens is conducted using the proportions of the maxillary sinus as a taxonomic index, it's variance across extinct and extant Papionina species limits it's value (e.g., Kostopoulos et al., 2018).

A potential enrollment of a *Papio* clade in Eurasia, contradicts with the state-of-art hypothesis that Papionina are an African endemic taxon, triggering questions regarding their dispersal routes, and a further study will provide an opportunity for an increased resolution of the paleoecological reconstruction of the continent in the Late Pliocene - Early Pleistocene. While climatic and habitat alterations at that time, strongly resulting in faunal turnovers, may justify the appearance of those large-bodied, but taxonomically problematic papionins across Eurasia, the abruptly disappearance of those taxa from the fossil record after 1.6 Ma, is more intriguing as it coincides with the appearance of *Homo* populations (Eronen and Rook, 2004; Kostopoulos et al., 2018).

Apart from Dafnero site, *Paradolichopithecus* is reported in Greece also from the Lower Pleiostocene site of Vatera, Lesvos Island (de Vos et al., 2002) and the Lower Pleistocene Karnazeika site in Peloponnese (Southern Greece) (Sianis et al., 2021). Among the Vatera samples, specimen AMPG PO 114F refers to a subadult or juvenile male mandible (de Vos et al., 2002; Geer and Dermitzakis, 2008), and alongside to DFN3-150, justifies Szalay and Delson’s (1979) note, that the taxon is mainly represented by underage individuals, as observed only for *Macaca majori*. Nonetheless, this similarity is possibly controlled by taphonomical factors (Szalay and Delson, 1979), but could be important for the study of population dynamics, growth rates and reproductive strategies (Erickson, 2005). As said before, a rather plural and properly preserved record of the species should be considered indicative of an enlarged basis of further research. This plurality of course is the aim of this “specimen-specific” research contribution.

CHAPTER 2. METHODOLOGY

2.1 Introduction

Declaring that the only true question is if it's worth living, even if living means suffering the same routine in a clearly set and understandable frame of action, Albert Camus speaks of the clarity of conceptual procedures needed when looking over one 's self. In addition to philosophical argumentation, an actualistic approach of clarity in paleontology, was permitted when Wilhem Röntgen introduced "radio-vision", now on, giving an insight of structures, hidden or inaccessible, letting questioners to securely measure, or seek "reality", and classify forms and change, in a completely new level.

Radiological techniques introduced a new chapter in the study of biology and computer technology expanded the boundaries even further. Moreover, and since using words to describe reality, relies on the principal that language, as being spoken by living individuals, is subjected to evolution as well, Weber (2015), among others, proposed the term "virtual morphology" to describe the new approach of studying differences among and within taxa and other materials.

The use of Computed Tomography (CT) scans and the supplementary measuring toolkits that follow the scanning procedure, are of use for both evaluation of interspecific phylogenetic relationship, accounting further anatomical features rather than the brain alone (Macrini et al., 2007), and intraspecies studies of the brain and cranium evolution (which involves sensitive samples and unreachable structures) in the course of preexisting, well established phylogenetic contexts (Balzeau et al., 2013; Orliac et al., 2012)

The concept, on which the use of radiology allows further applications, is that in tomographic sections (tomorgaphs), different absorption of a material appears with a different grey value, in a sense to understand "intra-material" absorption differences. This can be used to reconstruct the object virtually, by superimposing the sections taken from the CT device. Further on, and besides "one-specimen-description" gross anatomy studies, handling the virtual object in a comparative way, is in fact the application of certain computational and geometrical rules, as for example geometric morphometrics (GM), or morphometrics, when using the traditional measuring protocols (Gunz, 2015; Harvati et al., 2019). The GM approach is bonded to the concept of homology. Each anatomical point (of biological significance) can be manipulated as a geometric point (of statistical significance). Those points, are referred to as landmarks (Bookstein, 1991; Gunz, 2015; Rohlf, 1993).

While the study of virtually reconstructed models of fossils, and especially crania, seems to solve many problems, regarding the fragmentary nature of the specimens, it remains true that those reconstructed models serve as proxies. Multiple reconstructions of different scholars are needed in order to maintain the reliability of the reconstruction itself, in terms of criteria used to minimize error, so as the final model is a research-ready, robust volume (Bosman et al., 2019; Harvati et al., 2019; Zollikofer et al., 2005).

Following those of mechanical nature limitations and compromises, the loss of information passed by from the original to the reconstructed form (e.g. partial volume and staircase effect, due to scanning protocol, subjective, view-related observer interpretation), added by the fact that scanning, digitalization and statistical techniques are evolving in an exponential rate, the outcome seems to emerge as whole new basis of research, the "digital specimen", and so, the "digital collection".

2.2 X-rays. History, principles, detectors

Since this thesis is concerned with the study of a volume model produced via the application of X-rays technology in a biological sample, and thus, with the description of the scientific approach and handling that follows the “scanning” procedure, it has been considered that a brief report and mention of the history, instruments and principles used to produce the digital data later to be used in the computational and paleontological assessment, is reasonable.

The discovery of X-rays is related to the ancient worry of what the world is comprised from. This is thousands-years line of thinking and experimenting with the vast term of what is called “the Atom”. Centuries of theories, covering a time span from Leucippus and his student Democritus’ first complete Atomic Model (Antoniades et al., 2009), to the late studies of prodigy Sir Isaac Newton, concluded, as all intellectual phenomena do, in John Daltons’ ground shaking chemical philosophy, widely known as Atomic Theory. One of the assumption that Dalton made, was that the atom is an indivisible particle, the rather tiny “complete” constructing unit of matter, which cannot be destroyed, and lies on a proportional nature, weight and properties in respect to other elements in a compound (Grossman, 2021; Kuhn, 1951; Rocke, 2005). Still, this is the 19th century, and future was about to prove those innovators partially wrong.

Experiments that time were conducted with gases and electrical discharge (gaseous discharge), in an instrument called “Crookes tube”, or cathode rays tube. JJ Thomsons’ experiments with the cathodic ray tube, led to the discovery of electrons -early named corpuscles. “*What are these particles? are they atoms, or molecules, or matter in a still finer state of subdivision?”* he would question (Thomson, 1897:302). Electrons are subatomic particles, constituting just a fraction of the atom (Falconer, 1997). The experiment that provided quantitative proof of the existence of electrons is named “mass to charge” (*m/e*) experiment (Falconer, 1997; Thomson, 1897). Still, X-rays, or Röntgen rays, were discovered two years earlier (Röntgen, 1895; Thomson, 1896). They were named X-rays *“for the sake of brevity”* Röntgen (1895:227).

Probably the most profound observation Röntgen himself did, is that X-rays are produced by the matter and that are absorbed at different levels for different materials. In the third paragraph of the publication, *On a new kind of rays*, Röntgen (1895) formulates the manifest of the medical (Scatliff and Morris, 2014; Thomson, 1896) and thereby paleontological (El Albani et al., 2019; Harvati et al., 2019; Kostopoulos et al., 2018; Liakopoulou et al., 2021) usage of X-rays; that the density of the objects put in between the current of those rays, is responsible for permeability variation (Röntgen, 1895).

X-rays are an ionizing radiation, a type of “light”, capturing a very specific wavelength, a stable niche of 0.01 to 10 nm. As rays, when they fall on matter, three possibilities exist, transmission, absorption and scattering (Ou et al., 2021).

2.2.1 X-ray generation

The X-ray generator, X-ray tube, functions in a more or less same manner to the original Crookes tube. A cathode material, when heated appropriately at very high temperatures, is capable of “producing” free electrons, those forsaken *cathode rays*. This electron production (e^-) is described as thermionic emission, and is driven by the increase of electrical power, and thus energy, exceeding the bonding forces, inside the atom (Berger et al., 2018; Iniewski, 2009).

This electron stream, which could be pictured as a current, travels through vacuum conditions to an anode material, the positive target, and there is where the X-rays are generated. The high kinetic energy electrons from the cathode collide with the particles of the anode material, and part of them, through energy state changes, produce photons in the X-ray spectrum (Berger et al., 2018; Haidekker, 2013; Ou et al., 2021; Windsor and Michaels, 2008).

In simple words, the X-ray beam, is a high energy electromagnetic radiation - high energy photons - that exist in time and space, with their period and wavelength, and can be described equally as photons and waves. The unit describing the energy of a photon is the *electron volt* (eV), which is the energy that an electron gains when accelerated in a field of differential potential of one Volt (Knoll, 1989).

When a photon hits an atom, the process of ionization takes place. This means that this photon is capable of ejecting an electron that is bonded to an atom nuclei when reaching it (Seibert, 2004). Two distinct generic kinds of radiation are derived when free electrons hit a target. The first, *characteristic* or *direct X-ray radiation*, is accomplished when a free electron hits and releases an inner shell electron from the anode material atom, thus leaving the target atom with an electron "lack" (Berger et al., 2018; Knoll, 1989; Omar et al., 2020). Due to the material dependant nature of this type of radiation, it is possible to determine an unknown element by its energy spectrum, which acts as a signature. The same principle is used in medical concepts for legal purposes, such as unidentified skeletal remains in a forensics field of application (Knoll, 1989; Perrone et al., 2014).

The other discrete process is referred to the interaction of a free electron with the anode material atom nucleus. It is called *Bremsstrahlung*, and literally means "slowed down". The passing electron looses kinetic energy and deviates to different directions. This exact energy loss reveals X-ray photons. It is known as *ionization following a photon-atom interaction* (ph) (Berger et al., 2018; Omar et al., 2020).

Only a fifth of the energy spectrum represents characteristic X-rays (Ou et al., 2021), and appears as an add on; discrete peaks of the spectrum in an intesity/ photon energy scatter plot, while Bremsstrahlung, as a continum, from minumim to maximum energy, with a clear predominance of the low energy photons. Those low energy photons can further be filtered by absorbers and eliminated (Berger et al., 2018; Knoll, 1989; Windsor and Michaels, 2008).

2.2.2 X-ray interactions

X-ray photons interact with matter in four discrete ways, coupled in two categories. *Absorption*, related to the photoelectric effect, and *scattering* (or deflection), which refers to the Compton scattering effect, and the pair production effect. There is a third scattering type, which describes the potential that no energy is lost between the initial and final photon after interacting with an electron from a target atom. This circumstance is known as *Rayleigh scattering* (also referred to as coherent/ elastic scattering), but is of no significance since no energy difference that can be interpreted exists (Berger et al., 2018; Haidekker, 2013; Iniewski, 2009; Seibert and Boone, 2005). So, a photons' possible behavior regresses between complete absorption by matter, and scattering.

All X-ray interaction mechanisms are possible, but using different X-ray energies sets the basis for the probabilities on what mechanism will prevail. For medical application X-ray energies, the photoelectric effect is the predominant, almost at 80% of the total interactions number, but still, higher energies of the beam increase the Crompton scattering effect equally (Iniewski, 2009), while the probability for Rayleigh scattering to happen, is around 5% for body tissue (Seibert and Boone, 2005).

What is fundamental in X-ray use for medical, and thus paleontological research, is the fact that the intensity of the beam, “suffers” an attenuation when passing through matter, in that a way that a detector is able to capture the degree of attenuation for each specific material comprising the anatomy of the body, and convert it to contrast. Putting it in simple words, the number of photons that arrive at the detector behind the target is decreased (Berger et al., 2018; Seibert and Boone, 2005).

2.2.3 X-ray detectors

Detectors are responsible for capturing, converting, and further promoting the X-ray photons that pass through an object and hit their surface. Those devises are akin to the interaction of radiation with matter. Their basis of function corresponds to the attenuation that is happening when a photon penetrates an object and losses energy (Berger et al., 2018; Ou et al., 2021).

When the X-ray beam passes through an object it remains irradiative. This means that the interaction between the beam and the detector material, even if the intensity is reduced, is still subjected to the abovementioned categories. What a detector does, is detecting the electric charge that is produced in its volume. Here, radiation dose is converted and quantified into electrical charge, but a wide range of instrumentation and interaction mechanisms are developed to achieve the desired measure (Iniewski, 2009; Knoll, 1989; Seco et al., 2014).

The major types of detection are three, and their usage is commonly related to the efficiency of capturing “dense” events, by means of time. The *pulse mode*, which is the most widespread type, the *current mode*, and the *mean square voltage mode* (Knoll, 1989; Seco et al., 2014).

There are a lot to be discussed and analyzed for the detectors’ principals, and a lot more when historically supervising the long run of technologies applied in the field of X-ray detection in general. A bulk, but still of fundamental importance categorization of detectors, is based on their usage. Therefore there are *dosimeters*, and *imaging detectors* (Knoll, 1989; Seco et al., 2014).

Imaging the X-ray pattern is a two-gear course. There was a time for *film-screen radiography*, and the nowadays prevailing, since the 1983 Fujiflim’s “revolution”, *computed*, and *digital radiography*. This condition immediately discriminates technological implementations in an *analog* and *digital* era (Ou et al., 2021; Seibert and Boone, 2005).

2.3 The CT scanner

The innovation that revolutionized the use of X-rays is the addition of the third dimension in radiographs, depth. Now on, the generation of a volume enables a complete inspection of an object in their completeness. Still, a 4D CT acquisition, where time is depicted for respiratory examinations is possible (Seco et al., 2014; Vásárhelyi et al., 2020). While the CT operative principles and engineering was continuously evolving, managing to balance high resolution, representation, scanning duration, and dose reduction, the appearance of volumetric rendering techniques (VRT), with dedicated software packages was driven by the same evolutionary trend (Grignon et al., 2012).

The concept of a computer assisted three dimensional radiograph was conceived by Sir Godfrey Newbold Hounsfield in a field trip, and put in clinical use in October 1971 in a London hospital (Nicholls, 2019). While the mathematical base for image reconstruction, via projections was set as early as 1917 by J. Radon, the absence of a practical image reconstruction algorithm slowed down an earlier development of this technique (Haidekker, 2013; Hounsfield, 1973). The later innovations of Alan Cormack on Radon's work set the basis for the development of the CT devise (Nicholls, 2019). The development of μCT followed some years after in the early eighties (Elliott and Dover, 1982), still, it is not an indicative method for clinical use, rather than for *ex vivo* studies (Tolentino et al., 2021), but is used to provide reference material (a "standard") (Van Dessel et al., 2013).

Just as in conventional 2D radiographs, their 3D counterparts constitute maps of absorption, meaning, that if the intensity of the beam at the source is known, and the intensity at the detector is calculated, then, the absorption coefficient of a solid object inside a body, can be a function of two variants, $\mu_{object}(x_{object},y_{object})$, when represented in a two dimensional space. This works as following; if we can determine for the same object, different absorption coefficients, from different acquisition angles of, for example, 1^{o} degree each, i.e. $\mu_1(x_1,y_1)$, $\mu_2(x_2,y_2)$…, $\mu_{180}(x_{180},y_{180})$, via rotating the object, or the configuration, we can generate its absolute position in a three dimensional sense.

When we transform those values and resolve them in a single 2D slice, of know elements (pixels), we get a "cross section" of the body, where the absolute position of the object is revealed. The procedure leading to the cross section image is termed *image reconstruction*, and is generated from different angle projections (Haidekker, 2013; Hounsfield, 1973). This projection is achieved in a mathematical notion.

Essentially, the Radon Transform, "the projection", is the *line integral* representation of an absorption coefficient, that is provided by a linear X-ray beam with an established initial intensity at the source, and a measure of the final intensity at the detector, for its known angle θ, and distance ρ from the zero point (x=0,y=0) of the objects' Cartesian coordinate system. Following Hounsfield's (1973) description of this technique, translating the source-detector pair, meaning changing the distance ρ between successive beams, and rotating the configuration (rotating the sample table), meaning changing angle θ, multiple "projection data" $p(\rho,\theta)$ of a $f(x,y)$ domain are collected. While this example accounts for a two-dimensional object, the Radon Transform can be extrapolated for any *n* dimensional space. In *ex vivo* μCT scanning devises, it is usual that the specimen rotates and not the source-detector pair (Clark and Badea, 2014; Vásárhelyi et al., 2020).

When the whole set absorption values (for projection values θ and ρ) are mapped in two dimensions, the image is called *sinogram*. This is a sinusoidal form, where the one axis depicts the angle θ of the projection, and the other the distance ρ of each projection. Inverting the Radon Transform is the image reconstruction, a form of mathematical "solution". Those solutions are referred to as *reconstruction algorithms*. Usually two are used, the Filtered Back Projection algorithm and the Fourier Slice Theorem. The latter states that, due to the equivalence between the one dimensional and two dimensional Fourier conversions, a transformation of the projection data through the Fourier "frequency domain" can lead via the inversion of the two dimensional Fourier Tranform to the desired picture f(x,y), starting from an initially acquired projection data set [projection data > 1D Fourier > 2D Fourier > inversion > f(x,y)].

The back projection algorithm, a derived version of which is used in the "cone beam" image reconstruction (Clark and Badea, 2014), doesn't apply the projection values in the Fourier domain, thus avoiding the Fourier reconstruction errors. On the contrary, it directly inverts the projection values. Those "Fourier" low spatial resolution errors are caused by the interpolation of data that are missing in its continuous domain, which account for the overall calculation. Another reconstruction strategy algorithm is the Algebraic Reconstruction algorithm.

It is mandatory to mention that all the above-mentioned fundamentals account for the simplified paradigm where the object is two dimensional, and the X-ray beam is a "pencil" ray. Modern CT and *μ*CT scanners use a cone beam emission, capturing the whole object, and different algorithms are used in reconstructing the absorption map discussed above (Clark and Badea, 2014; Grignon et al., 2012). The cone beam CT technique (CBCT), treats the volume as isotropic *voxels*, thus, resolution is identical along all three planes (Grignon et al., 2012).

A *μ*CT configuration accounts for a pixel resolution of less than 100μm, with other scholars promoting different size ranges for micro classification (Vásárhelyi et al., 2020). In regard of this high resolution potential, the "special weight" of the pixel dimensions itself, doesn't account as a lower limit for spatial information (contrast) resolution, since the very CT devise has less resolving power. This sets a limit for the resolving potential of an image which depends on the geometry of the accessories involved in the CT devise, the magnification, DELs' size of the detector and the focal spot size, for the latter of which, even the specimen itself attributes somehow as an image quality factor (Holdsworth and Thornton, 2002; Vásárhelyi et al., 2020).

The least size that a pixel can in practice attribute to enhancing a better resolution is when it gets the focal spot size. Beyond that value, any reduction of pixel dimensions won't do any difference (Vásárhelyi et al., 2020). The initial evolution of *μ*CT devises was driven for the study of bone microarchitecture, due to the high contrast signal of bone and surrounding tissues (Holdsworth and Thornton, 2002 and references therein).

In *μ*CT systems the focal spot size, which is the size that covers the electron beam in the anode material, plays an important role in image quality, with small focal spot size leading to sharper images (Clark and Badea, 2014). The Hamamatsu micro focus X-ray source (75 W, 150 kV) focal spot dimensions, used in the DFN3-150 scanning, regresses between 7 to 50 μm.

While reconstructions account for computational procedures, there is no such thing as a perfect reconstruction. Many undesired effects, concerning the CT apparatus configurations can lead to a final image with artifacts, i.e. image quality distortion (Haidekker, 2013; Maier et al., 2018).

Due to the sensitive nature of the measured entities that are calculated, in respect to various parameters of the scanning, even to the age of the apparatus, a calibration of the representative absorption values, for each pixel, namely μ(x,y) is achieved with the use of the Hounsfield Units (HU). This "scale" represents the absorption of water as the zero-point, 0 HU, and the absorption of the air, with μ=0, as -1000 HU. Each absorption value that accounts for a pixel of an image, can be transformed in HU, according to the equation $HU(x,y)=1000*\{[\mu(x,y)-\mu_{water}]/\mu_{water}\}$. The HU range of fresh bone is between 80 to 3000 HU (Haidekker, 2013).

The essential assumption that has to be discussed is that the volume is comprised from isotropic volume elements, *voxels*. Those elements are assigned by a certain value, which then correspond to the absorption coefficient of any point in the volume, and further, this voxel is reconstructed by the alignment of the two dimensional picture elements, *pixels*, in the cross section that includes it (Holdsworth and Thornton, 2002). For this technique, it is essential to acquire more intensity equations of the object, than there are 2D variables in the cross section (pixels, n*m dimensions) (Haidekker, 2013).

2.4 Virtual post acquisition process

Along the acquisition, which produces cross sections of a volume, there are gaps in between each of the individual slices. This information loss is balanced through interpolating the values bracketing the hypothetical missing point [e.g. (Barequet and Vaxman, 2008; Leng et al., 2013)], but still, without creating new information. On the contrary, these techniques represent already existing values of other points inside a slice, in a weighted sense, but the variation of data among the scalar filed may lead to effects of inaccuracy, as opposed to the real object (Luccichenti et al., 2005; Preim and Botha, 2014; Stytz and Parrott, 1993).

The same value interpolation accounts in voxel projections onto display pixels, but also inside a voxel for some rendering algorithms (Stytz and Parrott, 1993). The values of voxels in CT are representative of the density (attenuation) of structures, and are depicted in HU in a grey or colored scale, but also can be different via the applying a color "map" (Luccichenti et al., 2005). From a personal point of view, the use of an alternative color map in respect to the grey scale, during the processing of the studied specimen, permits "by demand" cross checking of ambiguous loci, of otherwise similar density. From a computational perspective, color maps are an alternative (or extension) of contouring values, which for three dimension are the *iso*surfaces (Schroeder and Martin, 2005).

In virtual operations, where the display is the actual interference and interactive devise, the question of how to project three dimensional data onto two dimensional space emerges. Thus, the fundamental task of a *rendering* technique is to determine an efficient way of dimension reduction, from voxels to pixels. This "conversion" is successful when we manage to maintain the properties of a volume, and on the same time, represent a constant scene of it, preferably by choice. There are multiple options to render, but the whole procedure has to take place in a normal rate of function in the display (frames), while minimizing information loss.

The main difference between volume rendering and ordinary surface graphics, is that when rendered, a volume is projected keeping its insight properties. Another useful aspect is that the user is able to assign specific properties to a material of choice.

There are two discrete ways to render volume data. The *direct* way, which renders a voxel-based topology immediately into discrete pixels, and then, the *indirect* approach, in which a volume is converted into a geometric surface matrix via *isosurfacing*, therefore comprising an additional intermediate phase. An *iso*surface is a locus for which a discrete function takes a constant value [$F(x,y,z,)=f$]. A popular expression of this concept is in contour maps, where loci of the same altitude are represented by an *iso*contour. Multiple stacked *iso*contours create the illusion of altitude in a three dimensional sense, on a two dimensional physical object, the topological map (Schroeder and Martin, 2005).

As it may have already been conscious, in order for those *iso*surfaces to be calculated, the application of a grid over the volume is mandatory. The simplest kind of grid is the rectilinear Cartesian, even if spaces follow an anisotropic pattern, a regular CT case (with a dense z dimension in respect x and y-still, not in CBCT appications), while curvilinear or unstructed grids "cost" more to visualize (Babalola, 2019; Huang et al., 2000; Meißner et al., 2000).

Each of those rendering strategies is carried out by specialized algorithms. The one that is popular in the indirect approach is the "marching *cubes* algorithm" (MC), a dedicated surface rendering procedure. The reason that it granted popularity is that it is cost efficient in terms of hardware (Smit et al., 1999), and yet, balances frame rate, quality of the image and computation time (Bosma, 2000).

In this module, if a constant, default value of the field appears within a voxel, the algorithm creates triangles that connect these value-points. This value is called the *iso*value. The surface that satisfies those values is the pre mentioned *iso*surface, which in turn, in a larger scale, is a set of polygons. The whole procedure is termed *triangularization*, and its outcome is a continuous geometrical field. The two dimensional analog of this application is called "marching *squares* algorithm" (Preim and Botha, 2014; Schroeder and Martin, 2005; Bosma, 2000).

While the direct methods can apply opacity values to voxels, thus allowing a detailed approximation of the material properties, such as the degree of illumination or transparency, this doesn't apply to the marching cubes algorithm. Here, the "modeling" of the initial volume concludes in a solid representation (Kumar and Vijai, 2012). This should not be the issue in virtual paleontological specimens, rather than a theoretical limitation of the rendering strategy that is used.

The marching cubes algorithm was introduced in the late eighties (Lorensen and Cline, 1987). Here, each cell of the volume contains eight voxels that form the vertices of the cell cube. In terms of CT slices, it can be said that four voxels of the cube lay on one slice (x), and the rest four on the other (x-1). The algorithm processes each cell independently, and permits an *iso*surface to intersect the edges of the cubic cell, assigning each vertex as positive (or inside the surface/ contour) when its value is greater or equal to the *iso*value, and negative (or outside the surface/ contour) when its value is less, in a single cell space (Custodio et al., 2019; Preim and Botha, 2014; Schroeder and Martin, 2005). What makes the marching cubes efficient and preferable, is that the possible intersection within a cell (named *case table*), thus, the possible triangulation, is an individual case of a limited number of scenarios (with additions through the years), that way fastening up computation time and minimizing cost (Custodio et al., 2019; Preim and Botha, 2014).

The case table is the reduced (due to symmetry) scheme for 256 configurations that a surface intersects the edges of the cell, since the eight vertices of this cell, can either be inside or outside the intersecting *iso*surface (it is a binary state assignment, thus, 2^8=256 possible ways) (Schroeder and Martin, 2005). So, for an *iso*value *x*, the voxels that score less than this, will be excluded and isolated by a surface within the same cubic cell, in favor of the voxel that scores above this value and vice versa (Kumar and Vijai, 2012; Meißner et al., 2000).

This technique leads in an overall of fifteen cases (scenarios), for which a cell could be ascribed to. The exact location of the intersection along an edge of the cell, is determined by a linear interpolation algorithm, and is a function of the *iso*value, and the value of the voxels of the edge. In the instance that the *iso*value appoints to the value of a vertex exactly, it has to be manipulated so as not to produce an invalid triangle. The intersection point across the edges of cell is combined with the case-table of possible triangles. This method deploys a binary state for each vertex, namely if it belongs or not in the surface (Preim and Botha, 2014). The created polygon (*iso*surface) is the topology connecting those edge-intersecting points. Still, due to the extreme amount of polygons created, the whole process can delimit the time of calculation, and other approaches have been tested to address this issue (Smit et al., 1999 and references therein).

Another disadvantage of this technique is that a surface intersects an edge just once per cycle of process, thus not allowing the reproductions of sharp-geometries, which many times are crucial for interpreting volumes. This is addressed by using a marching tetrahedra algorithm, which subdivides a cubic cell in six tetrahedra (multiplying the edges of the cube), and then applies *iso*surfaces (Bagley et al., 2016). One of the theoretical assumptions been made in this rendering philosophy, is that those polygons that create a mesh in order to describe the volume examined, are infinitely thin, thus the volume is legit (Meißner et al., 2000).

The major fall back of the marching cubes, is that is sensitive to ambiguities. The way it triangulates the surface, may leave each cell with holes, while surfaces are separated or connected. This is happening when diagonal vertices fall in the same state, but those in an edge of a face (for cubic cells), are of different (Schroeder and Martin, 2005). Various solutions on this have been proposed, by extending the case table, or by adding a manual priority function.

For further extending the productivity of this method, in order to "solve" only the valuable cells, and not the entire volume, a *MinMax tree* strategy is used. Here, only those cells that are grouped in by means of a minimum and maximum value are used. When the *iso*value is engulfed between this MinMax range, only those cells ascribed there are further processed, that way allowing an *accelerated* surface extraction (Livnat, 2005; Preim and Botha, 2014).

One popular way that applies in structured grids, is the use of hierarchical dividing (decomposing) the volume data set via *octrees* (Meagher, 1982), and then extracting the *iso*surface (Wilhelms and Van Gelder, 1992). This procedure subdivides each cell in a maximum of eight derivates, and keeps only those voxels attributing to the *iso*surface (Smith, 2020). Other approaches address this time efficiency optimization as well, able to process grids without structure, since they are not geometry-dependant, rather than value-dependant, and others, reduce the extent of the generated grid (Cignoni et al., 2005; Livnat, 2005).

Those algorithmic extensions are developed due to the time-consuming effect that cells not attributing to the desired *iso*surface impose in the overall computation, in order the algorithm to find the actual "surface" attributing cells, and calculate the point of intersection. On that behalf, an algorithms' efficiency is a matter of how many cells it has to process (Itoh and Koyamada, 2005).

All these are useful also when the user wants to change the *iso*value and immediately see the changes without delay. The ongoing evolution of rendering techniques and the exponential growth in rendering performance needs, for medical, industrial and recreational purposes, has lead the visualization field of application, to be considered a high-end valuable game changer among many professionals (Custodio et al., 2019; Grosso and Zint, 2021; Lopes and Brodlie, 2003; Smith, 2020).

Concluding, those *geometric primitives* algorithms operating on the CT data can be classified as "scalar" and of "combined transformation", since they alter both the structure, geometry and topology of the original scalar field values of the input image (cross section) to reproduce the virtual volume (Schroeder and Martin, 2005). Still, even if the analysis accuracy depends on voxels dimensions (Smith, 2020), surface rendering techniques face drawbacks in terms of accuracy, and information completeness, in an effort to manage a balance between time efficiency and usual workstations' memory capabilities, that way promoting a specific cost-dependence range value for these applications.

CHAPTER 3. MATERIALS

While CT technology has been applied in paleontology since the mid eighties (Conroy and Vannier, 1984), and the first virtual reconstructions were published more or less a decade later (e.g. Zollikofer et al., 1995), a complete restoration/ retrodeformation of the LGPUT DFN3-150 cranium was not possible to be accomplished during this master thesis. This early conclusion was mainly driven by the time consuming nature of the manual segmentation process, in respect to possible corrections that could, or should be applied, prior to the delivery of a final, solid virtual specimen, as well as by the lack of state-of-the-art numerical applications, like GM methods, in a mathematical approach of reconstruction, which otherwise could yield an insight in the deformation processes as well (Di Vincenzo et al., 2017). Nevertheless, the present provided virtual specimen constitutes a part of the final accomplishment, that way being an essential portion of the entire workflow; that of segmentation and fragment reposition.

On the other hand, besides the progress itself, multiple reconstructions should be provided, so as to assess the inter-, or even the intraobserver error potential (Harvati et al., 2019; Shearer et al., 2017; Zollikofer et al., 2005), in respect to a hypothetical, legit virtual specimen delivery, but also for the very segmentation process, for which the experience status among different scholars plays a significant role in execution accuracy (Fourie et al., 2012). This accounts especially if the initial paleoneurological aim of this project is of any concern, since the *μ*CT provides a high resolution basis already. Thus, the latter should be conceived only as of an overall "assistance". A virtual specimen in any case represents an "evaluated approximation" (i.e. Benazzi et al., 2011), but conclusions based on virtual specimens analysis are thought to be valid.

LGPUT DFN3-150 refers to an almost complete but deformed cranium, of *Paradolichopithecus* aff. *arvernensis*. It's deformation [Types 1 and 3 disturbance in the Weber (2015: 32) qualitative scale] corresponds to a slight mediolaterally compression of the right side of the cranium, 5 mm backwards, and around 10 mm medially and upwards, followed by breakage clearly shaped in the left parietal area of the cranium, but in the right as well. The specimen belongs to a subadult, female individual (Kostopoulos et al., 2018).

In the current workflow, no template scheme on which a potential retrodeformation could be based on (Cirilli et al., 2020) was used– usually this is a reference sample, of high taxonomic and "geometrical" proximity – as well as no statistical or geometrical approaches (Gunz et al., 2009b; Senck et al., 2015), or even scaled (based on regular measurments) individual bones from other samples of the same taxon (Rawson et al., 2021) at all. Thus, options that validate the current reconstruction process orient from bilateral symmetry and "smoothness" axioms of the fragment junctions, for which a continous contour between to fragments is recreated without gap in between them. In the present, the workflow is termed as *mechanical reconstruction*, i.e., a restoration, meaning that the reconstructed specimen constitutes a non numerical, non billaterary "retrodeformed" configuration (Schlager et al., 2018), rather than a relative repositioning of the segments extracted.

Still, while bilateral symmetry is considered a common mammalian feature (while exceptions are not to be neglected), and smoothness is an aspect of a regular positioning of the cranial bones, some constraints are possible to be applied, so as to "control" manipulation of the fragments (e.g. Benazzi et al., 2011; Gunz et al., 2020a, 2020b; Haile-Selassie et al., 2019; Harvati et al., 2019; Zollikofer et al., 2005, 1995)

These constraints could be the alignment of the (perhaps) rotated or translated midsagittal planes that differentially arise from both the viscero- and neurocranium portions of the sample, and thus permitting a reasonable biological basis for the width of the reconstructed skull, when the rest of the fragments will be placed accordingly. Fragments then will follow the other mentioned criterion, by minimizing the gap between the fragments, while keeping a “soft curvature” among individual ones, to the point where no gap is left. Another form of control upon the process is the application of “degrees of freedom” for the fragments’ movement. This of course should account in an instance where plastic deformation isn’t much present, and the differential position of the fragments is an outcome of breakage and matrix invasion between them. Thus, the application of a “degrees of freedom” protocol (for rotation and translation of the fragments), should fill out the “smoothness” proximal manipulation of fragment repositioning.

3.1 Initial virtual anatomic inspection

Segmentation describes the dedicated procedure in which pixels in the display, corresponding to CT cross sections’ material, are assigned and labeled in groups by choice. Then the software user is able to individually manipulate the segmented fragments (groups). The almost identical threshold value of matrix and bones, immediately pointed out that a semiautomatic segmentation procedure couldn’t be applied. Besides that, even though the diploe part of the bony material is not completely affected and rather exhibits an “expected” preservation image, in respect to the typical macroscopic view, the inner table of the bones usually suffers from a “collapse” and boundaries among individual bones are not discrete.

Parts of the inner table – especially in the posterior part of the neurocranium – can be found inside the matrix in various proportions (in respect to shape and size) that way affecting the “black line” surrounding the inner table of the bone. This density boundary is the diving level between bone and matrix, and also serves as the segmentation base, and once, besides the sediment shrinkage, was filled by the dura matter tissue. This “compressive” collapse is evident in its most severe expression in the right parieto-occipital area of LGPUT DNF3-150, both over and under the nuchal crest, but in the temporal also, especially in the petrous and tympanic parts.

After selection, twenty five segments, five for viscerocranium and twenty for neurocranium were extracted (Table 1, 2; Fig. 1-6), for which, one accounts to the separate sella turcica. Additionally, some of the fragments don’t share a bilateral counterpart; the nasal fragment and one depicting the protrubing calvarial top, the latter of which was difficult to assign to a specific side, as part of the frontal or parietal segments. The same condition applies for occipital fragments as well. Initially, thirty six segments were determined, following a maximum availability concept, but this excess that corresponded to minor structures couldn’t be manipulated, and otherwise would add more time in the overall project, while not minimizing failure or deformation signal after reconstruction.

The most controversial aspect of the segmentation, related to the overall strategy conducted by the user, was to keep a reasonable ratio of fragment generation and bilateral partitioning. This, besides the preservation status, accounts as the main error factor, in terms of crystal clear fragment extraction, since only a very small portion of the cranium is broken, and most of the segmentation is based on visible sutures among bones, which in some occasions are confronted as “suture zones”. This tactic was mainly driven by the need to mechanically eliminate plastic deformation, allowing each fragment to be independently replaced, in a relative position though.

Table 1. Ossa crania segments (#20) on the original virtual specimen.

Bone	Side	Color	Abbreviation	Bilateral	Single
Oss occipitale	transverse develpoment	Grey	Occ-1		yes
		Deep pink	Occ-2		yes
		Deep blue	Occ-3		yes
		Golden	Occ-4		yes
	right [*]	White	Occ-5		yes
	Pars basilaris	Bright golden	Occ-6		yes
Os sphenoidale	left [2]	Radioactive green	*Fused with the related temporal*	-	-
	right	Purple	Sph-1		yes
	Sella turcica [1]	Light green	Sel		yes
Os ethmoidale		-		-	-
Os frontale	left	Light red	Fro-1	yes	
	right	Deep red	Fro-2	yes	
Os parietale	left	Pale yellow	lPar-1	yes	
	left	Pale orange	lPar-2	yes	
	left	Pale purple	lPar-3	yes	
	left [*]	Deep purple	lPar-4 *(1a)*	yes	
	right	Deep purple	rPar-1	yes	
	right	Light green	rPar-2	yes	
	right	Blue	rPar-3	yes	
Oss temporale	left [2] *(+left sphenoid)*	Radioactive green	Tem-1	yes	
	right	Dark grey	Tem-2	yes	
Calvaria top [3]	-	Cherry purple	Cal		yes

[[1]separated *in silica* only; [2]referred to as "temporo-sphenoid" in text; [3]*in silica* space; part of Os frontale/ Os parietale in the original specimen; [*]*italics* depict the inner position of the segments].

Table 2. Viscerocranium segments (#5) on the original virtual specimen.

Bone	Side	Color	Abbreviation	Bilateral	Single
Maxila	left	Light green	Max-1	yes	
	right	Bright yellow	Max-2		
Os lacrimale	-	-	-	-	-
	-	-	-		
Vomer	-	-	-	-	-
Os zygomaticum	left	Blurred pink	Zyg-1	yes	
	right	Bright ciel	Zyg-2		
Os palatinum	-	-	-	-	-
	-	-	-		
Os nasale	-	Deep blue	Nas		yes

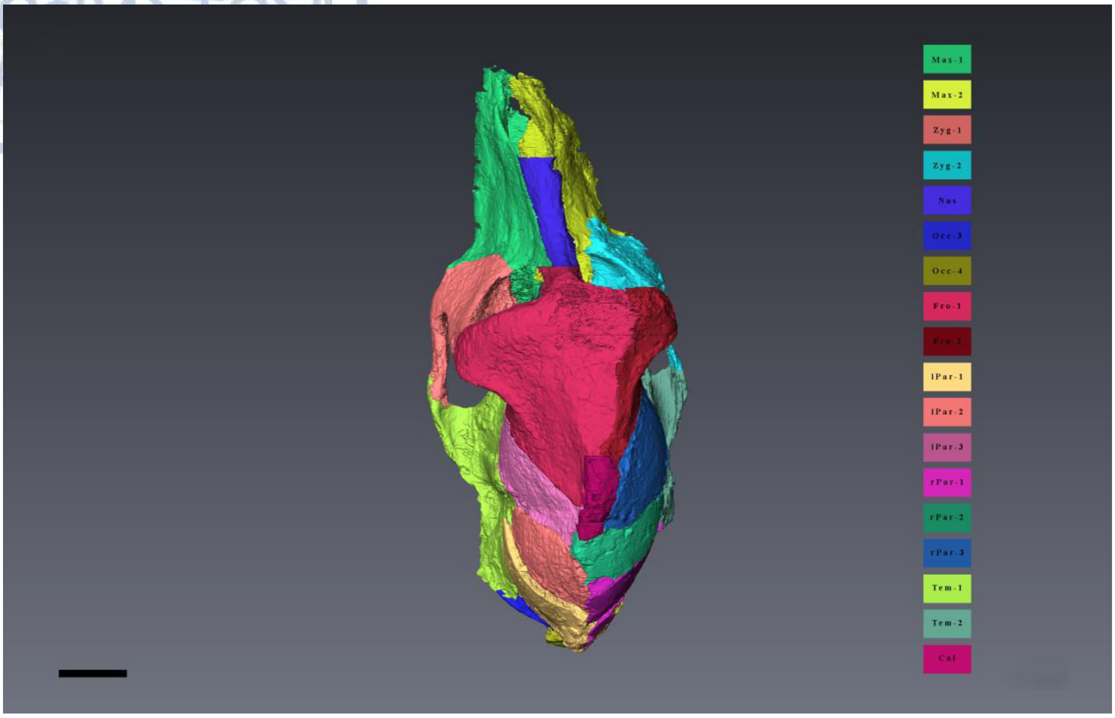

Figure 1. Abbreviation map (Table 1, 2) of segments on the original specimen. Dorsal view. Scalebar 2 cm.

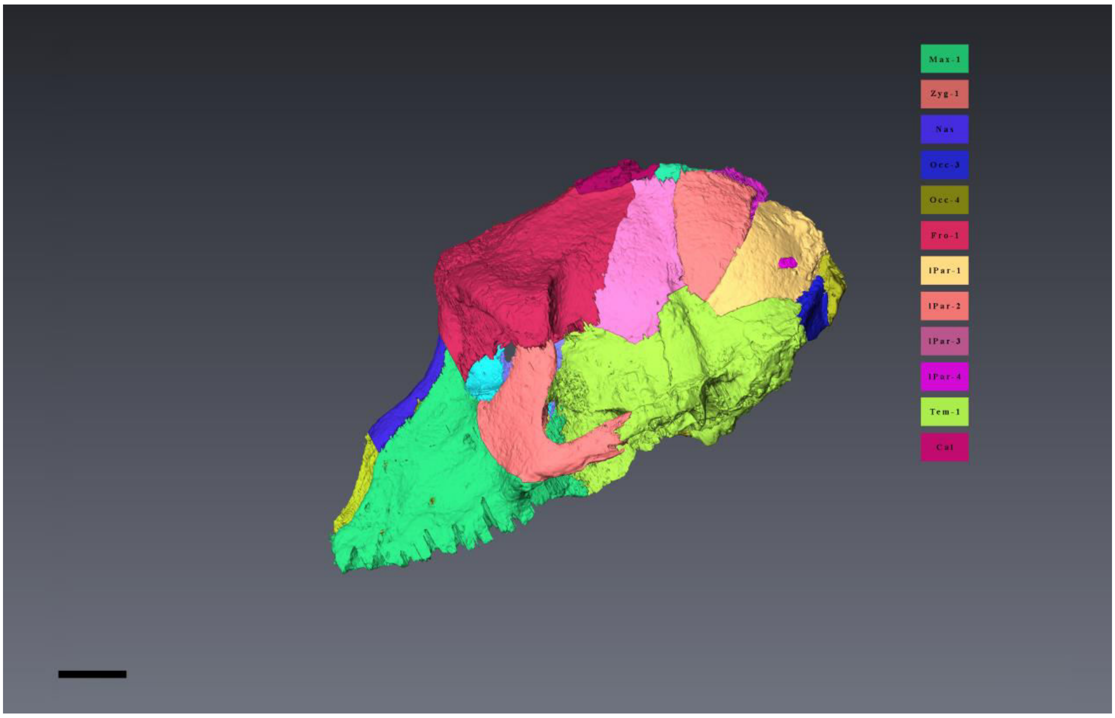

Figure 2. Abbreviation map (Table 1, 2) of segments on the original specimen. Left lateral view. Scalebar 2 cm.

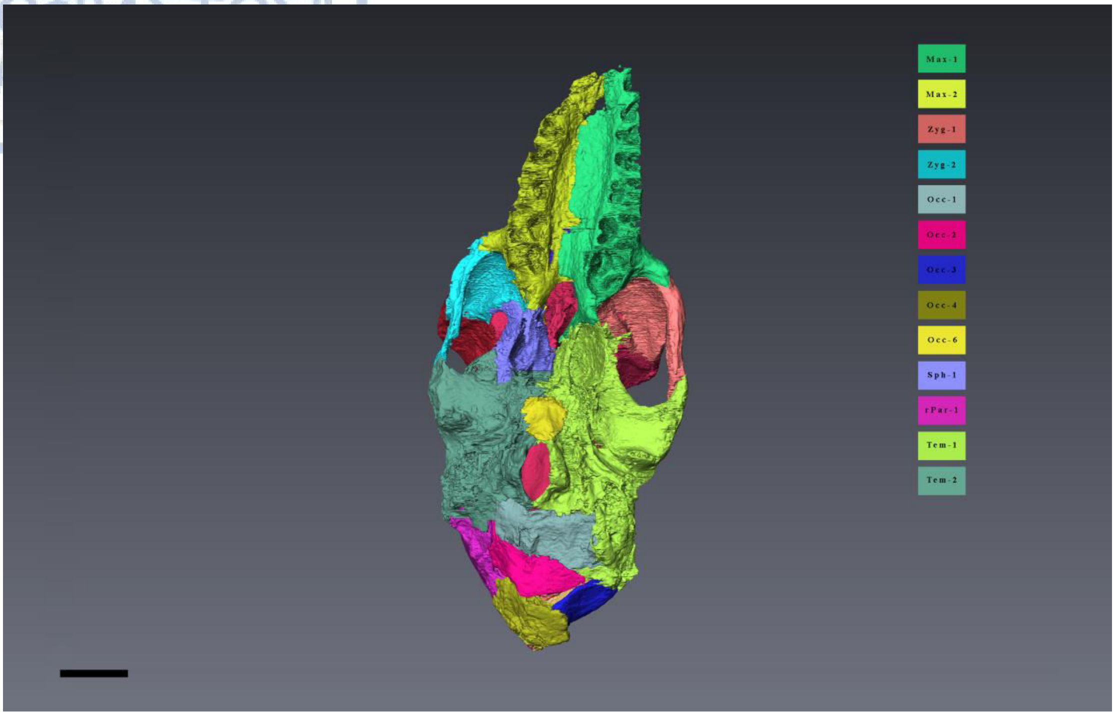

Figure 3. Abbreviation map (Table 1, 2) of segments on the original specimen. Ventral view. Scalebar 2 cm.

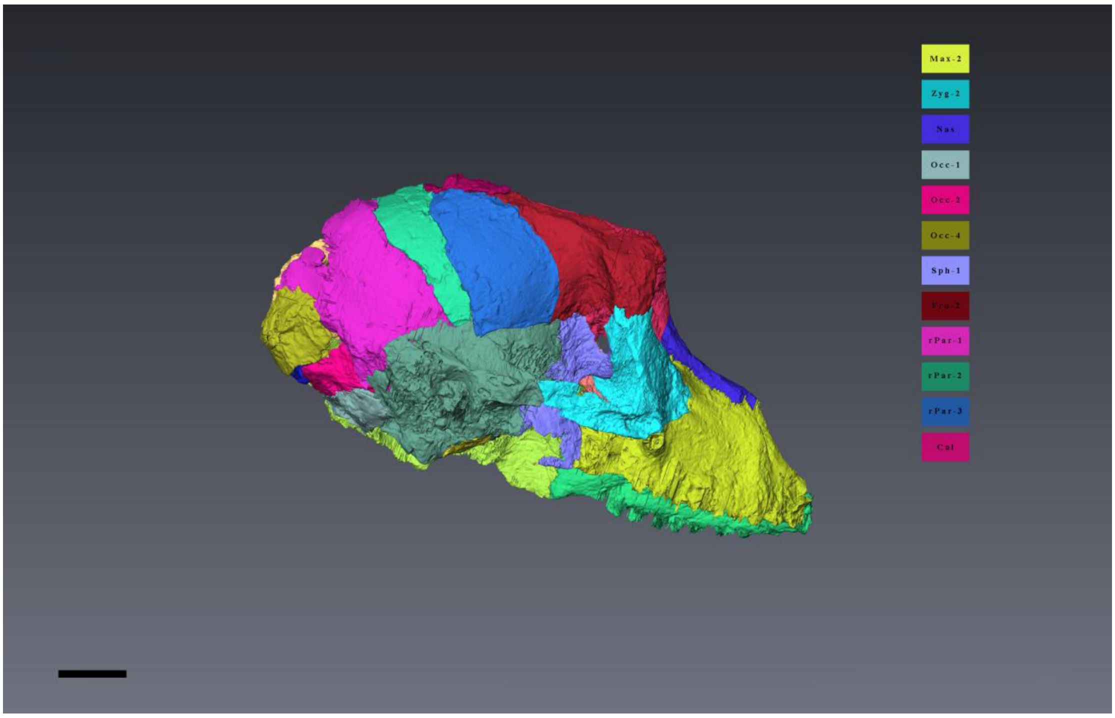

Figure 4. Abbreviation map (Table 1, 2) of segments on the original specimen. Right lateral view. Scalebar 2 cm.

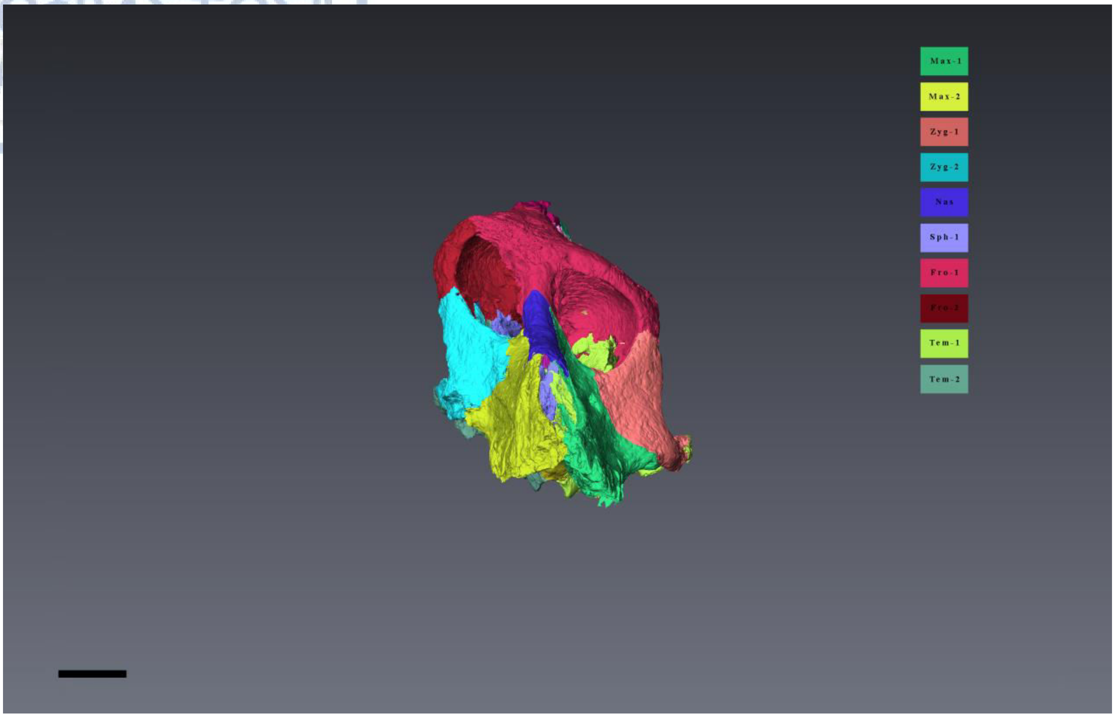

Figure 5. Abbreviation map (Table 1, 2) of segments on the original specimen. Frontal view. Scalebar 2 cm.

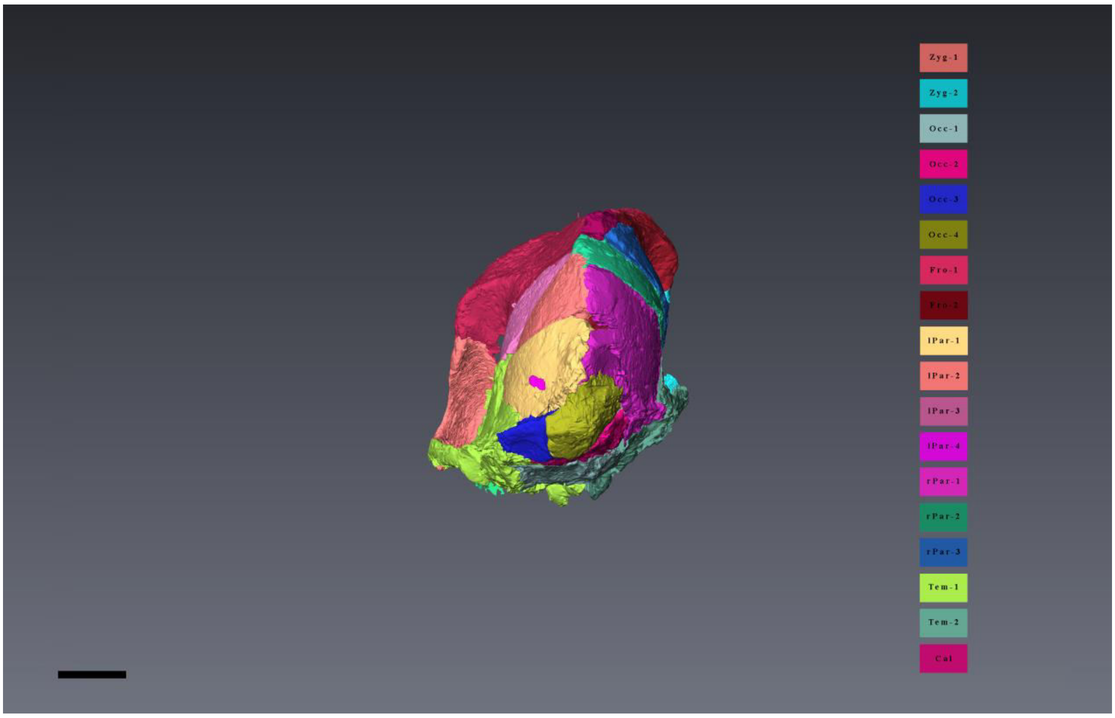

Figure 6. Abbreviation map (Table 1, 2) of segments on the original specimen. Posterior view. Scalebar 2 cm.

Neurocranium

Along the midsagittal plane, approximately from bregma to inion, a strong fusion of the parietals and occipitals on both sides of the cranium occurs. It seems that the left side ones are wedged inside the rights, that way giving the impression of a strong pseudo-crest (*SFig. 1, 2*). Anyway, this structure vanishes around the coronal suture, for which is the boundary of the mostly unfractured but strongly deformed frontal bone.

The frontal bone (Fig. 1) is segmented in two pieces. Even if the supraorbital tori aren't fragmented, there is a strong compression scheme in the right supraorbital margin around the zygomatic process, which thickened the diploe part of the frontal in that area, in relation to the well-presented left part (*SFig. 3*). Another more controversial inner structure emerges here, that seems like a "growth line" (e. g. in the epiphysis of the long bones). This, divides the rostral part of the frontal bone in three parts, two – right and left – "superciliary" areas, and a central "ophryonic" in between them (*SFig. 4).* Anyway, a metopic suture (as expected for specimens' dental group) or other fracture is absent, thus this structure is likely the outcome of compression, rather than any of anatomic, ontogenetic significance.

In an effort to reduce the compression load in the following reconstruction steps, the frontal bone is segmented in two parts (Fig. 2, 4, 5), a) the narrow right half-superciliary arch, starting from its related fronto-zygomatic suture all way caudally to the coronal suture, and laterally to the sphenofrontal suture and b) the remaining left "torus" accordingly (including half of the elevated right arch). A further division based on the abovementioned compression structure – including the ophryonic part – would exhibit a rather sharp and abstract impression, in an otherwise not fragmented bone. The fact that a third "phantom" segment would affect the other following segments, while not contributing much in the restoration of the frontal in general, is the main reason not to present it individually. Otherwise the neurocranium exhibits clear fragmentation that allowed segmentation of individual fragments.

In the right parietal area (Fig. 4), a surface extending from approximately the lamdoid suture of the vault, all along the squamous suture to the coronal one, three major fragments were extracted. From a posterior point of view, the third of them, delimited by the coronal suture rostrally and the squamus suture caudally is in perfect continuity with the right frontal segment, and the division was based by criterea of maximizing the number of individual fragments. The first, second and third right parietal segments are in "good" contact, meaning that no relative displacement occurs, but the division was based on available discontinuities to the extent that a very slight disposition would not justify a complete move of the fragments.

The left parietal area (Fig. 2) consists of three separate fragments, and one additional inner fragment (Fig. 2: **lPar-4**), which otherwise is in exact contact with the first one (Fig. 2: **lPar-1**). An interesting aspect on this side is that, even if the left bilateral side is considered as the non deformed, this accounts mainly for the viscerocranium part. Between the second and the third parietal fragments (Fig. 2: **lPar-2** and **lPar-3** respectively), a strong curve is present, with a triangular shape around bregma but caudally positioned, and becomes a straight depression line all way inferiorly to the supramastoid crest level in the left temporo-sphenoid segment, **Tem-1**. This could be read inversely (*SFig. 5*), so that a robust rectangle compressive "crest", approximately completely inside the left temporo-spenoid bone, starts exactly at the level of the mandibular fossa and continues throughout its petrous part. On the opposite sites of this crest the petrous part is flat.

Among those three major parietal fragments, the first one (Fig. 2: **lPar-1**) is the only neurocranium segment that was later repositioned, due to its discrete displacement in respect to its neighboring fragments. This genuinely "broken" fragment is in absolute contact with the left temporo-sphenoid segment, but in a coronal plane, the rostral part exceeds laterally, and the following – second left parietal (Fig. 2: **lPar-2**) – is positioned relatively ventral (*SFig. 6, 7*). Despite the fact that may have not affected the relative positions of the respected fragments, these fractures follow the projection of the great transverse "crack" that runs across the whole specimen, following an oblique inclination towards the anterior of the cranium. This discontinuity is probably responsible for the convergence between segments **lPar-2** and **lPar-3** in the left parietal a rea, disrupting the globular shape of this side in addition to its right counterpart (*SFig. 8,12*).

The right temporal fragment (Fig. 3, 4: **Tem-2**) incorporates part of the basis of the occipital, from pars basilaris to the condylar fossa, completely engulfing the occipital condyles and so on half of the foramen magnum. The same accounts for the left temporal bone (Fig. 3, 4: **Tem-1**), incorporating the other half of the occipital. Another beautiful aspect of the temporale is the well preserved articular eminences.

The occipital bone is divided in four fragments (Fig. 3, 6: **Occ-1** to **Occ-4**). The first two (Fig. 3: **Occ-1**, **Occ-2**), starting immediately posterior and in contact to the foramen magnum, are placed vertically to the londitudinal axis of the cranium, and witness the erodously preserved and slight occipital crest. The other two fragments encounter the nuchal crest (Fig. 1, 3: **Occ-3**, **Occ-4**) which is strongly present in segment **Occ-3** (Fig. 2). These fragments are positioned side by side in the same vertical notion as the previous ones, with the difference that the left one, **Occ-3**, is in contact with the left temporo-sphenoid fragment, and the right one, **Occ-4**, which is protruding posteriorly, is in contact with the first right parietal fragment (Fig 4: **Occ-4** and **rPar-1** respectively). In the latter occipital, a rather wide gap is present between this one, and the first right parietal. Still, an additional fragment was successfully segmented but is placed inside the vault, possibly a result of collapse (Table 1: **Occ-5**), or it may be part from the first right parietal as well (*SF 9*). No indication of interparietal bone was found to interpret this inner fragment otherwise. Also, the pars basilaris (Fig. 3: **Occ-6**) of the occipital was individually segmented, for which an unaffected pharyngeal tubercle is clearly shaped (like an elongated crest), but it was rather difficult to present it connected to the occipital condyles in an exocranial view.

An effort was made so as to individually segment different bones on the basis of the cranium (i.e. pyramidal process in the temporal, basioccipital), but the distractive image of the insight of the vault delimited this attempt (*SFig.10*). So, different proportions of the bones, in the form of an extreme "stair case" effect, especially where the temporal and sphenoid meet, are typical of their condition across two sides. In the dedicated right sphenoid fragment, a clear abrupt boundary is seen lateral and posterior to the pterygoid process in the contact with the temporal (Fig 3), proving the difficulty on "what" to segment.

The sphenoid bones account as the most difficult ones (Fig 2, 4: **Sph-1** and rostral part of **Tem-1**) to be segmented. Not both the bilateral sphenoid parts are assigned to as individual fragments (Table 1). The left hemi-sphenoid, **Tem-1**, is virtually "fused" with the temporal bone. The pterygoid processes though of both, display a major difference in surface size, with the lateral plates overwhelmingly exciding the medial plates, while the pterygoid fossa between the plates is deep. Both plates show a rather vertical position. Hamuli on both sides on the medial pterygoid processes are not present.

The post orbital lesser wings of the sphenoids was not able to be completely segmented, due to their fragile nature and bad preservation status, especially in the right side, so, the presented orbital foramen are rather a byproduct of the segmentation "effort" and not a distinctive anatomic appearance, to be further processed. The roof of the orbit and the medial orbital wall is comprised only by the two frontal segments, and an ethmoid fragment is not independently segmented (Fig. 5).

As for the endocranial part of the sphenoid, only the sella turcica was able to be clearly segmented as a surface (*SFig. 11*: **Sel**), even though as a separate fragment rather than the posterior part of the sphenoid body. Still, no anterior clinoid processes are evident, but the tuberculum sellae can be seen. This fragment is delimited by the dorsum sellae. In general, the right bilateral side of the neurocranium seems more globular and unaffected, especially in the parietal. This is rather the outcome of the great "crack", that displaces the fragments mainly on the left side (*SFig. 12*).

Viscerocranium

In the viscerocranium (Table 2; Fig 1-6), the most ambiguous case was the nasal segment. In the contact with the frontal, a frontonasal suture is absent, even if a transitional diploe scheme is evident is a sagittal plane (*SFig. 13*). Thus, in the virtual model, the nasal segment starts abruptly in front of the frontal bone (Fig. 1, 5: **Nas**), approximately at the dacryon level, and following a coronal plane. It was segmented from its early "flat" form before reaching the premolars, all the way to the strongly curved part of it, until reaching rhinion, over nasal aperture.

Since a premaxilla-maxilla suture is not present, but rather a slight depression before the canine alveoli could delimit the maxilla segments, both maxillary where segmented including the premaxillas (Fig. 2, 4: **Max-1**, **Max-2**). An interesting aspect of both these fragments, affecting the reconstruction, is that the alveolar processes of both are curved. As early as from the distal part the second moral, the occlusal plane tilts upwards and more medially when reaching the incisors alveoli. The medial turn is stronger in the right maxilla, and the upwards one in the left (*SFig. 14, 15*). This differential deformation pattern further hardens the bilateral alignment of the fragments.

Another important aspect of the viscerocarnium is the eminent palatal overlap (*SFig. 16*). Following a potential stronger diagenetic equally distributed compression load on the whole right side of the cranial surface, the right maxillary fragment overlaps on the left side. This imposition is evident all along the palatine process (Fig. 3) and is responsible for the narrow lookout of the cranium, while on the same time, it serves as the basis of the reconstruction, since it is rather easy to segment the two processes and assign them in their related maxilla as a whole, for both fragments. On that behalf, the median palatine suture is pseudo-reconstructed. Here, the Os palatinum is included in those segments (palatine process/ palatine), since no transverse suture is available, and is in a rather normal contact with the sphenoid.

The zygomatic bones (Fig. 2, 4, 5) initially were segmented in an absolute vertical shape in their contact with the maxilla, as seen from a horizontal plane. This was later corrected so as the zygomatic segments meet the maxillary fragments at the level of the zygomaticomaxillary suture, until the level of zygomaticotemporal suture (temporal process) for a reasonable place to be left for the zygomatic process of each maxilla.

A minor observation on the right side (Fig. 4) is that the anterior root of the zygomaxillare exhibits an almost perfect hemispherical abrasion structure. An abrasion pattern, not canonical though, is evident in the right pterygoid process of the sphenoid, for which the lateral plate has lost a major part of its surface.

3.2 Results

Following the bilateral symmetry and "best-fit" protocols, three reconstructed models are presented. As mentioned before, these models are far from solid, research-ready virtual specimens, and their nature depicts the first attempt to recreate the bulk morphology of LGPUT DFN3-150 cranium before the deformation, but without "retrodefroming" it.

The first two reconstructions follow raw anatomical criteria. The starting point for both of which was the reposition, mainly translation of the right maxillary fragment, so as to optimally "fit" alongside its left counterpart, in order to create a continuous palatine level. Though, a constant occlusal plane is not able to be achieved, since the maxillary fragments are curved uprwards and medially. Following the "palatine reconstruction", two different tactics were executed, in order to highlight the deformation effect, across both lateral sides of the cranium, since the width, and occlusal plane, where now partially corrected.

Model 1a

In this reconstruction, the first left parietal fragment, **lPar-1**, is positioned following the shape of the second, **lPar-2**. It has been counter-clockwise rotated in a lateral direction, and translated rostrally, so as to optimally "fit" the second left parietal (Fig. 7). This reposition left a new gap between the first parietal and the massive temporo-sphenoid fragment, and somehow affected the rest of the left fragments, since a new position for the temporo-sphenoid was needed. This is mostly evident is the zygomatic arch, where the displacement alters the otherwise "regular" zygomaticotemporal suture (Fig. 8). This displacement though is kept minimal, and most of the misalignment is observed in the zygomatic arch (besides on purpose repositioning the first parietal).

The rest of the fragments follow their exact position that had in their initial space, but this time, the right bilateral fragments, where shifted downwards, slightly forward and laterally to the right, following the new right maxilla position (Fig. 9a, e). This led to an obvious and wide gap along the medial axis, but still, the fused nature of the superior parts of the parietals on both sides, maintain the contact among them, even if the robust superior parts of the left parietals – especially the second and the third – is exposed (*SFig. 17*).

In order to equally distribute the deformation effect, the left third occipital fragment, **Occ-3**, was kept in contact to the left temporo-sphenoidal fragment, and the fourth occipital, **Occ-4**, which initially lays alongside the third, was repositioned in contact to the right parietal (Fig. 9f). The created gap follows the occipital area as well. Both the first and second occipital fragments, which lay transverse to the longitudinal axis of the cranium, were kept in contact in between them and to the right bilateral fragments, namely the temporal and parietal respectively, and rostrally to their third occipital counterpart.

This overall displacement, strongly affected the basicranium, for which the foramen magnum proportions are severely altered, giving it the impression of a more wide, and circular shaped countour (Fig. 9c), opposing the initial report for a rostro-caudally elongated, oval shape (Kostopoulos et al., 2018). As the left side fragments were kept intact, following their initial distribution, the right maxilla-zygomatic-frontal configuration was altered (Fig. 9e and *SFig. 18* for comparison). This repositioning is highly possible that lead to an overall higher degree of exposure for the right temporal fragment, mainly witnessed in the zygomaticotemporal suture, which otherwise is forming a constant contact. This "discontinuity" is rather a side effect of the not tightly and "smoothly" reposition of the right fragments, possibly the temporal (*SFig. 19*).

A valuable question to ask at this point, is whether the basillar part of the occipital, **Occ-6**, for which a dedicated segment was extracted (Table 1), presents its extended pharyngeal "crest" as part of its anatomic surface, or rather this is a matter of deformation (*SFig. 20*). This concept is reasonable if the gaps created among the new positions of the temporals, which lay on the lateral margins of the basilar segment, are of any significance, indicating a rather "flatter" initial basilar segment, in order to fill the gaps. The same gap allocation applies in the viscerocranium as well. Both maxillary fragments demonstrate this widening, and their contact at the intermaxillary suture level is interrupted. Here, restoring deformation while keeping an approximately constant symmetry for the unerupted third molars and the pyramidal processes of the palatines (posterior to the maxillary tuberosities), evidence the different deformation effect between the right and left maxilla.

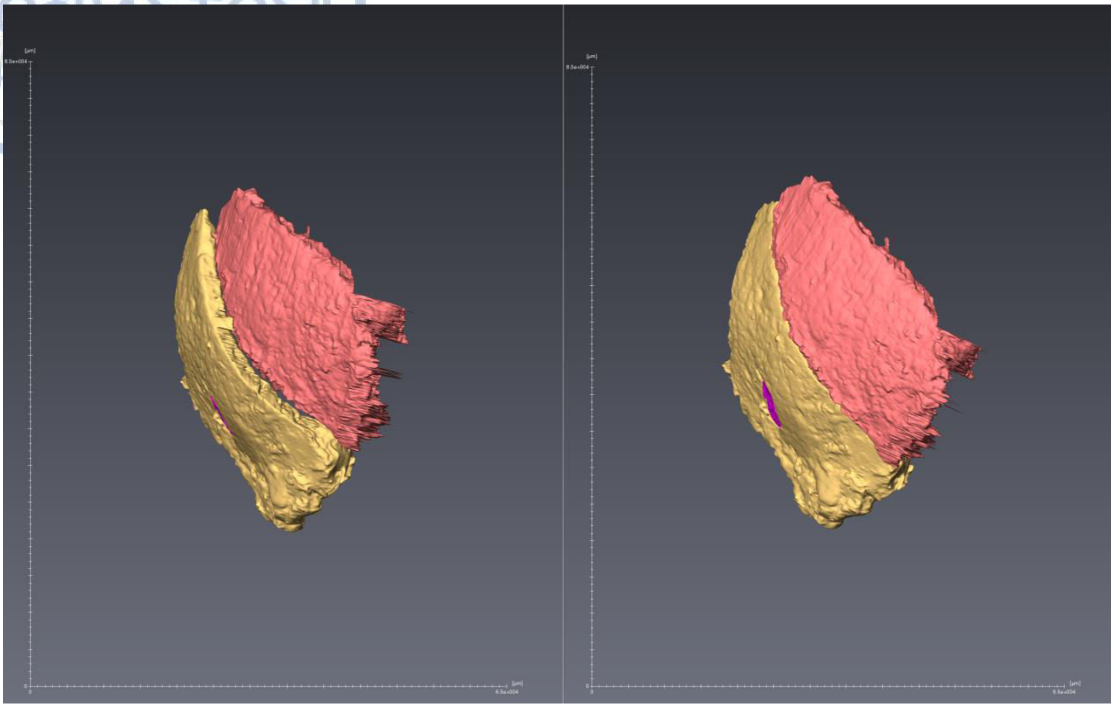

Figure 7. Reposition of the left parietal fragment lPar-1 following lPar-2 boundary in *Model 1a* (right) and initial position in the original model (left). Oblique left lateral view. Anterior is upwards and right. Scalebar 8.5*6.5 cm.

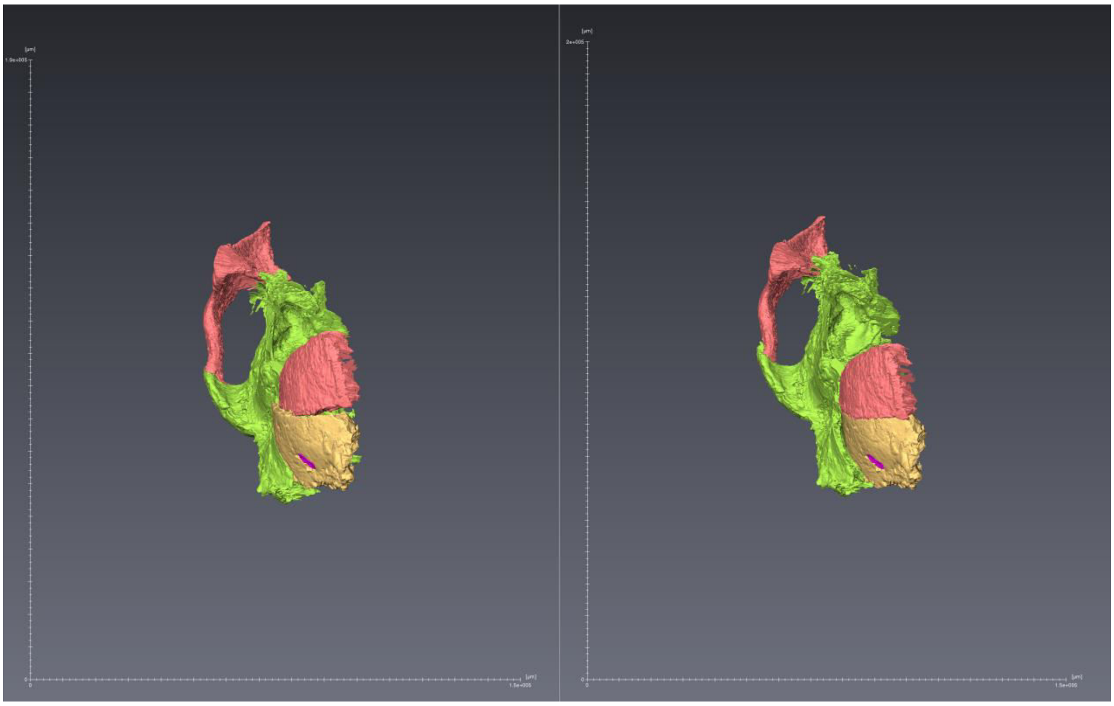

Figure 8. The zugomaticotemporal suture of original model (left) and after reconstruction in *Model 1a* (right). Dorsal views. Scalebar 20*15 cm

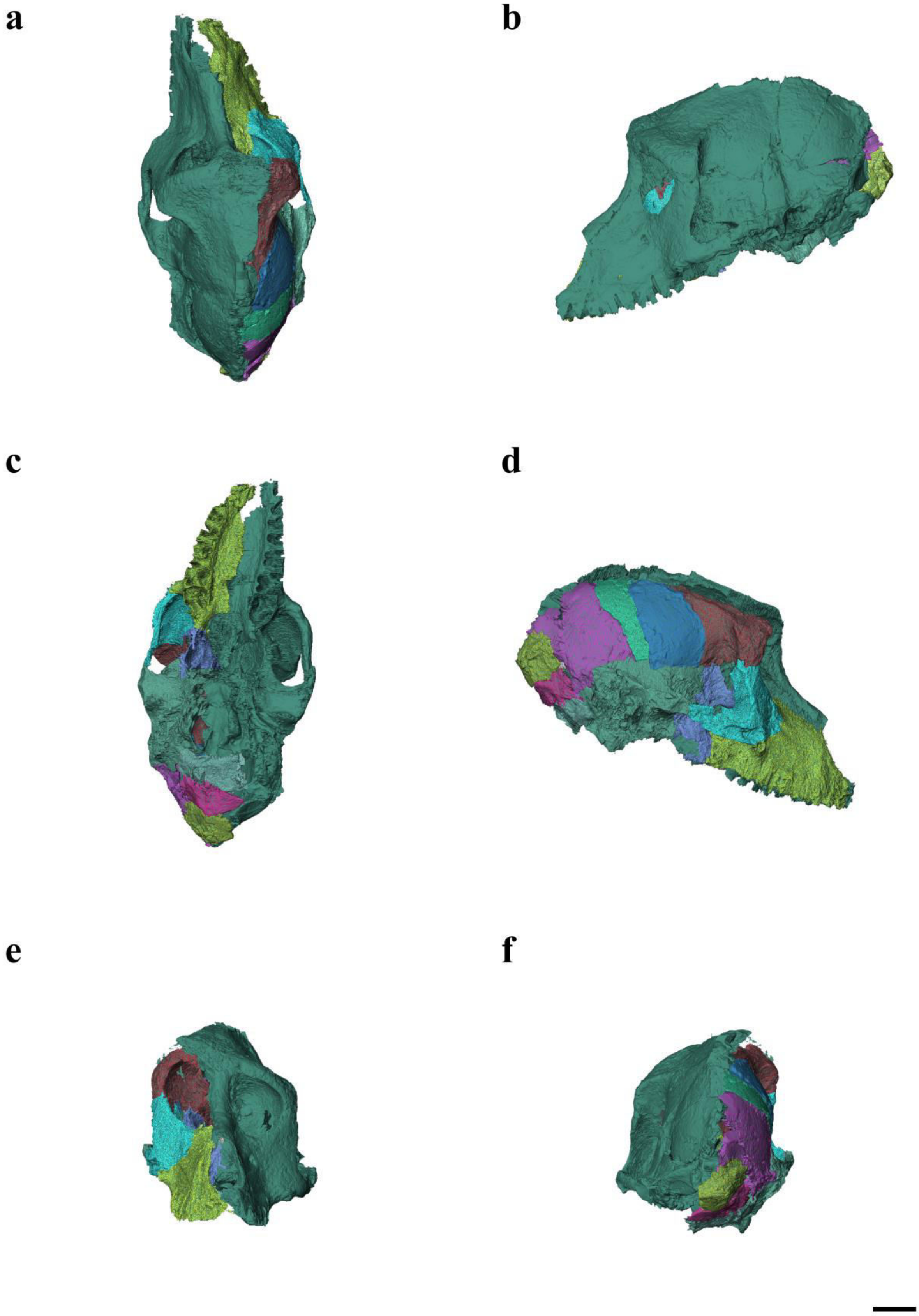

Figure 9. *Model 1a*, in dorsal (a), left lateral (b), ventral (c), right lateral (d), frontal (e) and posterior (f) view. Scalebar 2 cm.

Model 1b

Keeping the left bilateral surfaces intact, using the *Model 1a* configuration, the spread of the right bilateral components followed the initially strategy of "palatine reconstruction". Here the right maxilla-zygomatic pair is kept isolated by the rest of the fragments, while the right frontal segment lays in its original position, in contact to the left frontal fragment (Fig. 10a, f). This displacement optically reveals the greater degree of deformation that the right side of the viscerocranium suffered (Fig. 10e). The right orbital cavity is extremely elongated in a dorso-ventral direction. The temporal process of the zygomatic is inferiorly positioned as well (Fig 10d, e), while a significant gap in the right fronto-zygomatic suture is evident (Fig. 10e, f). This preferential reposition is evident is the right sphenoid as well, since it was kept in contact to the intact right frontal and third parietal (Fig. 10c). While in this model the main concern was to keep the calvaria roof solid, by means of not adjusting fragments to the new inferior position of the right maxilla, whereas keeping them as initially reported, the new width acquired from this "position" is evident across the whole cranium.

Again, the effect of width is evident, mainly in the basicranium (Fig. 10c), changing the same proportions. Alternatively, in this model, the right maxillary fragment was positioned more closely to the left maxilla (*SFig. 21*), that way closing the intermaxillary suture "gap" observed before, and narrowing the width of the palate. Anyway, this did not lead to a continuously narrow form all across the cranium, since here, the rest of the fragments where repositioned following the "new" right frontal segment. While the conclusions are kept at a minimum, and are referred to the basicranium, especially the bulk foramen magnum countour, any altered position is not capable of reforming this characteristic, mainly driven by intermaxillary width. This may not follow an originally wider cranium shape for sure, rather is the effect of a compressed neurocranium, which originally could lay more caudally and less high, gaining a more globular shape. Another potential that could describe the observed micro-morphologies, is that of inaccurate fragment reposition between those two models.

The angular nature of the individual segments isn't considered a good factor for repositioning the fragments. A fragment with many facets in its boundaries can lead to ambiguous decisions for repositioning it, when other criteria are meant to be satisfied in parallel, like symmetry, optimal fitness, and smoothness. This would require extremely careful maneuver of the fragments, especially in such a deformed specimen like LGPUT DFN3-150 cranium. In any case, when necessary, the "best" position of the fragments is approximated.

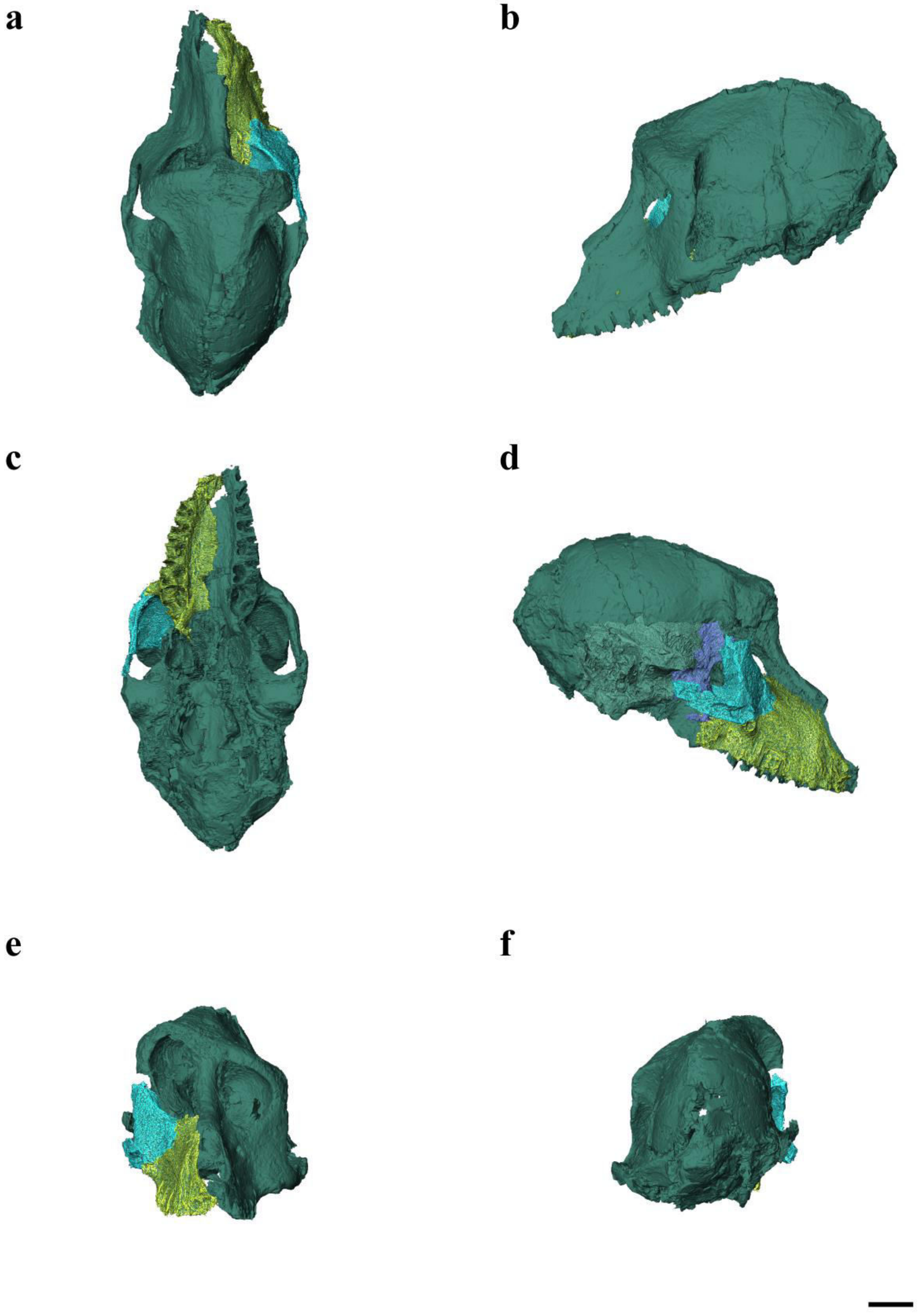

Figure 10. *Model 1b*, in dorsal (a), left lateral (b), ventral (c), right lateral (d), frontal (e) and posterior (f) view. Scalebar 2 cm.

Model 2

In order to further expand the reconstructions' envelop, a model based on mirror imaging the left fragments and projecting them on the right side is presented (Fig. 11). The reason that the left neurocranial fragments were chosen to be mirrored, while the right ones seem to preserve a more globular shape in the neurocranium, is that those in the right wouldn't "fit" to the undeformed left viscerocranial ones. In respect to that condition, all left fragments where mirrored (#13). Fragments that do not share a bilateral counterpart, like the **Occ-1**, **Occ-2** in the basicranium, and **Nas** in the viscerocranium, create "crests" when mirrored and combined. This effect is mostly evident in the occipitals, but the nasals present it as well, if examined more carefully. Once the model was created, in order to solidify it, a (virtual) extant, young adult *Papio anubis* specimen, which originally is housed at PALEVOPRIM institute, was warped via the application of a surface mapping method, based on a set of homologous landmarks. Here, a deformation matrix between the landmark sets is calculated and then extrapolated to the deformation of the surface to match the reference onto the DFN3-150 *Model 2* target (Fig. 12).

This non-taxonimical landmark application, targets to "modify" the shape of the template (Table 3; *SFig. 22*), which is the *Papio anubis* specimen, and reshape it onto the reconstructed *Model 2* of the LGPUT DFN3-150 cranium. This is done by allocating landmarks across those two, each time, one by one landmarks, creating unique pairs for the template and the host (*SFig. 23*). The more landmarks used the better the warp, but still, it serves neither a taxonomic use nor any scientific value in general, rather than it represents a rough "visual" estimation of completeness for the mirrored model. In this procedure, twenty one anatomical landmarks and several **not** equally distanced were distributed on both *Papio anubis* and DFN3-150 *Model 2*. The reason that the rest of landmarks were not equidistant is that they **do not** represent curve and surface semilandmarks, which are of different principles, functions and set up in general (Gunz and Mitteroecker, 2013).

Before applying a "bilateral symmetry reconstruction", some other issues should be handled. The initial segmentation has led to a more or less solid frontal bone, which by rather "abstract" criteria was divided into two segments, both starting caudally from the bilateral coronal sutures, and terminating rostrally to the fronto-syzgomatic sutures and nasal segment, approximately around dacryon. To apply the mirroring protocol, one has to appoint a plane in which to project fragments on both sides. In order to produce a biologically meaningful surface, the midsagittal plane was used. Since no numerical application was further applied to define and "cut" the fragments in the midsagittal (e.g. Benazzi et al., 2011), the left frontal fragment was mirrored (*SFig. 24*). Then, when the two counters would meet, approximately at a nasion-glabella plane, the protruding parts of the two frontals were sectioned, and a new supraorbital torus was generated based solely on the left frontal surfaces (*SFig. 25*).

So as to meet the original segmented model, no alternations in the left side besides the first parietal reposition were conducted, following models *1a* and *1b* (*SFig. 26*). The mirrored fragments were positioned using the "Transformation Editor" in Avizo. Here, an exact inversion of the coordinates along the horizontal plane was chosen, so as all the mirrored fragments would follow the mirrored left frontal position. This was achieved by extracting its "mirrored", inverse Y (left-right) coordinate, and applying it to the other fragments (*SFig. 27*). The results are rather unreliable. The new palatine "roof" is very wide (Fig. 11), and while from a lateral view it may seem that a perfect cover of the mirrored fragments from the left ones is achieved, a closer look at the basicranium, where the pterygoid process and the maxilla tuberocity meet, reveal a mismatch. This is due the insufficient repositioning between the left temproro-sphenoid and left maxilla at the *Model 1b* reconstruction. This is just a minor defect, since it wouldn't directly influence any morphometric landmark-based measurement, if the present width of this model – affecting all morpholandmarks – is of concern.

Table 3. Anatomical "2-set landmarks" used on both extant *Papio anubis* and *Model 2* for shape warping.

Anatomical landmark[4]	**Parts**[5]	**Description**
Rhinion	single	most anterior point in midline on the nasal
Nasion	single	middle of fronto-nasal suture
Glabella	single	most anterior point of the frontal
Frontomalare temporale	bilateral	crossing point of frontozygomatic suture and lateral edge of zygoma
Frontomalare orbitale	bilateral	crossing point of frontozygomatic suture and the inner orbital rim
Dacryon	bilateral	junction of frontal, lacrimal and maxilla
Zygo-max superior	bilateral	superior point of zygomaxillary suture
Mid-torus inferior	bilateral	inferior margin of superaorbital torus
Inion	single	most prominent projection of the protuberance
Opistion	single	most posterior point of foramen magnum
Posterior occipital condyles	bilateral	most posterior edge of occipital condyles
Porion	bilateral	upper margin of auditory meatus
Pterion	bilateral	region where the frontal, temporal and sphenoid join

[[4]Landmarks follow Kynigopoulou et al. (2017); [5]points are not absolutely positioned in the midline due to shape deformation].

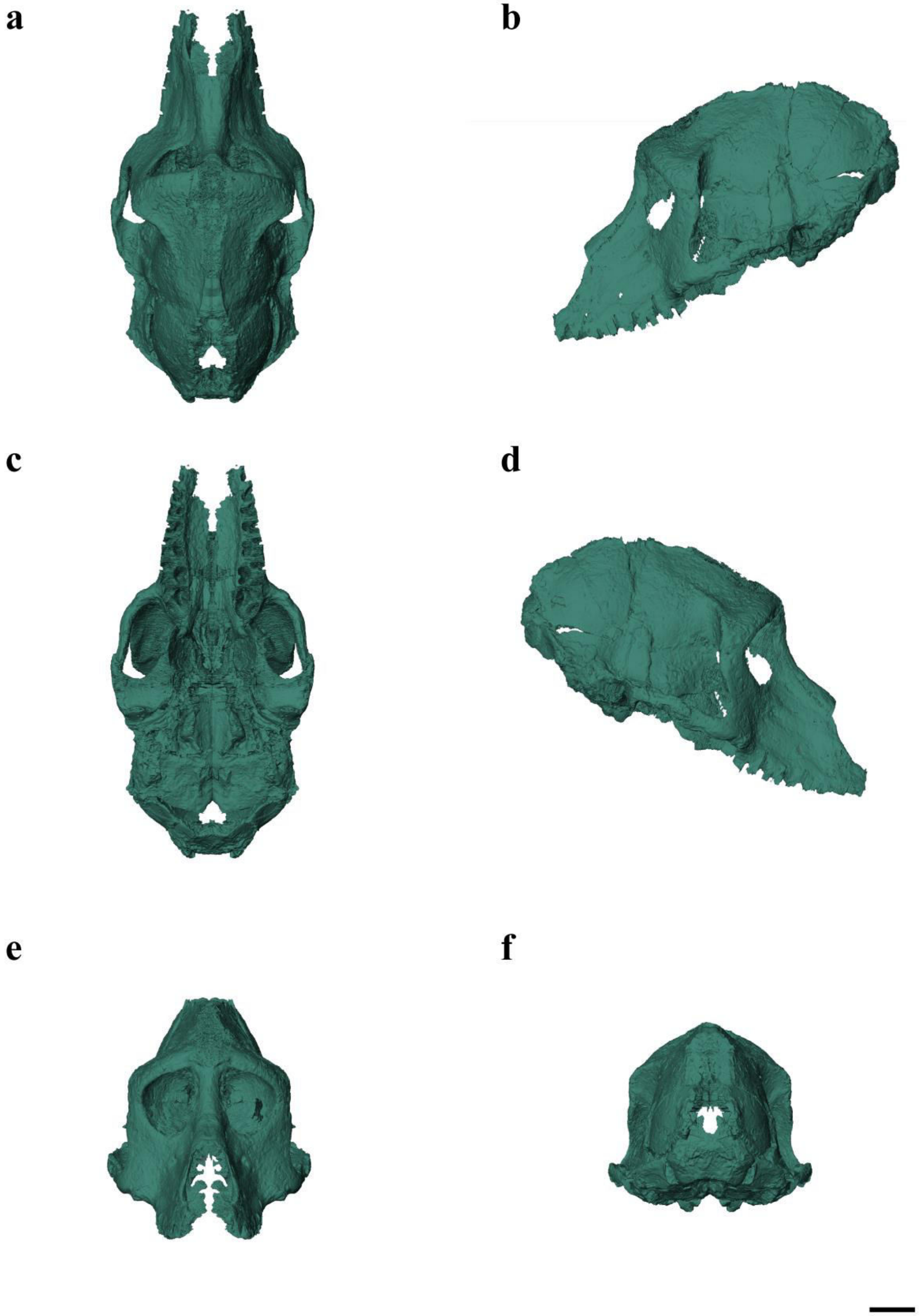

Figure 11. *Model 2* in dorsal (a), left lateral (b), ventral (c), right lateral (d), frontal (e) and posterior (f) view. Scalebar 2 cm.

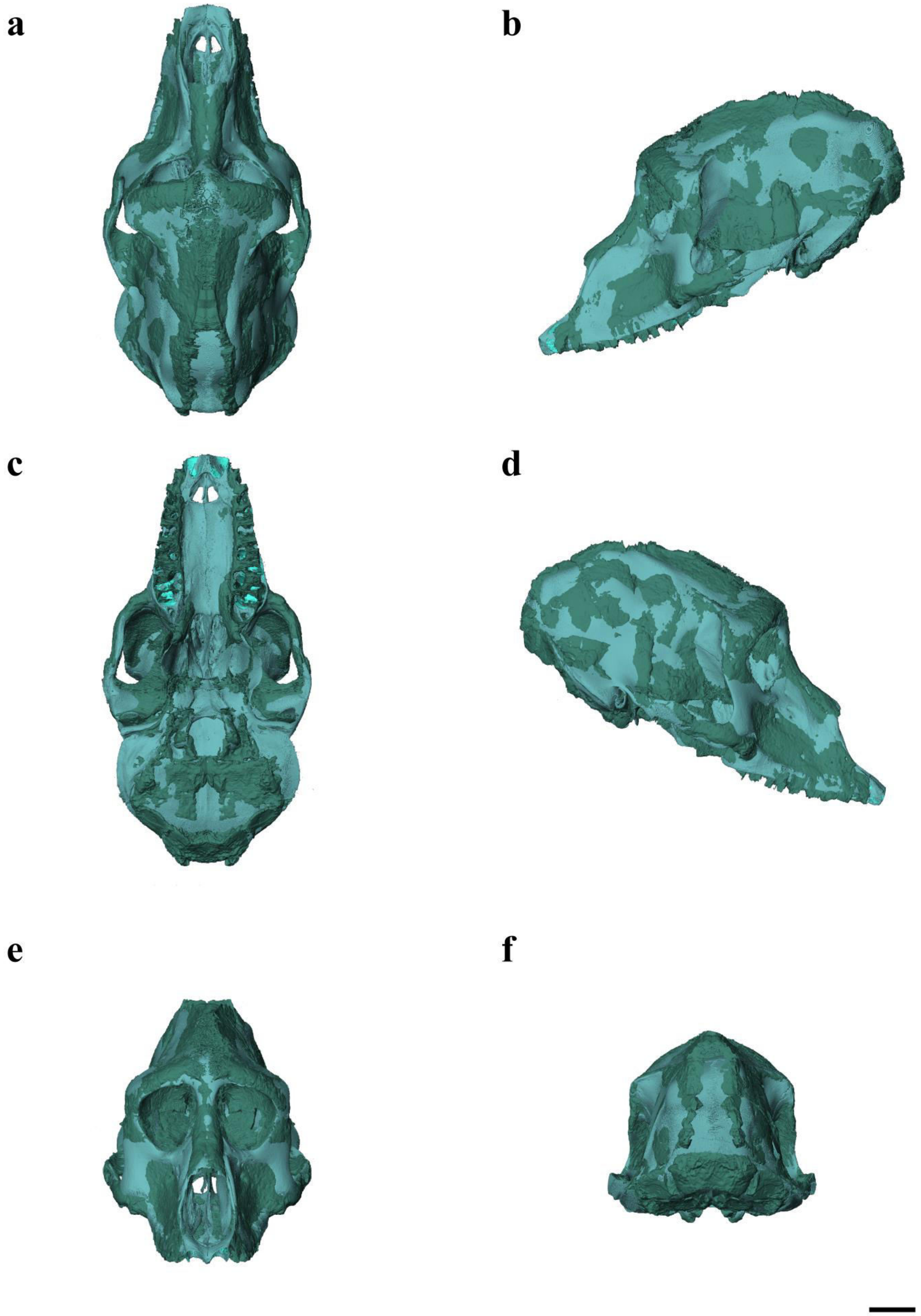

Figure 12. *Model 2* warped , in dorsal (a), left lateral (b), ventral (c), right lateral (d), frontal (e) and posterior (f) view. Light blue depicts the warped *Papio anubis* specimen. Scalebar 2 cm.

In this model, **Occ-3** and **Occ-4** occipital fragments are kept in contact with the temporo-sphenoid and first parietal, with **Occ-4** fragment relatively translated to the right, and clockwise medially rotated, so as to cover more space, and on the same time to normalize its protruding initial position (Fig. 3). The generated gap this time follows the same longitudinal direction, but is restricted rostrally from the coronal suture zone, and caudally to the lambdoid suture zone (Fig. 11). The reposition of the fourth occipital fragment lead to the widening of the existing gap between the second, third and fourth occipitals, which otherwise keeps its original triangular form, but also creates an additional gap, where the second and fourth occipital fragments previously joined.

Again, the most eminent character in the basicranium is the circular foramen magnum (Fig. 11). Since this new shape persists through both reconstructions, for which the width of the cranium is considered wider, the original rostro-caudally elongated shape could be interpretated as related to compression (further justifying the long, narrow, relatively heigh neurocranial shape). In this model, the pseudo-sagittal crest evident is the initial model will persist but widens and loses its dynamic. Alternatively, a mirror related crest appears in the frontals (Fig. 11).

The area posterior to the superciliary arch, as far as at the level of bregma and between the end of the left temporal line, is positioned in an oblique direction as opposed to its right – deformed – counterpart in the original specimen. This inclination, translated as an elevation, is responsible for the creation of the pre coronal pseudo-crest is this particular model, whiles the post coronal pseudo-crest accompanying the original specimen, is a matter of the fused nature of the superior parts of the calvaria bones on both sides of the midsagittal (*SFig. 28*).

Another evident character occurs in the frontal view (Fig. 11). While in the original specimen, both genuine and virtual, the supraorbital torus follows an elevation scheme from left to the right supraorbital margin, the countour of the torus is linear (Fig. 5) (*SFig. 29*). The same does not apply for the mirrored model. Even if the left side bares some degree of plastic deformation, in addition to the *in vivo* state, the new contour is strongly curved. Maintaining its robust character and the "weak depression at the glabella region" (Kostopoulos et al., 2018; 180), *Model 2* is rather very different than the original specimen, as well as compared to the previous reconstructions. These *in silica* observations trigger questions regarding the validity of the virtual models, but not less about the initial shape of the specimen and the deformation pattern.

CHAPTER 4. DISCUSSION

It is of course of paramount importance to assess a certain bias in a provided reconstruction. This shall "guide" the process whiles maintaining the digital specimens' integrity, constituting it a basis of further interpretation. On that behalf, any "hard" specimen introduces its own challenges, while the purpose of the reconstruction leads on its own way aspects of the workflow. In order to assign a valid midsagittal plane on the specimen, later on which the mirroring and "maximum fit" of the fragments will depend on, in a meaningful way, both computational and anatomical criteria could be used (Benazzi et al., 2011; Haile-Selassie et al., 2019; Harvati et al., 2019; Zollikofer et al., 2005, 1995).

The different degrees of deformation in a bilateral sense, which more or less accounts for LGPUT DFN3-150 cranium, could be assessed by computational manners, using landmarks and semilandmarks. Schlager et al., (2018) proposed a taxonomically unbiased method to assess bilateral deformation, which though won't perform ideally in specimens with unilateral deformation. This in turn accounts for LGPUT DFN3-150 cranium, for which the further application of target specimens, of close taxonomical or geometrical proximity (e.g. Cirilli et al., 2020; Haile-Selassie et al., 2019) would be debatable, if the whole *Paradolichopithecus* discussion is to be considered (Kostopoulos et al., 2018; Maschenko, 2005; O 'Shea et al., 2016).

But this shall be only part of the problem. LGPUT DFN3-150 cranium is both plastically deformed and fragmented. This would trigger the question of how to handle a future reconstruction in general. Should it be mechanically reconstructed prior to "retrodeforming" it, even if this fragmentary aspect refers solely to **lPar-1** fragment (Fig.2, 7), and what would be the criteria of using or excluding this initial fragment, so as to let the specimen behave like it lacks it from the begining? This series would become more complicated if the extraction of the virtual endocast is the purpose of the reconstruction after all (Gunz et al., 2020b; Haile-Selassie et al., 2019).

In terms of comparing the initial specimen and *Model 2*, which would account as the most "solid" of the three reconstructions, though not explicitly, the main ambiguous morphological characters that present a clear interest are the shape of the **supraorbital torus**, the **contour of the foramen magnum**, for which a more circular shape is evident in all three models and t**he shape of the vault**, expressed as a function of height, width and length. The prominent angular contour of the torus in *Model 2*, which is steeper in the mesophryon, shaping an obtuse angle for the whole rostral part of the frontal, can't be the real case. No known complete female *Paradolichopithecus* specimen holds this character, neither *Par. arvernensis* nor *Par. sushkini* (Depéret, 1929: Fig. 1; Trofimov, 1977: Pl. 1, B, C; Maschenko, 2005: Fig. 11, A). Male crania of *Par. sushkini* lack it as well (Nishimura et al., 2007: Fig. 2d, e; Takai et al., 2008: Fig. 3d, e), even the subadult PIN 3120-524 partial cranium, for which the torus is preserved. The same applies for the Romanian *Par. arvernensis* specimen ISER VGr/ 345 (O 'Shea et al., 2016), which was rather assigned in *Par. arvernenis* species with a possible *geticus* subspecies nomen left open for comparison to future findings (Delson and Nicolaescu-Plopsor, 1975; Radulescu et al., 2003).

This context would justify the false nature of *Model 2*, even if we consider the age (subadult), sex (female) and geographical location (E. Mediterranean) of LGPUT DFN3-150, and ontogenetic trajectories in Papionini in general. As ontogenetic shape differences among sexes are not that prominent before adulthood, even if extreme size related cases are included (Leigh et al., 2006, 2003), it seems that a torus countour as expressed in LGPUT DFN3-150 isn't realistic, when opposed to subadult PIN 3120-524, and later expressed in all males and females of the sample. Still, even if a species doesn't seem to follow a specific geographical pattern, in addition to extant Papionina (Leigh et al., 2006), adult forms seem to follow more or less the same torus shape despite their origin.

In terms that *Model 2* torus shape is the true condition, a significant difference in ontogeny, must account for more or less the same peramorphic shape. In this notion, LGPUT DFN3-150 cranium shouldn't be assigned at the *Paradolichopithecus* species at all, situation that falls way beyond all available information provided by the specimen so far, in an absolute and comparative way (Kostopoulos et al., 2018). Anyway, this weird frontal bone shape in *Model 2* wouldn't count for an age related character, in a sense that a prominent supraorbital region would be expected as a function of aging (Joganic and Heuzé, 2019), rather than phylogeny on its own, even if the variation of shapes is evident among different taxa (Hylander et al., 1991).

The same would apply for the ventral occipital countour. In *Model 2* it seems that this profile takes a trapezoidal form, resembling more to the holotype UCBL-FSL 41336 specimen from Senéze, France and the Romanian ISER VGr/ 345. This is due to the differential positioning of the **Occ-4** fragment within the left ones, in a way to delimit the posterior gap, while not altering the nuchal crest, which is beautifully shaped in the **Occ-3** fragment. This was not applied to the other models (*1a*, *1b*), and it affects significantly the countour shape and the underlying interpretation, especially if we consider that the ventral countour accounts as one of the few differentiating characters among published crania for *Paradolichopithecus* (Kostopoulos et al., 2018).

Thus, LGPUT DFN3-150, indicates the true nature of the ventral occipital contour in the female *Paradolichopithecus arvernensis* species, as observed in different ages. This coincides with the Joganic and Hauze (2019) study on female baboons, where no indication of significant age related alteration of the neurocranial shape was found. On the contrary, elderly specimens seem to present a more "prominent inion" (Joganic and Heuzé, 2019:223). Still, the very **Occ-4** fragment retains a certain degree of plastic deformation, and so it could indeed take a more "semicircular" shape, such as the female PIN 3120-523 *Par. sushkini* from Kuruksay, Tajikistan (Trofimov, 1977: Pl. II, D)

The same "taxonomic overlap" applies for the temporal lines, for which *Model 2* seems to resemble those of the female adult *Par. sushkini* PIN 3120-523 specimen, with temporal lines that do not converge. This described character though needs special care when interpreted, since deformation isn't minimized for the frontal bone, as well as the left temporal, discouraging valid assumptions, in the same degree as for the ventral occipital contour. The high degree of deformation wouldn't be the solely cause of false interpretation.

The status of reconstructions depends on the constraints applied. Indicative of this phenomena could be the initially reported "parallel molar series" that *Par. arvernensis* should present (Kostopoulos et al., 2018:188). A closer look at (Fig. 11e) would provide a clue on the effect of constrain application. *Model 2* was built on correcting for the left frontal segment, in an approximate sagittal plane preserved in this segment. This means that the mirrored left maxilla would not be corrected for this molar specific taxonomic criterion (parallelism), that way making it harder to drive absolute conclusions.

Another important observation that contrasts the original descritption of LGPUT DFN3-150 cranium is the shape of the foramen magnum. An oval shape was initially reported, but all three reconstructions (models *1a, 1b, 2*) present a circular shape for the foramen magnums' countour. This on it's own is of unknown phylogenetic value, in a conservative sense (Lieberman et al., 2000), since traditionally most studies deal with morphometrical aspects of the basicranium, thus the relative position of the foramen magnum, in accordance to bipedal and quadropedal locomotion and posture (Villamil, 2017 and referenses therain; Zollikofer et al., 2005). Nevertheless, an ontogenetic relationship between the viscrocranium and basicranium is expected (Profico et al., 2017).

So, a theoretic expectation to be exploited, for the basicranium in *Model 2*, is to seek whether a specific shape covariance among different *Paradolichopithecus* and further Papionina taxa is revealed, between the basicranium, the vault and their face, or ideally, if a particular intraspecies allometry pattern between LGPUT DFN3-150 and UCBL-FSL 41336 from Senéze, France is applied. Anyway, differences in basicranial shape may be explained, as mentioned before, by functional aspects, at a higher taxonomical level though (Profico et al., 2017). Adding on, an evolutionary allometric trend in size, and later shape (Singleton, 2002), explaining environmental conditions rather than phylogeny (Ito et al., 2011) should be found, interpreted and excluded.

On that behalf, it is interesting to mention the fact that postcranial elements of *Paradolichopithecus* may be indicative of a more bipedal posture and locomotion, resembling that of Australopithecines and trained macaques (van der Geer et al., 2006), and a possible further study of *Paradolichopithecus* foramen magnum may reveal accordingly interesting results (e.g. Zollikofer et al., 2005). Still, the face of LGPUT DFN3-150 was not repositioned at any direction, but was rather widened, due to the initial palatal overlap correction, but the strong craniofacial integration in Papionini, and especially *Papio* (Monson, 2020), could provide a trustworthy basis for the use of other, less deformed *Paradolichopithecus* crania, in order to contextualize the "novel" LGPUT DFN3-150 foramen magnum shape and possible position, even if a developmental approach to resolve the ancestry of the cranium towards the *Macaca-Papio* "stand" would be rather difficult, due to their shared trajectories (Singleton, 2002).

The newly obtained shape (Fig. 11e, but better in Fig. 12e) is much alike that in the female adult UCBL-FSL 41336 *Par. arvernensis* from Senéze, France (Depéret, 1929: Pl. 1, a), while approximating that of the male adult ISER VGr/ 345 *Par.arvernensis* from Graunceanu, Romania (O 'Shea et al., 2016) and to a lesser extent, that of adult female PIN 3120-523 *Par. sushkini* from Kuruksai, Tajikistan (Trofimov, 1977: Pl. II, D). In the latter two, the foramen magnum gets narrower towards basion, and gains maximum width exactly at the posterior occipital condyles landmarks. The French specimen contradicts both of them, by maintaining a more circular countrour from basion to opisthion, and gaining its maximum breadth at approximately the center of the occipital condyles level. Hence, by terms of maximum width, *Model 2* resembles the Romanian and Kuruksai specimens, and by means of a circular shape that from Senéze, France. Still, caution on the interpretation of these robust comparisons is recommended, due to the unknown degree of deformation that the vault has suffered, which may not account only for the "restored" width, and the potential shortening of the opisthocranium (in *Model 2*), altering the position of the foramen magnum in a more posterior relative place. The same could apply for its orientation.

The deformation of the vault, would mainly account for its gained height, due to the fusion of the parietals in a bilateral sense (*Sfig. 1*). This would be further supported by the fragmentary nature of the left side parietals, for which the deformation caused by the transverse "crack" seems to compress the vault, as well as the plastic deformation pattern observed in the underlying left temporal (Fig. 2). In combination, and since the left side was used to "mirror-reconstruct" the form, the vault may have had a less high profile. In terms of reconstruction choice, this may sound contradictory. Still, we have to consider that the left side neurocranial fragments, even if they represent the most damaged ones, in a bilateral, relative sense, where chosen for the reconstruction due to their alignment status with the left side viscerocranium segments.

Nevertheless, even if this aspect is not the effect of the fused calvaria top, the dedicated fragment of which (Table 1: **Cal**; Fig. 1, 2, 4) starts way before the coronal suture and was excluded from *Model 2* reconstruction, the overall shape of the neurocranium seems to be affected by the deformation of the frontal bone, or in accordance to it. This though is expressed by means of dimensions and not by means of slopping to inion, character for which its taxonomical implications are a matter of examination (Kostopoulos et al., 2018). When *Model 2* is considered, its length reduction, due to the new positioning of **Occ-4** fragment, couldn't further differentiate its shape, since it solely affects the opisthocranium, reducing the overall squamous occipital surface though.

This condition imposes the question whether the vault exceeds in height that of the supraorbital tori. It may be impossible to judge from the current provided reconstruction. This should be searched out by the application of "retrodeformation" techniques. When the taxonomical status of LGPUT DFN3-150 among the *Paradolichopithecus* genus is considered, it seems that in both the adult female specimen UCBL-FSL 41336 from Senéze, France and the adult male ISER VGr/ 345 from Graunceanu, Romania, of *Paradolichopithecus arvernensis*, a reduced height of the vault in relation to the tori should be prominent and expected. This is a sanguine situation, if the overall degree of sexual dimorphism and allometry in shape change is considered (Frost et al., 2015; Ito et al., 2011; Kostopoulos et al., 2018), proving this character to be conservative, by means of sex and possibly geography.

A drawback on this assumption would be the case which female baboons exhibit, i.e., that of a continuous age related craniofacial shape modification throughout adulthood, which is more prominent between young adults and middle-aged adults that don't exhibit tooth loss (Joganic and Heuzé, 2019). Another descriptive morphometric study on macaques, showed that among the studied sample, both females and males present a decrease in cranial height from young adulthood to mature adulthood, while other cranial dimensions (e.g., overall cranial length, posterior basicranial length, cranial base length, intertemporal distance) change significantly but only in males (Van Minh et al., 2015).

No matter this agreement or disagreement though, this height reduction would be either followed (or not) by a further slight increase in vault height around bregma, before slopping towards inion, as seen in the available French and Romanian specimens of *Paradolichopithecus*. The same vault height posterior to supraorbital tori is shown in the adult female PIN 3120-523 *Par. sushkini* from Kuruksai, Tajikistan (Trofimov, 1977), but when the "distrorted" subadult male PIN 3120-524 partial cranium is considered, interpretation could become more complicated, as from a lateral view (Nishimura et al., 2007: Fig. 2, e; Takai et al., 2008: Fig. 3, e), the vault seems to gain a certain degree of height, just behind the right supraorbital torus.

CHAPTER 5. CONCLUSIONS

The most prominent result of the reconstruction of *Paradolichopithecus* cranium DFN3-150 from Dafnero-3, Greece is the new width that was gained, after correcting for the maxilla overlap. Between the original cranium and *Model 2*, which represents the most "solid" reconstruction, the main morphological differences demonstrated located at the right supraorbital torus and the right parietal region, anterior to the right temporal squama (*SFig. 30*). This conclusion though is biased by the nature of *Model 2*, which in turn represents a left-side duplicated mirror model. Beyond that, and considering the potential distortion of the vault, assessing other crystal-clear conclusions by studying the present provided models and especially *Model 2* would indeed be a trivial case.

The severe diagenetic deformation that LGPUT DFN3-150 cranium suffered, affected major portions of its surface but inner bones as well, further hardening safe conclusions, even if morphometric or GM methods are to be applied to this and a comparative sample. This should of course be the suggestion, in order to somewhat enlight one of the most interesting cases in paleoprimatology. The method applied to retrodeform this specimen would be a matter of further concern, if the current (but also debatable) phylogenetic status of LGPUT DFN3-150 is considered. This is especially true, when the degree of possible differentiating variation patterns of *Paradolichopithecus* compared to extant and other fossil cercopithecines is accounted. The possibility of an age-related differentiation for this taxon in comparison to the extant taxa would just add more insecurity on that behalf.

A potential way to assess this problem is to regionally retrodeform parts of the LGPUT DFN3-150 cranium, like the supraorbital torus alone, the maxillae, or the left temporal, the opisthocranium for the vault, deploying both the reconstructions provided here and a more diverse comparative sample. Then, those retrodeformed regions of the cranium could be added on the initial fragment series, for which an extended reappraisal is rather obligatory, and the outcome should be subjected in a statistical rather than the "raw" anatomical context. This "lesser scaled" regional approach may be sufficient to discriminate phylogenetic signal as well (Grunstra et al., 2021). If a paleoneurological research proposal is pending, it would be also valuable to think whether or not a retrodeformation of the whole cranium would affect the relative position of the preserved neurological traits, or rather a bulk mechanical reconstruction would serve better the needs of this inquiry.

An imaginary "technique" would be a straight application on the CT cross sections to retrodeform shape, in accordance to a previous acquired retrodeformed vault. Still, as far as literature is considered, no attempt was made on plastically deformed crania in paleoneurological studies, at least at such a degree as in LGPUT DFN3-150. When all these are considered as a retrospective point of view, this thesis is of educational interest. Nevertheless, the results consolidate the fundamental basis on which complete research will be applied, the solid conclusions of which shall be more strictly contextualized and evaluated, through a complete comparative reference sample.

Finally, it would be wise to mention that due to the time consuming character of the segmentation progress, even if novel approaches have already been applied to solve this, in an evaluation level though (e.g. Yu et al., 2022), it is mandatory that an exhaustive assessment of the raw data, i.e. CT cross sections, should take place prior to any methodological application. On that behalf, it would be of great assistance if a quantitative, specimen-specific "scale of techinques' performance" could be developed. Still, any choice depends on the subject studied. For that in particular, it is not irrelevant that a paleoneurological study could follow.

Broading the existing framework of research for LGPUT DFN3-150 (Plastiras, 2021; Le Maitre et al., submmited) by means of subject and manners, paleoneurology has much to contribute. Within a reasonable context of rationalism, paleoneurological criteria could shed light on matters of phylogeny, therefore could be a useful tool in the study of the taxonomic affinities of LGPUT DNF3-150, and *Paradolichopithecus* ancestry within the Papionini clade (Beaudet et al., 2016; Gonzales et al., 2015; Kostopoulos et al., 2018; Maschenko, 1994, 2005; Montgomery et al., 2010; O 'Shea et al., 2016). Following the historical consensus, the first *Paradolichopithecus* specimen described by Depéret (1929) was attributed, due to wrong criteria, to the colobine *Dolichopithecus* lineage (Szalay and Delson, 1979). Besides the rest of its cercopithecine craniodental characters, the specimen proves to follow, the first to be described, clearly cercopithecine sulcal (gyrification/ cerebreal imprints on brain endocasts) pattern of the brain in the fossil record (and literature), when, on the opposite, the colobine pattern, refers to a *Mesopithecus pentelici* endocast (Falk, 1978; Radinsky, 1974).

Further on, the *Paradolichopithecus* endocast from Senéze, France, shows sulcal affinities that strongly resemble that of extant *Papio* and *Theropithecus* samples, but "*the fossil endocast is relatively lower in the occipital region than are the modern forms*", Radinsky (1974: 24). Following this, Maschenko (1994: 27), in his study on the *Par. sushkini* male juveline specimen PIN 03120-524 from Kuruksay, Tajikistan, reports weakly preserved sulcal impressions, "*impressiones qurorum*" and "*juga cerebralia*", alongside to other charecters preserved on the inner table of the frontal bone (Maschenko, 1994: Fig. 6, A). Those imprints could be of great comperative value.

Nevertheless, while the main focus should be put in the retrieve of distinct Macacina and Papionina sulcal characters (Connoly, 1950; Amiez et al., 2019; Bouchet et al., 2019; Falk, 1981) within the fossil record, a potential absence of a structural impression in an endocast, shouldn't be indicative for interpretation, in respect to the presence of another (Beaudet et al., 2016), an anatomical "coincidence" which leaves much in doubt for the use of imprints in general, especially in such deformed crania as LGPUT DFN3-150.

Following the phylogenetical potential, an interesting result was that of Beaudet et al. (2016), who showed that the *Cercopithecoides williamsi*, MP 36 and MP 3a specimens from the South African Plio-Pleistocene, present derived papionin-like cortical features, despite the fact that the species is described as the first definite ancestor of the extant African colobine clade (Frost et al., 2015). This contradiction allows the conduct of conservative conclusions, regarding a hypothecical ancestral taxon, which exhibits habitual (terrestriallity) and cortical (Papionin-like) signals, different from extant colobines, and derived, or even autapomorphic, opposed to *Mesopithecus*, when a sulcal pattern is concerned (Beaudet et al., 2016). Still, when the endocast of the stem taxon *Victoriapithecus macannesi* is considered, the colobine pattern seems derived in respect to the cercopithecine (Gonzales et al., 2015).

Therefore, we propose that the paleoneurological examination of LGPUT DFN3-150, and other *Paradolichopithecus* specimens, to be of vital contribution. Despite the great variability of characters that this taxon exhibits in accordance to sex, age and spatio-temporal distribution (Kostopoulos et al., 2018), there is no direct evidence that the sulcal pattern (folding pattern of the brain) in *Macaca* and *Papio* adult individuals, strongly correlates with sex, age or brain weight (Zilles et al., 2013 and references therein). On the contrary, there are considerable differences in the sulcal pattern among extinct *Theropithecus* subspieces (chronospecies), enough to justify taxonomic and phylogenetic comparisons and conclusions (Beaudet et al., 2016). Additionally, there is an age related, different degree of sulcal impression on endocasts, favoring juveline individuals (Van Minh and Hamada, 2017), like DFN3-150.

Thus, because brain size studies may have a low potential to reproduce evolutionary signals within the Papionini clade, a sulcal pattern, even in an endocast (Atkinson et al., 2015; Dumoncel et al., 2021), proves to be a trait of great reliability, consistent in a phylogenetic perspective, with a high degree of heritability (for baboons) (Zilles et al., 2013). Post-natal shape variations of the brain (formation of secondary and tertiary sulci), disturbing the paleontological "few-sample" study interpretation, are not expected for Old World Monkeys (Sawada et al., 2012), with the exception of sulci neighboring the paretioccipital sulcus in baboons, for which there is a strong relation to age and sex (Connolly, 1950). Still, such kind of intraspecific variations, are more or less of no significance in paleontology, and are controlled mainly by environmental factors (Kochunov, 2010).

Finally, a virtual endocast favors manipulations and quantitative handling, while additional brain information, like blood vessels or cranial nerves, can be assessed as well (Bouchet et al., 2019; Falk, 2012).

BIBLIOGRAPHY

Alba, D.M., Delson, E., Carnevale, G., Colombero, S., Delfino, M., Giuntelli, P., Pavia, M., Pavia, G., 2014. First joint record of *Mesopithecus* and cf. *Macaca* in the Miocene of Europe. J. Hum. Evol. 67, 1–18. https://doi.org/10.1016/j.jhevol.2013.11.001

Alba, D.M., Delson, E., Morales, J., Montoya, P., Romero, G., 2018. Macaque remains from the early Pliocene of the Iberian Peninsula. J. Hum. Evol. 123, 141–147. https://doi.org/10.1016/j.jhevol.2018.07.005

Antoniades, V., Penolidis, T., Dardiotis, G., 2009. History of ancient philosophy (1st ed.) Athens: Crateros. ISBN 978-960-89886-1-3 (in greek).

Amano, H., Kikuchi, T., Morita, Y., Kondo, O., Suzuki, H., Ponce de León, M.S., Zollikofer, C.P.E., Bastir, M., Stringer, C., Ogihara, N., 2015. Virtual reconstruction of the Neanderthal Amud 1 cranium: VIRTUAL RECONSTRUCTION OF AMUD 1 CRANIUM. Am. J. Phys. Anthropol. 158, 185–197. https://doi.org/10.1002/ajpa.22777

Amiez, C., Sallet, J., Hopkins, W.D., Meguerditchian, A., Hadj-Bouziane, F., Ben Hamed, S., Wilson, C.R.E., Procyk, E., Petrides, M., 2019. Sulcal organization in the medial frontal cortex provides insights into primate brain evolution. Nat. Commun. 10, 3437. https://doi.org/10.1038/s41467-019-11347-x

Atkinson, E.G., Rogers, J., Mahaney, M.C., Cox, L.A., Cheverud, J.M., 2015. Cortical Folding of the Primate Brain: An Interdisciplinary Examination of the Genetic Architecture, Modularity, and Evolvability of a Significant Neurological Trait in Pedigreed Baboons (Genus *Papio*). Genetics 200, 651–665. https://doi.org/10.1534/genetics.114.173443

Babalola, A.M., 2019. Visualization of Voxel Volume Emission and Absorption of Light in Medical Biology. Curr. Trends Biostat. Biom. 1. https://doi.org/10.32474/CTBB.2019.01.000114

Bagley, B., Sastry, S.P., Whitaker, R.T., 2016. A Marching-tetrahedra Algorithm for Feature-preserving Meshing of Piecewise-smooth Implicit Surfaces. Procedia Eng. 163, 162–174. https://doi.org/10.1016/j.proeng.2016.11.042

Balzeau, A., Grimaud-Hervé, D., Détroit, F., Holloway, R.L., Combès, B., Prima, S., 2013. First description of the Cro-Magnon 1 endocast and study of brain variation and evolution in anatomically modern *Homo sapiens*. Bull. Mém. Société Anthropol. Paris 25, 1–18. https://doi.org/10.1007/s13219-012-0069-z

Barequet, G., Vaxman, A., 2008. Nonlinear Interpolation between Slices. Int. J. Shape Model. 14, 39–60.

Beaudet, A., Dumoncel, J., de Beer, F., Duployer, B., Durrleman, S., Gilissen, E., Hoffman, J., Tenailleau, C., Thackeray, J.F., Braga, J., 2016. Morphoarchitectural variation in South African fossil cercopithecoid endocasts. J. Hum. Evol. 101, 65–78. https://doi.org/10.1016/j.jhevol.2016.09.003

Beaudet, A., Gilissen, E., 2018. Fossil Primate Endocasts: Perspectives from Advanced Imaging Techniques, in: Bruner, E., Ogihara, N., Tanabe, H.C. (Eds.), Digital Endocasts. Springer Japan, Tokyo, pp. 47–58. https://doi.org/10.1007/978-4-431-56582-6_4

Belmaker, M., 2010. The presence of a large cercopithecine (cf. *Theropithecus* sp.) in the •Ubeidiya formation (Early Pleistocene, Israel). J. Hum. Evol. 11.

Benammi, M., Aidona, E., Merceron, G., Koufos, G.D., Kostopoulos, D.S., 2020. Magnetostratigraphy and Chronology of the Lower Pleistocene Primate Bearing Dafnero Fossil Site, N. Greece. Quaternary 3, 22. https://doi.org/10.3390/quat3030022

Benazzi, S., Bookstein, F.L., Strait, D.S., Weber, G.W., 2011. A new OH5 reconstruction with an assessment of its uncertainty. J. Hum. Evol. 61, 75–88. https://doi.org/10.1016/j.jhevol.2011.02.005

Berger, M., Yang, Q., Maier, A., 2018. X-ray Imaging, in: Maier, A., Steidl, S., Christlein, V., Hornegger, J. (Eds.), Medical Imaging Systems, Lecture Notes in Computer Science. Springer International Publishing, Cham, pp. 119–145. https://doi.org/10.1007/978-3-319-96520-8_7

Bookstein, F.L., 1991. Morphometric Tools for Landmark Data: Geometry and Biology. Cambridge University Press, Cambridge

Bosma, M., 2000. Iso-Surface Volume Rendering: speed and accuracy for medical applications. Ph.D. Thesis, University of Twente, 142pp.

Bosman, A.M., Buck, L.T., Centeno, H.R., Lahr, M.M., Stringer, C., Harvati, K., 2019. Modern human origins and dispersal, Words, bones, genes, tools. Kerns Verlag, Tübingen.

Bouchet, F., Ribéron, A., Heaton, J.L., 2019. The inner craniodental anatomy of the *Papio* specimen U.W. 88-886 from the Early Pleistocene site of Malapa, Gauteng, South Africa 15.

Chung, B.S., Jeon, C.-Y., Huh, J.-W., Jeong, K.-J., Har, D., Kwack, K.-S., Park, J.S., 2019. Rise of the Visible Monkey: Sectioned Images of Rhesus Monkey. J. Korean Med. Sci. 34, e66. https://doi.org/10.3346/jkms.2019.34.e66

Cignoni, P., Montani, C., Scopigno, R., Puppo, E., 2005. Optimal Isosurface Extraction, in: Visualization Handbook. Elsevier, pp. 69–82. https://doi.org/10.1016/B978-012387582-2/50006-X

Cirilli, O., Melchionna, M., Serio, C., Bernor, R.L., Bukhsianidze, M., Lordkipanidze, D., Rook, L., Profico, A., Raia, P., 2020. Target Deformation of the *Equus stenonis* Holotype Skull: A Virtual Reconstruction. Front. Earth Sci. 8, 247. https://doi.org/10.3389/feart.2020.00247

Clark, D.P., Badea, C.T., 2014. Micro-CT of rodents: State-of-the-art and future perspectives. Phys. Med. 30, 619–634. https://doi.org/10.1016/j.ejmp.2014.05.011

Connolly, C.J., 1950. The external morphology of the primate brain. CC Thomas, Springfield

Conroy, G.C., Vannier, M.W., 1984. Noninvasive Three-Dimensional Computer Imaging of Matrix-Filled Fossil Skulls by High-Resolution Computed Tomography. Science 226, 456–458. https://doi.org/10.1126/science.226.4673.456

Custodio, L., Pesco, S., Silva, C., 2019. An extended triangulation to the Marching Cubes 33 algorithm. J. Braz. Comput. Soc. 25, 6. https://doi.org/10.1186/s13173-019-0086-6

Delson, E., Nicolaescu-Plopsor, D., 1975. *Paradolichopithecus*, a large terrestrial monkey (Cercopithecidae, Primates) from the Plio-Pleistocene of southern Europe and its importance for mammalian biochronology. VIth Congress Regional Committee of Mediterranean Neogene Stratigraphy, Bratislava, pp. 91-96.

Depéret, C., 1929. *Dolichopithecus arvernensis* Depéret. Nouveau singe du Pliocène supérieur de Sénèze (Haute-Loire). Travaux et Documents des Laboratoires de Géologie de Lyon 12, 5-12

De Vos, J., Van der Made, J., Athanassiou, A., Lyras, G., Sondaar, P. Y., and Dermitzakis, M. D., (2002). Preliminary note on the late Pliocene fauna from Vatera (Lesvos, Greece). In Annales géologiques des Pays helléniques (Vol. 39, No. 3).

Di Vincenzo, F., Profico, A., Bernardini, F., Cerroni, V., Dreossi, D., Schlager, S., Zaio, P., Benazzi, S., Biddittu, I., Rubini, M., Tuniz, C., Manzi, G., 2017. Digital reconstruction of the Ceprano calvarium (Italy), and implications for its interpretation. Sci. Rep. 7, 13974. https://doi.org/10.1038/s41598-017-14437-2

Dumoncel, J., Subsol, G., Durrleman, S., Bertrand, A., Jager, E., Oettlé, A.C., Lockhat, Z., Suleman, F.E., Beaudet, A., 2021. Are endocasts reliable proxies for brains? A 3D quantitative comparison of the extant human brain and endocast. J. Anat. 238, 480–488. https://doi.org/10.1111/joa.13318

El Albani, A., Mangano, M.G., Buatois, L.A., Bengtson, S., Riboulleau, A., Bekker, A., Konhauser, K., Lyons, T., Rollion-Bard, C., Bankole, O., Lekele Baghekema, S.G., Meunier, A., Trentesaux, A., Mazurier, A., Aubineau, J., Laforest, C., Fontaine, C., Recourt, P., Chi Fru, E., Macchiarelli, R., Reynaud, J.Y., Gauthier-Lafaye, F., Canfield, D.E., 2019. Organism motility in an oxygenated shallow-marine environment 2.1 billion years ago. Proc. Natl. Acad. Sci. 116, 3431–3436. https://doi.org/10.1073/pnas.1815721116

Elliott, J.C., Dover, S.D., 1982. X-ray microtomography. J. Microsc. 126, 211–213. https://doi.org/10.1111/j.1365-2818.1982.tb00376.x

Elton, S., 2014. Macaques at the margins: the biogeography and extinction of *Macaca sylvanus* in Europe 14.

Erickson, G.M., 2005. Assessing dinosaur growth patterns: a microscopic revolution. Trends Ecol. Evol. 20, 677–684. https://doi.org/10.1016/j.tree.2005.08.012

Eronen, J.T., Rook, L., 2004. The Mio-Pliocene European primate fossil record: dynamics and habitat tracking. J. Hum. Evol. 47, 323–341. https://doi.org/10.1016/j.jhevol.2004.08.003

Falconer, I., 1997. J J Thomson and the discovery of the electron. IOP Publ. Ltd, Physics Education 32, 7. https://doi.org/10.1088/0031-9120/32/4/015

Falk, D., 2015. Evolution of the Primate Brain, in: Henke, W., Tattersall, I. (Eds.), Handbook of Paleoanthropology. Springer Berlin Heidelberg, Berlin, Heidelberg, pp. 1495–1525. https://doi.org/10.1007/978-3-642-39979-4_37

Falk, D., 2012. Chapter 12 - Hominin paleoneurology: Where are we now? 18.

Falk, D., 1981. Sulcal patterns of fossil *Theropithecus* baboons: Phylogenetic and functional implications. Int. J. Primatol. 2, 57–69. https://doi.org/10.1007/BF02692300

Falk, D., 1978. Brain evolution in old World monkeys. Am. J. Phys. Anthropol. 48, 315–319. https://doi.org/10.1002/ajpa.1330480307

Fleagle, J.G., 2013. Primate adaptation and evolution, 3rd ed. ed. Elsevier/Academic Press, Amsterdam ; Boston.

Fourie, Z., Damstra, J., Schepers, R.H., Gerrits, P.O., Ren, Y., 2012. Segmentation process significantly influences the accuracy of 3D surface models derived from cone beam computed tomography. Eur. J. Radiol. 81, e524–e530. https://doi.org/10.1016/j.ejrad.2011.06.001

Frost, S.R., 2017. Evolution of the Cercopithecidae, in: Bezanson, M., MacKinnon, K.C., Riley, E., Campbell, C.J., Nekaris, K.A.I.A., Estrada, A., Di Fiore, A.F., Ross, S., Jones-Engel, L.E., Thierry, B., Sussman, R.W., Sanz, C., Loudon, J., Elton, S., Fuentes, A. (Eds.), The International Encyclopedia of Primatology. John Wiley & Sons, Inc., Hoboken, NJ, USA, pp. 1–3. https://doi.org/10.1002/9781119179313.wbprim0064

Frost, S.R., Gilbert, C.C., Pugh, K.D., Guthrie, E.H., Delson, E., 2015. The Hand of *Cercopithecoides williamsi* (Mammalia, Primates): Earliest Evidence for Thumb Reduction among Colobine Monkeys. PLOS ONE 10, e0125030. https://doi.org/10.1371/journal.pone.0125030

Frost, S.R., Rosenberger, A.L., Hartwig, W.C., 2011. Old World Monkeys, in: John Wiley & Sons, Ltd (Ed.), ELS. John Wiley & Sons, Ltd, Chichester, UK, p. a0001561.pub2. https://doi.org/10.1002/9780470015902.a0001561.pub2

Geer, A.A.E.V.D., Dermitzakis, M.D., 2008. Dental eruption sequence in the Pliocene papionin *Paradolichopithecus arvernensis* (Mammalia: Primates) from Greece. J. Vertebr. Paleontol. 28, 1238–1244. https://doi.org/10.1671/0272-4634-28.4.1238

Gilbert, C.C., Bibi, F., Hill, A., Beech, M.J., 2014. Early guenon from the late Miocene Baynunah Formation, Abu Dhabi, with implications for cercopithecoid biogeography and evolution. Proc. Natl. Acad. Sci. 111, 10119–10124. https://doi.org/10.1073/pnas.1323888111

Gilbert, C.C., Frost, S.R., Pugh, K.D., Anderson, M., Delson, E., 2018. Evolution of the modern baboon (*Papio hamadryas*): A reassessment of the African Plio-Pleistocene record. J. Hum. Evol. 122, 38–69. https://doi.org/10.1016/j.jhevol.2018.04.012

Gonzales, L.A., Benefit, B.R., McCrossin, M.L., Spoor, F., 2015. Cerebral complexity preceded enlarged brain size and reduced olfactory bulbs in Old World monkeys. Nat. Commun. 6, 7580. https://doi.org/10.1038/ncomms8580

Grignon, B., Mainard, L., Delion, M., Hodez, C., Oldrini, G., 2012. Recent advances in medical imaging: anatomical and clinical applications. Surg. Radiol. Anat. 34, 675–686. https://doi.org/10.1007/s00276-012-0985-0

Grossman, M.I., 2021. John Dalton's "Aha" Moment: the Origin of the Chemical Atomic Theory. Ambix 68, 49–71. https://doi.org/10.1080/00026980.2020.1868861

Grosso, R., Zint, D., 2021. A parallel dual marching cubes approach to quad only surface reconstruction. Vis. Comput. https://doi.org/10.1007/s00371-021-02139-w

Grunstra, N.D.S., Bartsch, S.J., Le Maître, A., Mitteroecker, P., 2021. Detecting Phylogenetic Signal and Adaptation in Papionin Cranial Shape by Decomposing Variation at Different Spatial Scales. Syst. Biol. 70, 694–706. https://doi.org/10.1093/sysbio/syaa093

Gunz, P., 2015. Computed Tools for Paleoneurology, in: Bruner, E. (Ed.), Human Paleoneurology, Springer Series in Bio-/Neuroinformatics. Springer International Publishing, Cham, pp. 39–55. https://doi.org/10.1007/978-3-319-08500-5_3

Gunz, P., Kozakowski, S., Neubauer, S., Le Cabec, A., Kullmer, O., Benazzi, S., Hublin, J.-J., Begun, D.R., 2020a. Skull reconstruction of the late Miocene ape *Rudapithecus hungaricus* from Rudabánya, Hungary. J. Hum. Evol. 138, 102687. https://doi.org/10.1016/j.jhevol.2019.102687

Gunz, P., Mitteroecker, P., Neubauer, S., Weber, G.W., Bookstein, F.L., 2009b. Principles for the virtual reconstruction of hominin crania. J. Hum. Evol. 57, 48–62. https://doi.org/10.1016/j.jhevol.2009.04.004

Gunz, P., Mitteroecker, P., 2013. Semilandmarks: a method for quantifying curves and surfaces. Hystrix It. J. Mamm. 24, 103–109. https://doi.org/10.4404/hystrix-24.1-6292

Gunz, P., Neubauer, S., Falk, D., Tafforeau, P., Le Cabec, A., Smith, T.M., Kimbel, W.H., Spoor, F., Alemseged, Z., 2020b. *Australopithecus afarensis* endocasts suggest ape-like brain organization and prolonged brain growth. Sci. Adv. 6, eaaz4729. https://doi.org/10.1126/sciadv.aaz4729

Haidekker, M.A., 2013. Medical Imaging Technology, SpringerBriefs in Physics. Springer New York, New York, NY. https://doi.org/10.1007/978-1-4614-7073-1

Haile-Selassie, Y., Melillo, S.M., Vazzana, A., Benazzi, S., Ryan, T.M., 2019. A 3.8-million-year-old hominin cranium from Woranso-Mille, Ethiopia. Nature 573, 214–219. https://doi.org/10.1038/s41586-019-1513-8

Harris, E.E., 2000. Molecular systematics of the Old World monkey tribe Papionini: analysis of the total available genetic sequences. J. Hum. Evol. 38, 235–256. https://doi.org/10.1006/jhev.1999.0318

Harvati, K., Röding, C., Bosman, A.M., Karakostis, F.A., Grün, R., Stringer, C., Karkanas, P., Thompson, N.C., Koutoulidis, V., Moulopoulos, L.A., Gorgoulis, V.G., Kouloukoussa, M., 2019. Apidima Cave fossils provide earliest evidence of *Homo sapiens* in Eurasia. Nature 571, 500–504. https://doi.org/10.1038/s41586-019-1376-z

Holdsworth, D.W., Thornton, M.M., 2002. Micro-CT in small animal and specimen imaging. Trends Biotechnol. 20, S34–S39. https://doi.org/10.1016/S0167-7799(02)02004-8

Hounsfield, G.N., 1973. Computerized transverse axial scanning (tomography): Part 1. Description of system. Br. J. Radiol. 46, 1016–1022. https://doi.org/10.1259/0007-1285-46-552-1016

Huang, J., Mueller, K., Crawfis, R., Bartz, D., Meissner, M., 2000. A Practical Evaluation of Popular Volume Rendering Algorithms, in: Symposium on Volume Visualization and Graphics 2000. pp. 81–90. https://doi.org/10.1109/VV.2000.10009

Hylander, W.L., Picq, P.G., Johnson, K.R., 1991. Function of the supraorbital region of primates. Arch. Oral Biol. 36, 273–281. https://doi.org/10.1016/0003-9969(91)90097-E

Iniewski, K., 2009. MEDICAL IMAGING, Principles, Detectors, and Electronics. Wiley, Hoboken, N.J.

Ito, T., Nishimura, T., Takai, M., 2011. Allometry and Interspecific Differences in the Facial Cranium of Two Closely Related Macaque Species. Anat. Res. Int. 2011, 1–7. https://doi.org/10.1155/2011/849751

Itoh, T., Koyamada, K., 2005. Isosurface Extraction Using Extrema Graphs, in: Visualization Handbook. Elsevier, pp. 83–96. https://doi.org/10.1016/B978-012387582-2/50007-1

Jablonski, N.G., Leakey, M.G., Kiarie, C., Antón, M., 2002. A new skeleton of *Theropithecus brumpti* (Primates: Cercopithecidae) from Lomekwi, West Turkana, Kenya. Journal of Human Evolution 43, 887–923. https://doi.org/10.1006/jhev.2002.0607

Jablonski, N.G., Frost, S.R., 2010. Cercopithecoidea. In: Werdelin, L., Sanders, W.J. (Eds.), Cenozoic Mammals of Africa. University of California Press, pp. 393–428.

Joganic, J.L., Heuzé, Y., 2019. Allometry and advancing age significantly structure craniofacial variation in adult female baboons. J. Anat. 235, 217–232. https://doi.org/10.1111/joa.13005

Knoll, G.F., 1989. Radiation detection and measurement / Glenn F. Knoll. Wiley, New York.

Kochunov, P., 2010. Genetics of primary cerebral gyrification: Heritability of length, depth and area of primary sulci in an extended pedigree of Papio baboons 9.

Köhler, M., Moyà-Solà, S., Alba, D.M., 2000. *Macaca* (Primates, Cercopithecidae) from the Late Miocene of Spain. J. Hum. Evol. 38, 447–452. https://doi.org/10.1006/jhev.1999.0388

Kostopoulos, D.S., Guy, F., Kynigopoulou, Z., Koufos, G.D., Valentin, X., Merceron, G., 2018. A 2Ma old baboon-like monkey from Northern Greece and new evidence to support the *Paradolichopithecus – Procynocephalus* synonymy (Primates: Cercopithecidae). J. Hum. Evol. 121, 178–192. https://doi.org/10.1016/j.jhevol.2018.02.012

Koufos, G.D., 2019. Late Turolian *Mesopithecus* (Mammalia: Cercopithecidae) from Axios Valley (Macedonia, Greece): earliest presence of M. monspessulanus in Europe. Comptes Rendus Palevol 18, 1057–1072. https://doi.org/10.1016/j.crpv.2019.07.002

Koufos G.D., (2001). The Villafranchian mammalian faunas and biochronology of Greece. Bullettino della Societa Paleontologica Italiana, 40 (2), 2001, 217-223. ISSN 0375-7633

Koufos, G.D., Kostopoulos, D.S., 2016. The Plio-Pleistocene Large Mammal Record of Greece: Implications for Early Human Dispersals into Europe, in: Harvati, K., Roksandic, M. (Eds.), Paleoanthropology of the Balkans and Anatolia, Vertebrate Paleobiology and Paleoanthropology. Springer Netherlands, Dordrecht, pp. 269–280. https://doi.org/10.1007/978-94-024-0874-4_15

Koufos, G. D., Kostopoulos, D. S., and Koliadimou, K. K. (1991). Un nouveau gisement de mammifères dans le Villafranchien de Macédoine occidentale (Grèce). Comptes Rendus de l'Academie des Sciences, Paris, 313, 831-836.

Kuhn, T.S., 1951. Newton's "31st Query" and the Degradation of Gold. Isis 42, 296–298.

Kumar, T.S., Vijai, A., 2012. 3D Reconstruction of Face from 2D CT Scan Images. Procedia Eng. 30, 970–977. https://doi.org/10.1016/j.proeng.2012.01.952

Kynigopoulou, Z., Kostopoulos, D.S., Guy, F., 2017. Comparative analysis of outer and inner skull morphology between *Paradolichopithecus*/*Procynocephalus* and cercopithecines. In: 2nd International Meeting of early-stage researchers in Paleontology 2017, pp. 83e84 abstract. http://www.imerp2.upatras.gr/index.php.

Le Maitre, A., Guy, F., Merceron, G., Kostopoulos, D. S., 2021. Morphology of the bony labyrinth supports the affinities of *Paradolichopithecus* with the Papionina. submitted.

Leigh, S.R., 2006. Cranial ontogeny of *Papio* baboons (*Papio hamadryas*). Am. J. Phys. Anthropol. 130, 71–84. https://doi.org/10.1002/ajpa.20319

Leigh, S.R., Shah, N.F., Buchanan, L.S., 2003. Ontogeny and phylogeny in papionin primates. J. Hum. Evol. 45, 285–316. https://doi.org/10.1016/j.jhevol.2003.08.004

Lemert, J.R., Spocter, M.A., 2018. Evolution of the Brain, The, in: Shackelford, T.K., Weekes-Shackelford, V.A. (Eds.), Encyclopedia of Evolutionary Psychological Science. Springer International Publishing, Cham, pp. 1–5. https://doi.org/10.1007/978-3-319-16999-6_3094-1

Leng, J., Xu, G., Zhang, Y., 2013. Medical image interpolation based on multi-resolution registration. Comput. Math. Appl. 66, 1–18. https://doi.org/10.1016/j.camwa.2013.04.026

Liakopoulou, D., Georgitsis, M., Roussiakis, S., 2021. Frontal bone pneumatisation in *Tragoportax* and *Miotragocerus* (Mammalia, Bovidae) from the Late Miocene of Greece. Hist. Biol. 1–10. https://doi.org/10.1080/08912963.2021.1959578

Lieberman, D.E., Pearson, O.M., Mowbray, K.M., 2000. Basicranial influence on overall cranial shape. J. Hum. Evol. 38, 291–315. https://doi.org/10.1006/jhev.1999.0335

Livnat, Y., 2005. Accelerated Isosurface Extraction Approaches, in: Visualization Handbook. Elsevier, pp. 39–55. https://doi.org/10.1016/B978-012387582-2/50004-6

Lopes, A., Brodlie, K., 2003. Improving the robustness and accuracy of the marching cubes algorithm for isosurfacing. IEEE Trans. Vis. Comput. Graph. 9, 16–29. https://doi.org/10.1109/TVCG.2003.1175094

Lorensen, W., Cline, H., 1987. Marching Cubes: A High Resolution 3D Surface Construction Algorithm. ACM SIGGRAPH Comput. Graph. 21, 163-. https://doi.org/10.1145/37401.37422

Luccichenti, G., Cademartiri, F., Pezzella, F.R., Runza, G., Belgrano, M., Midiri, M., Sabatini, U., Bastianello, S., Krestin, G.P., 2005. 3D reconstruction techniques made easy: know-how and pictures. Eur. Radiol. 15, 2146–2156. https://doi.org/10.1007/s00330-005-2738-5

Macrini, T.E., Rougier, G.W., Rowe, T., 2007. Description of a Cranial Endocast from the Fossil Mammal *Vincelestes neuquenianus* (Theriiformes) and its Relevance to the Evolution of Endocranial Characters in Therians. Anat. Rec. Adv. Integr. Anat. Evol. Biol. 290, 875–892. https://doi.org/10.1002/ar.20551

Maier, A., Steidl, S., Christlein, V., Hornegger, J. (Eds.), 2018. Medical Imaging Systems: An Introductory Guide, Lecture Notes in Computer Science. Springer International Publishing, Cham. https://doi.org/10.1007/978-3-319-96520-8

Maschenko, E.N., 1994. Comparative morphological analysis of the skull and lower jaw of the late Pliocene baboon *Papio suschkini*. In: Tatarinov, L.P. (Ed.), Paleonteriologia. Nauka, Moscow, pp. 15-57 (in Russian).

Maschenko, E.N., 2005. Cenozoic Primates of eastern Eurasia (Russia and adjacent areas). Anthropol. Sci. 113, 103–115. https://doi.org/10.1537/ase.04S015

Meagher, D.J., 1982. Geometric modeling using octree encoding. Comput Graph Image Process 19, 129–147.

Meißner, M., Pfister, H., Westermann, R., Wittenbrink, C., 2000. Volume visualization and volume rendering techniques. Eurographics Association. https://doi.org/10.2312/egt.20001035

Mittermeier, R.A., Rylands, A.B., Wilson, D.E. (Eds.), 2013. Handbook of the Mammals of the World. Volume 3: Primates., first. ed. Lynx Ediciones, Barcelona, Spain. ISBN 978-84-96553-89-7

Monson, T.A., 2020. Patterns and magnitudes of craniofacial covariation in extant cercopithecids. Anat. Rec. 303, 3068–3084. https://doi.org/10.1002/ar.24398

Montgomery, S.H., Capellini, I., Barton, R.A., Mundy, N.I., 2010. Reconstructing the ups and downs of primate brain evolution: implications for adaptive hypotheses and Homo floresiensis. BMC Biol. 8, 9. https://doi.org/10.1186/1741-7007-8-9

Nicholls, M., 2019. Sir Godfrey Newbold Hounsfield and Allan M. Cormack. Eur. Heart J. 40, 2101–2103. https://doi.org/10.1093/eurheartj/ehz421

Nishimura, T.D., Ito, T., Yano, W., Ebbestad, J.O.R., Takai, M., 2014. Nasal architecture in *Procynocephalus wimani* (Early Pleistocene, China) and implications for its phyletic relationship with *Paradolichopithecus.* Anthropol. Sci. 122, 101–113. https://doi.org/10.1537/ase.140624

Nishimura, T.D., Takai, M., Maschenko, E.N., 2007. The maxillary sinus of *Paradolichopithecus sushkini* (late Pliocene, southern Tajikistan) and its phyletic implications. J. Hum. Evol. 52, 637–646. https://doi.org/10.1016/j.jhevol.2006.12.004

Nomade, S., Pastre, J.F., Guillou, H., Faure, M., Guérin, C., Delson, E., Debard, E., Voinchet, P., Messager, E., 2014. 40Ar/39Ar constraints on some French landmark Late Pliocene to Early Pleistocene large mammalian paleofaunas: Paleoenvironmental and paleoecological implications. Quat. Geochronol. 21, 2–15. https://doi.org/10.1016/j.quageo.2012.12.006

O 'Shea, N., Delson, E., Pugh, K.D., Gilbert, C.C., 2016. Phylogenetic analysis of *Paradolichopithecus*: Fossil baboon or macaque? https://doi.org/10.13140/RG.2.2.21089.61289

Omar, A., Andreo, P., Poludniowski, G., 2020. A model for the energy and angular distribution of x rays emitted from an x-ray tube. Part I. Bremsstrahlung production. Med. Phys. 47, 4763–4774. https://doi.org/10.1002/mp.14359

Orliac, M.J., Argot, C., Gilissen, E., 2012. Digital Cranial Endocast of *Hyopsodus* (Mammalia, "Condylarthra"): A Case of Paleogene Terrestrial Echolocation? PLoS ONE 7, e30000. https://doi.org/10.1371/journal.pone.0030000

Ou, X., Chen, Xue, Xu, X., Xie, L., Chen, Xiaofeng, Hong, Z., Bai, H., Liu, X., Chen, Q., Li, L., Yang, H., 2021. Recent Development in X-Ray Imaging Technology: Future and Challenges. Research 2021, 1–18. https://doi.org/10.34133/2021/9892152

Perrone, A., Finlayson, J.E., Bartelink, E.J., Dalton, K.D., 2014. Application of Portable X-ray Fluorescence (XRF) for Sorting Commingled Human Remains, in: Commingled Human Remains. Elsevier, pp. 145–165. https://doi.org/10.1016/B978-0-12-405889-7.00007-1

Plastiras C. A., 2021. Ecological diversity of Pliocene to Pleistocene Palaearctic cercopithecids (Primates, Mammalia); evidence from dental tissue. Ph.D. Thesis, Aristotle University of Thessaloniki, 228 pp.

Preim, B., Botha, C., 2014. Surface Rendering, in: Visual Computing for Medicine. Elsevier, pp. 229–267. https://doi.org/10.1016/B978-0-12-415873-3.00006-7

Profico, A., Piras, P., Buzi, C., Di Vincenzo, F., Lattarini, F., Melchionna, M., Veneziano, A., Raia, P., Manzi, G., 2017. The evolution of cranial base and face in Cercopithecoidea and Hominoidea: Modularity and morphological integration. Am. J. Primatol. 79, e22721. https://doi.org/10.1002/ajp.22721

Raaum, R.L., Sterner, K.N., Noviello, C.M., Stewart, C.-B., Disotell, T.R., 2005. Catarrhine primate divergence dates estimated from complete mitochondrial genomes: concordance with fossil and nuclear DNA evidence. J. Hum. Evol. 48, 237–257. https://doi.org/10.1016/j.jhevol.2004.11.007

Radinsky, L., 1974. The fossil evidence of anthropoid brain evolution. Am. J. Phys. Anthropol. 41, 15–27. https://doi.org/10.1002/ajpa.1330410104

Radulescu, C., Samson, P.-M., Petculescu, A., Stiucã, E., 2003. Pliocene large mammals of Romania. Coloq. Paleontol. ISSN 1132-1660 N^o 1 2003 Pags 549-558 1.

Rawson, J.R.G., Porro, L.B., Martin-Silverstone, E., Rayfield, E.J., 2021. Osteology and digital reconstruction of the skull of the early tetrapod *Whatcheeria deltae*. J. Vertebr. Paleontol. 41, e1927749. https://doi.org/10.1080/02724634.2021.1927749

Rocke, A.J., 2005. In Search of El Dorado: John Dalton and the Origins of the Atomic Theory. Johns Hopkins Univ. Press, Errors: Consequences of Big Mistakes in the Natural and Social Sciences 72, 125–158.

Rohlf, F.J., 1993. Contributions to morphometrics. In: Marcus, L.F., Bello, E., Garcia-Valdecasas, A. (Eds.), Museo Nacional de Ciencies Naturales, Madrid, pp. 131–159.

Röntgen, W.C., 1896. On a New Kind of Rays. Science 3, 227–231. https://doi.org/10.1126/science.3.59.227

Sawada, K., Fukunishi, K., Kashima, M., Saito, S., Sakata-Haga, H., Aoki, I., Fukui, Y., 2012. Fetal Gyrification in Cynomolgus Monkeys: A Concept of Developmental Stages of Gyrification 10.

Scatliff, J.H., Morris, P.J., 2014. From Röntgen to Magnetic Resonance Imaging: The History of Medical Imaging. N. C. Med. J. 75, 111–113. https://doi.org/10.18043/ncm.75.2.111

Schlager, S., Profico, A., Di Vincenzo, F., Manzi, G., 2018. Retrodeformation of fossil specimens based on 3D bilateral semi-landmarks: Implementation in the R package "Morpho." PLOS ONE 13, e0194073. https://doi.org/10.1371/journal.pone.0194073

Schroeder, W.J., Martin, K.M., 2005. Overview of Visualization Text and images taken with permission from the book The Visualization Toolkit: An Object-Oriented Approach to 3D Graphics, 3rd ed., published by Kitware, Inc. http://www.kitware.com/products/vtktextbook.html., in: Visualization Handbook. Elsevier, pp. 3–35. https://doi.org/10.1016/B978-012387582-2/50003-4

Seco, J., Clasie, B., Partridge, M., 2014. Review on the characteristics of radiation detectors for dosimetry and imaging. Phys. Med. Biol. 59, R303–R347. https://doi.org/10.1088/0031-9155/59/20/R303

Seibert, J.A., 2004. X-Ray Imaging Physics for Nuclear Medicine Technologists. Part 1: Basic Principles of X-Ray Production. J. Nucl. Med. Technol. 32, 139.

Seibert, J.A., Boone, J.M., 2005. X-Ray Imaging Physics for Nuclear Medicine Technologists. Part 2: X-Ray Interactions and Image Formation. J. Nucl. Med. Technol. 33, 17.

Senck, S., Bookstein, F.L., Benazzi, S., Kastner, J., Weber, G.W., 2015. Virtual Reconstruction of Modern and Fossil Hominoid Crania: Consequences of Reference Sample Choice: Virtual Reconstruction of Hominoid Crania. Anat. Rec. 298, 827–841. https://doi.org/10.1002/ar.23104

Shearer, B.M., Cooke, S.B., Halenar, L.B., Reber, S.L., Plummer, J.E., Delson, E., Tallman, M., 2017. Evaluating causes of error in landmark-based data collection using scanners. PLOS ONE 12, e0187452. https://doi.org/10.1371/journal.pone.0187452

Sianis, P.D., 2021. The cf. *Paradolichopithecus* sp. (Primates, Cercopithecidae) finds from the new Lower Pleistocene site of Karnazeika (Peloponnese, Southern Greece). 3rd Palaeontological Virtual Congress 1st-15th December 2021

Singleton, M., 2002. Patterns of cranial shape variation in the Papionini (Primates: Cercopithecinae). J. Hum. Evol. 42, 547–578. https://doi.org/10.1006/jhev.2001.0539

Smith, W.A.P., 2020. 3D Data Representation, Storage and Processing, in: Liu, Y., Pears, N., Rosin, P.L., Huber, P. (Eds.), 3D Imaging, Analysis and Applications. Springer International Publishing, Cham, pp. 265–316. https://doi.org/10.1007/978-3-030-44070-1_6

Springer, M.S., Meredith, R.W., Gatesy, J., Emerling, C.A., Park, J., Rabosky, D.L., Stadler, T., Steiner, C., Ryder, O.A., Janečka, J.E., Fisher, C.A., Murphy, W.J., 2012. Macroevolutionary Dynamics and Historical Biogeography of Primate Diversification Inferred from a Species Supermatrix. PLoS ONE 7, e49521. https://doi.org/10.1371/journal.pone.0049521

Stevens, N.J., Seiffert, E.R., O'Connor, P.M., Roberts, E.M., Schmitz, M.D., Krause, C., Gorscak, E., Ngasala, S., Hieronymus, T.L., Temu, J., 2013. Palaeontological evidence for an Oligocene divergence between Old World monkeys and apes. Nature 497, 611–614. https://doi.org/10.1038/nature12161

Stytz, M.R., Parrott, R.W., 1993. Using kriging for 3d medical imaging. Comput. Med. Imaging Graph. 17, 421–442. https://doi.org/10.1016/0895-6111(93)90059-V

Szalay, F.S., Delson, E., 1979. Evolutionary History of the Primates. Academic Press, New York.

Takai, M., Maschenko, E.N., Nishimura, T.D., Anezaki, T., Suzuki, T., 2008. Phylogenetic relationships and biogeographic history of *Paradolichopithecus sushkini* Trofimov 1977, a large-bodied cercopithecine monkey from the Pliocene of Eurasia. Quat. Int. 12.

Thomson, J.J., 1897. XL. *Cathode Rays*. Lond. Edinb. Dublin Philos. Mag. J. Sci. 44, 293–316. https://doi.org/10.1080/14786449708621070

Tolentino, E. de S., Amoroso-Silva, P.A., Alcalde, M.P., Yamashita, F.C., Iwaki, L.C.V., Rubira-Bullen, I.R.F., Duarte, M.A.H., 2021. Comparison of limited- and large-volume cone-beam computed tomography using a small voxel size for detecting isthmuses in mandibular molars. Imaging Sci Dent 51, 27–34.

Tosi, A.J., Morales, J.C., Melnick, D.J., 2003. Paternal, maternal, and biparental molecular markers provide unique windows onto the evolutionary history of macaque monkeys. Evolution 57, 1419–1435. https://doi.org/10.1111/j.0014-3820.2003.tb00349.x

Trofimov, B.A., 1977. Primate *Paradolichopithecus sushkini* sp. nov. from the Upper Pliocene of the Pamir Piedmont. Journal of the Paleontological Society of India 20, 26-32.

Tung, J., Barreiro, L.B., 2017. The contribution of admixture to primate evolution. Curr. Opin. Genet. Dev. 47, 61–68. https://doi.org/10.1016/j.gde.2017.08.010

van der Geer, A., Sondaar, P., Dermitzakis, M., 2006. The unique postcranial of the Old World monkey *Paradolichopithecus*: more similar to *Australopithecus* than to baboons. Hell. J. Geosci. 41, 19–28.

Van Dessel, J., Huang, Y., Depypere, M., Rubira-Bullen, I., Maes, F., Jacobs, R., 2013. A comparative evaluation of cone beam CT and micro-CT on trabecular bone structures in the human mandible. Dentomaxillofacial Radiol. 42, 20130145. https://doi.org/10.1259/dmfr.20130145

Van Minh, N., Hamada, Y., 2017. Age-related changes of sulcal imprints on the endocranium in the Japanese macaque *(Macaca fuscata)*. Am. J. Phys. Anthropol. 163, 285–294. https://doi.org/10.1002/ajpa.23205

Van Minh, N., Mouri, T., Hamada, Y., 2015. Aging-related changes in the skulls of Japanese macaques (*Macaca fuscata*). Anthropol. Sci. 123, 107–119. https://doi.org/10.1537/ase.150305

Vásárhelyi, L., Kónya, Z., Kukovecz, Á., Vajtai, R., 2020. Microcomputed tomography–based characterization of advanced materials: a review. Mater. Today Adv. 8, 100084. https://doi.org/10.1016/j.mtadv.2020.100084

Villamil, C.I., 2017. Locomotion and basicranial anatomy in primates and marsupials. J. Hum. Evol. 111, 163–178. https://doi.org/10.1016/j.jhevol.2017.07.003

Visualization Sciences Group, 2011. Avizo® 7.0.0. Berlin, Germany: Konrad-Zuse-Zentrum für Informationstechnik

Weber, G.W., 2015. Virtual Anthropology. American Journal of Physical Anthropology 156, 22–42. https://doi.org/10.1002/ajpa.22658

Wilhelms, J., Van Gelder, A., 1992. Octrees for Faster Isosurface Generation. ACM Trans Graph 11, 201–227. https://doi.org/10.1145/130881.130882

Windsor, R.E., Michaels, M., 2008. CHAPTER 21 - Radiation Safety – Theory and Practical Concerns, in: Slipman, C.W., Derby, R., Simeone, F.A., Mayer, T.G., Chou, L.H., Lenrow, D.A., Abdi, S., Chin, K.R. (Eds.), Interventional Spine. W.B. Saunders, Edinburgh, pp. 229–238. https://doi.org/10.1016/B978-0-7216-2872-1.50026-1

Yu, C., Qin, F., Li, Y., Qin, Z., Norell, M., 2022. CT Segmentation of Dinosaur Fossils by Deep Learning. Front. Earth Sci. 9, 8.

Zilles, K., Palomero-Gallagher, N., Amunts, K., 2013. Development of cortical folding during evolution and ontogeny. Trends Neurosci. 36, 275–284. https://doi.org/10.1016/j.tins.2013.01.006

Zinner, D., Roos, C., 2014. So what is a species anyway? A primatological perspective: So What is a Species Anyway? A Primatological Perspective? Evol. Anthropol. Issues News Rev. 23, 21–23. https://doi.org/10.1002/evan.21390

Zollikofer, C.P.E., Ponce de León, M.S., Lieberman, D.E., Guy, F., Pilbeam, D., Likius, A., Mackaye, H.T., Vignaud, P., Brunet, M., 2005. Virtual cranial reconstruction of *Sahelanthropus tchadensis*. Nature 434, 755–759. https://doi.org/10.1038/nature03397

Zollikofer, C.P.E., Ponce de León, M.S., Martin, R.D., Stucki, P., 1995. Neanderthal computer skulls. Nature 375, 283–285. https://doi.org/10.1038/375283b0

SUPPLAMENTARY MATERIAL

So as not to overload the original manuscript with extensive illustrative material, it has been decided that a supplementary companion to the manuscript shall be provided. Corresponding references cited in the main text follow the scheme *SFig. X*, colored in brown. Figures here are illustrative notices of the models extracted.

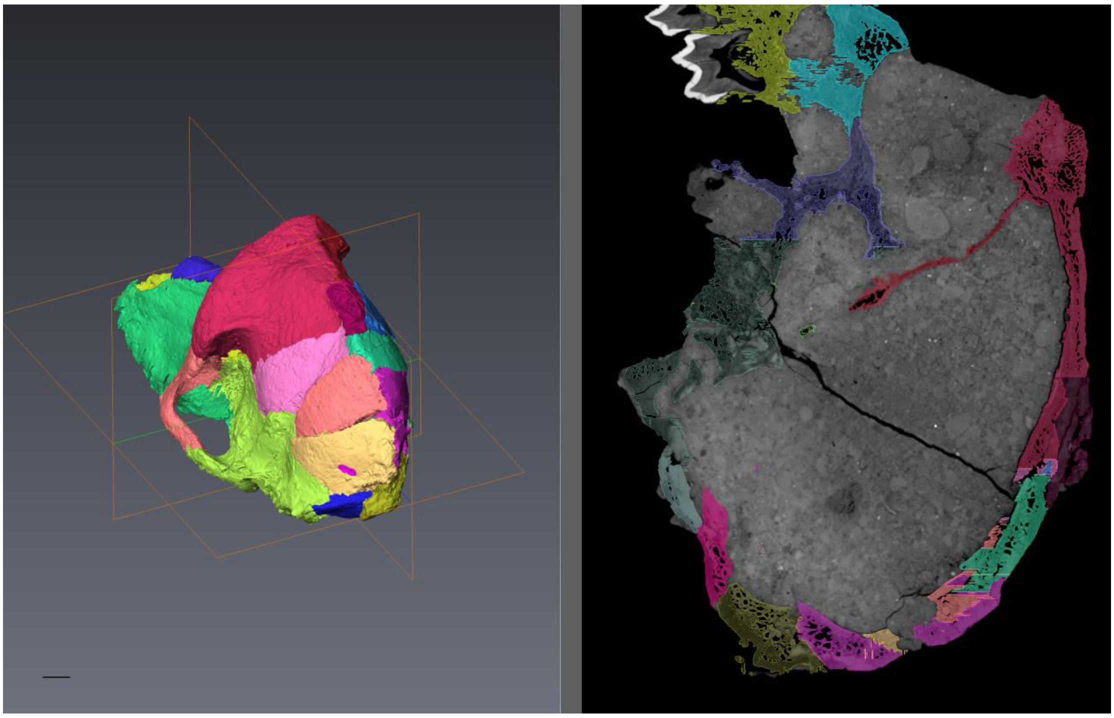

SFigure 1. Fusion of the segments along the neurocranial midsagittal on the original model (left) and an approximate midsagittal labeled CT cross section (right). Oblique left lateral view. Scalebar 1 cm.

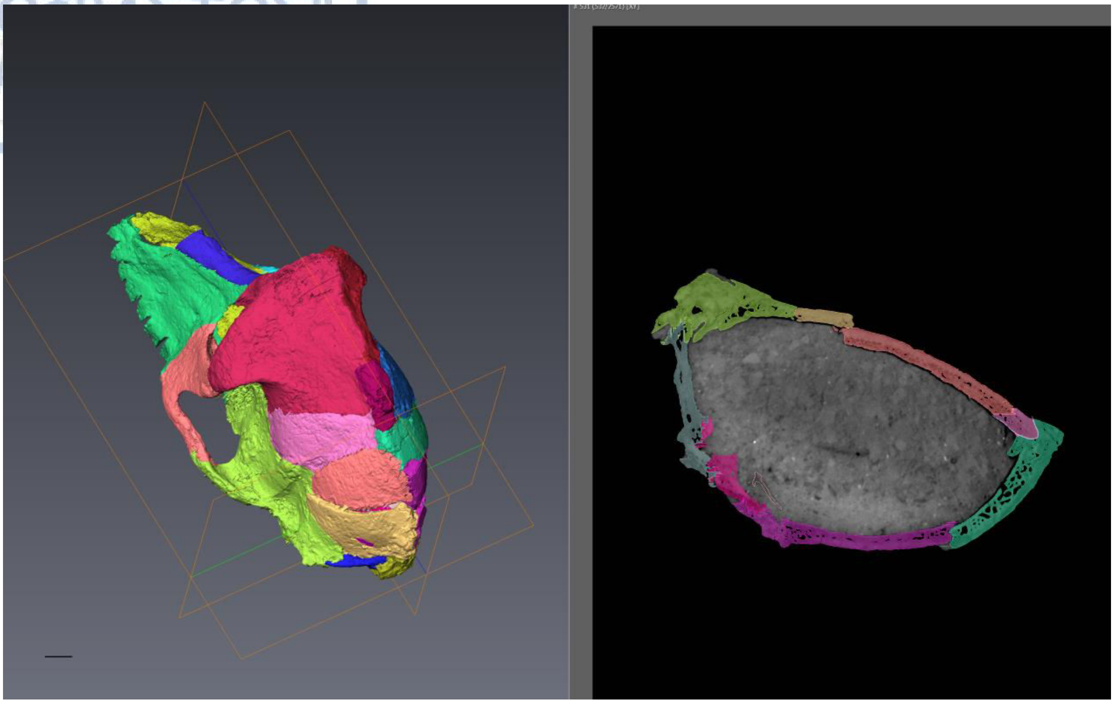

SFigure 2. “Pseudo-crest” as seen in the original model (left) and in a coronal labeled CT cross section (right) depicting the parietals. In right image, dorsal view is rightwards and right lateral view is downwards. Oblique left lateral view. Scalebar 1 cm.

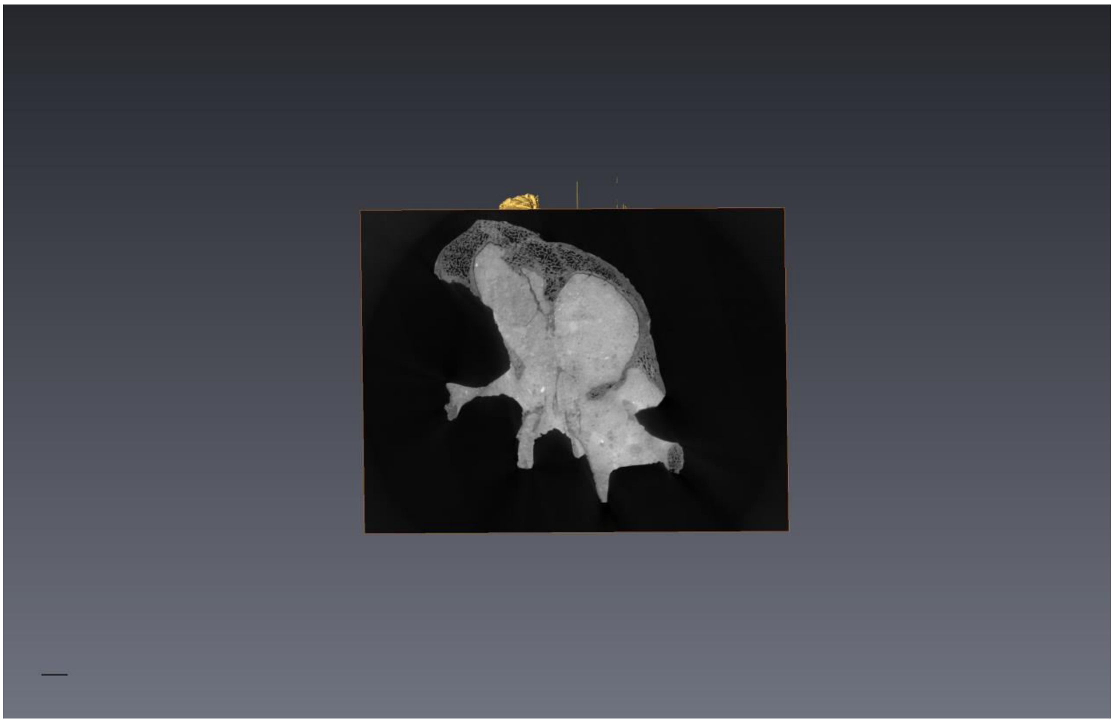

SFigure 3. Coronal CT section passing form left frontomalare tempolare, depicting the thick right frontal on the upper left corner. Frontal view. Scalebar 1 cm.

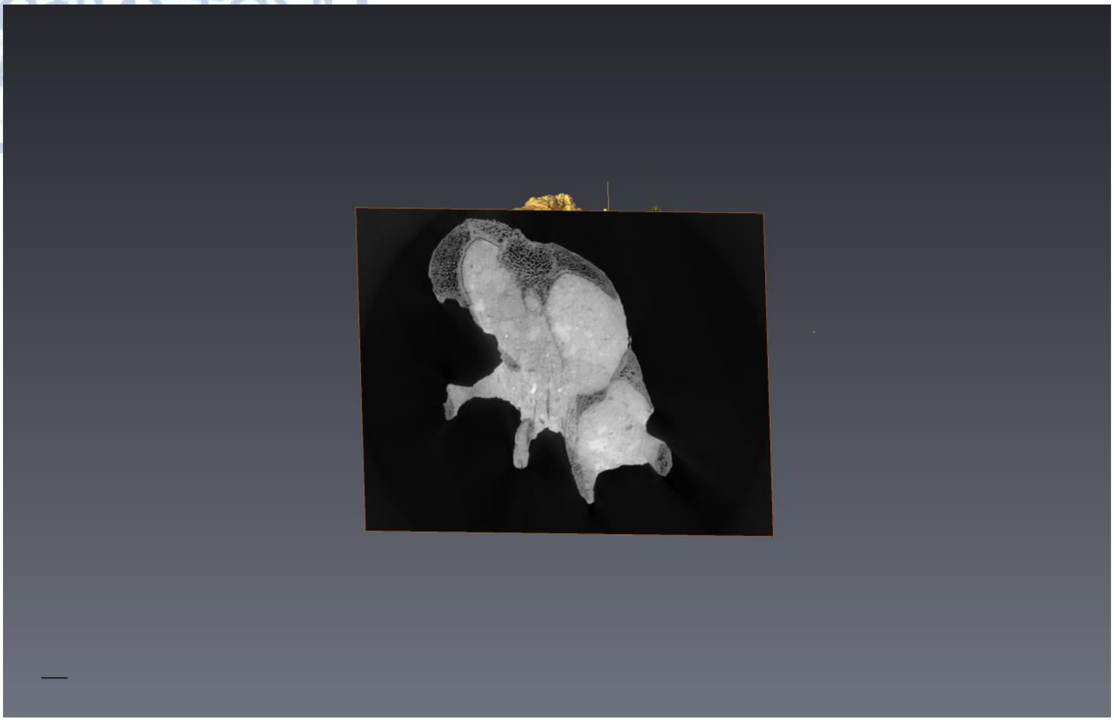

SFigure 4. Coronal CT section passing anterior of left frontomalare orbitale, depicting the “three-fold” structure of the frontal bone. Frontal view. Scalebar 1 cm.

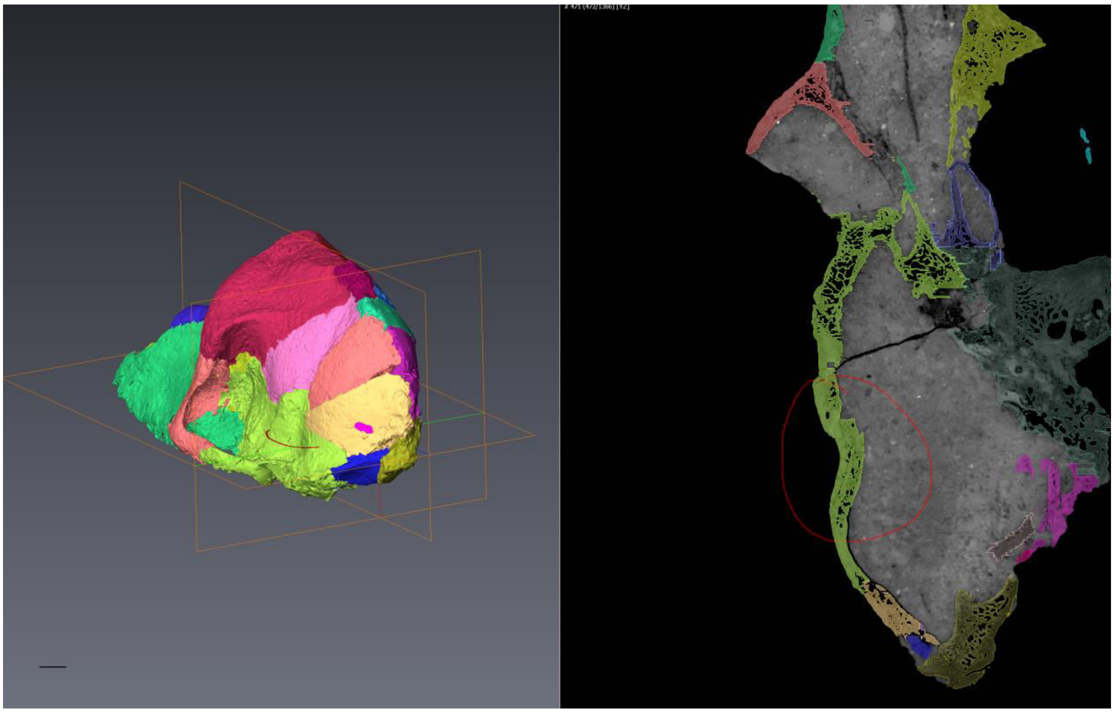

SFigure 5. The “crest” in left temporo-sphenoid segment on the original model (left) and on a labeled horizontal CT cross section (right). Structure on both is marked in red circle. Oblique left lateral view. Scalebar 1 cm.

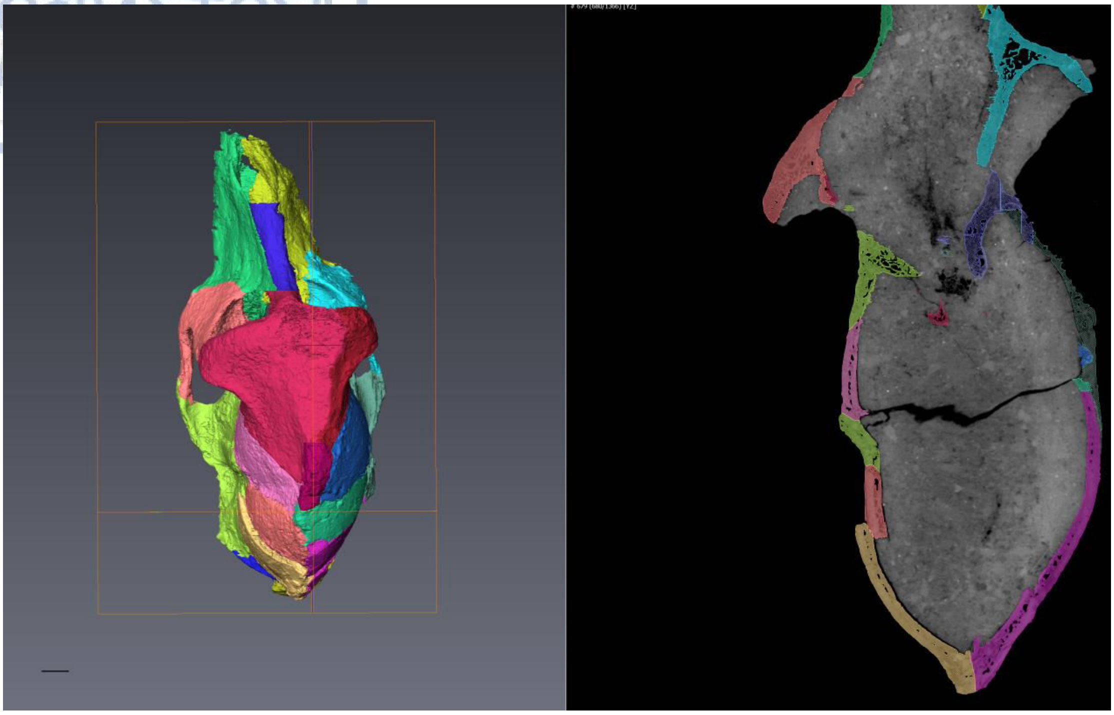

SFigure 6. The “broken” left first parietal fragment, lPar-1 in Table: 1. On the original model (left) and on a labeled horizontal CT cross section (right). Dorsal view. In the cross section anterior is upwards and right lateral is rightwards. Scalebar 1 cm.

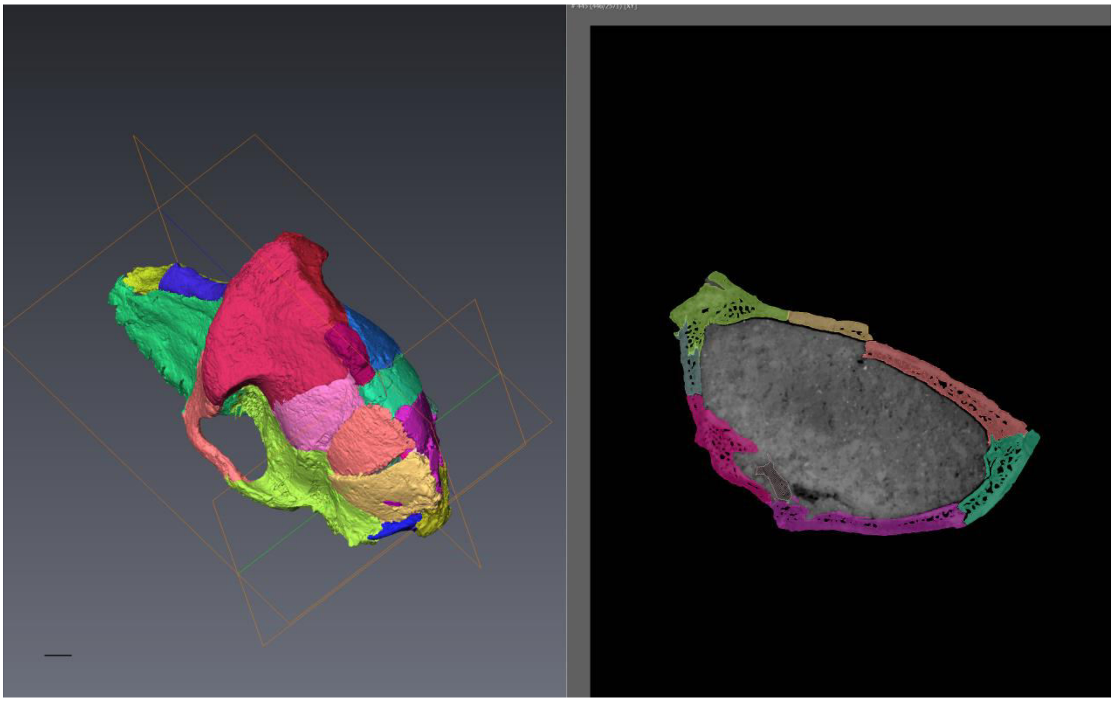

SFigure 7. The “broken” left first parietal fragment, lPar-1 in Table: 1. On the original model (left) and on a labeled coronal CT cross section (right). Oblique left lateral view. In cross section anterior is rightwards and right lateral in downwards. Scalebar 1 cm.

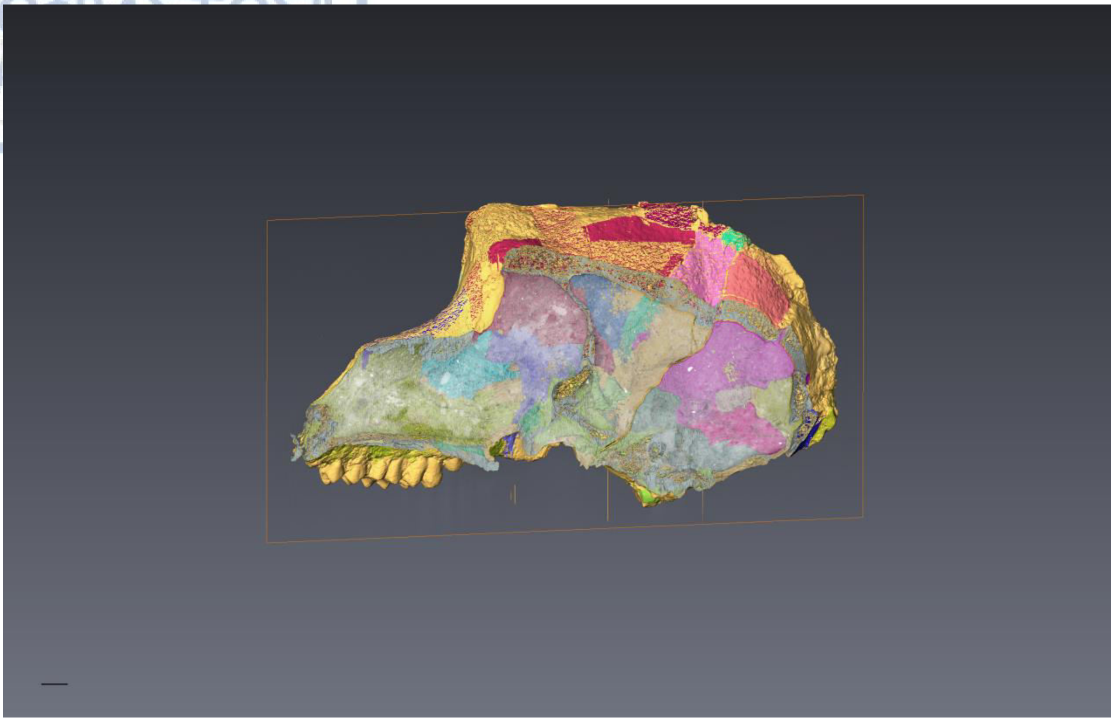

SFigure 8. The great “hemi coronal” crack. Approximately in the middle of the neurocranium is depicted as a “wall”. Left parasagittal CT cross section on both labeled model, isosurface (golden) and CT data (details). Left lateral view. Scalebar 1 cm.

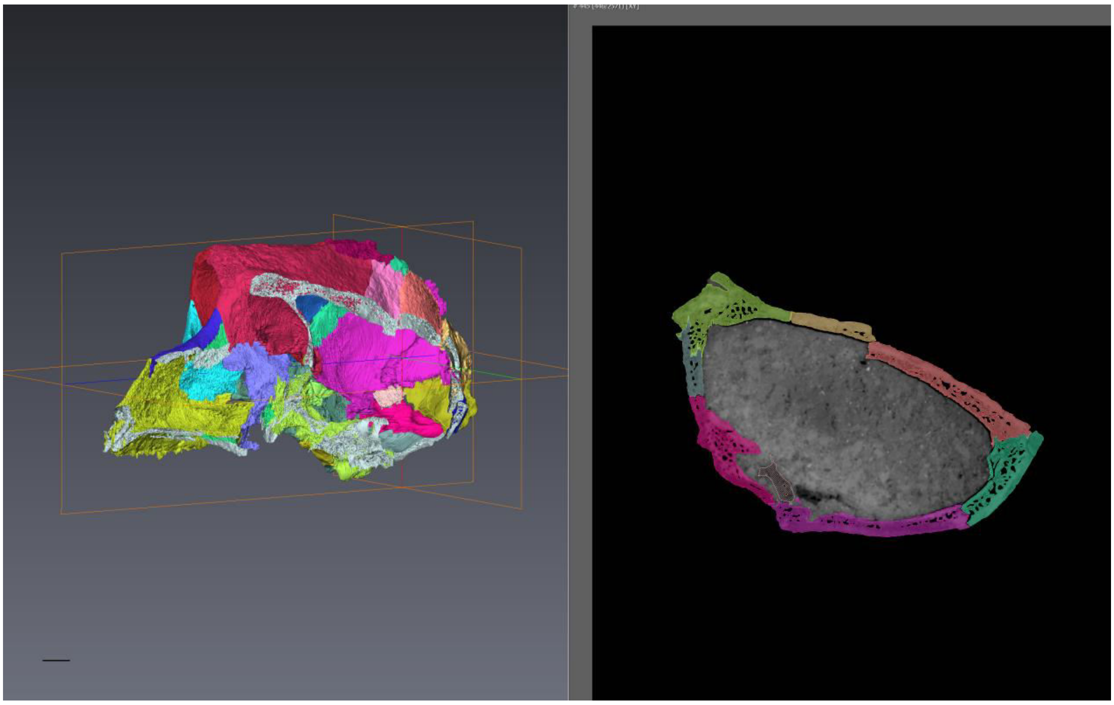

SFigure 9. The inner occipital fragment **Occ-5** (Table 1) in white color as seen in the interior of the neurocranium (left) and in a labeled coronal CT cross section (right). On the right image anterior is rightwards and left lateral side upwards. Scalebar 1 cm.

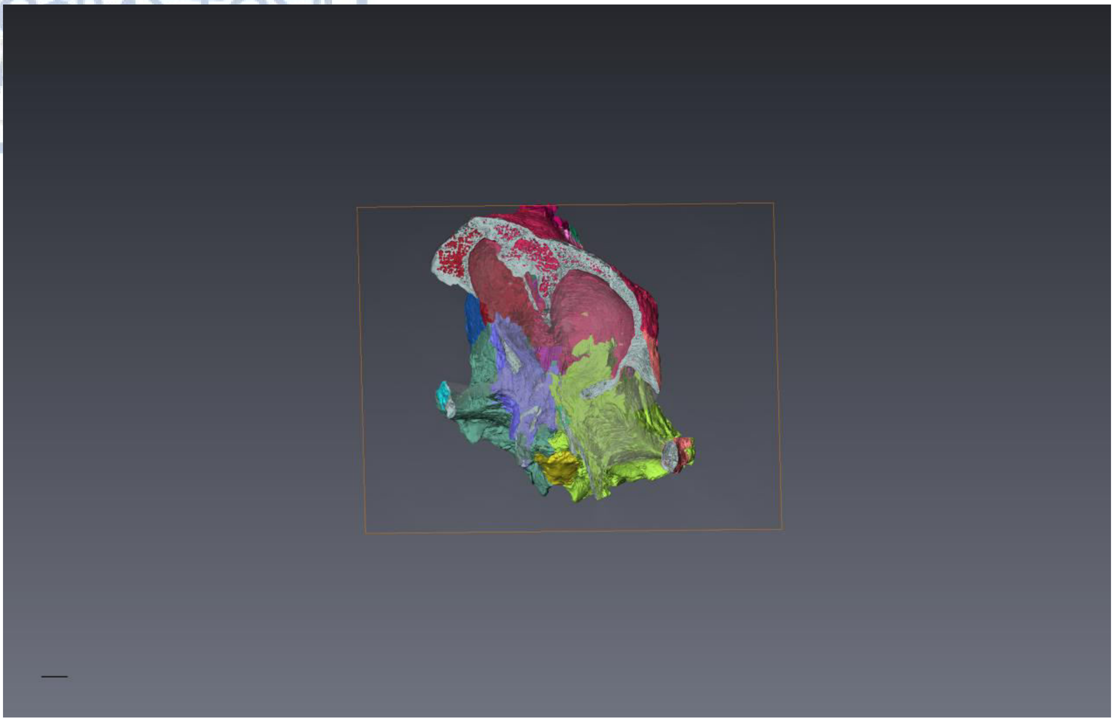

SFigure 10. The ambiguous nature of segmentation with an extreme staircase effect outcome. Coronal plane on original model passing through left frontomalare orbitale. Frontal view. Scalebar 1 cm.

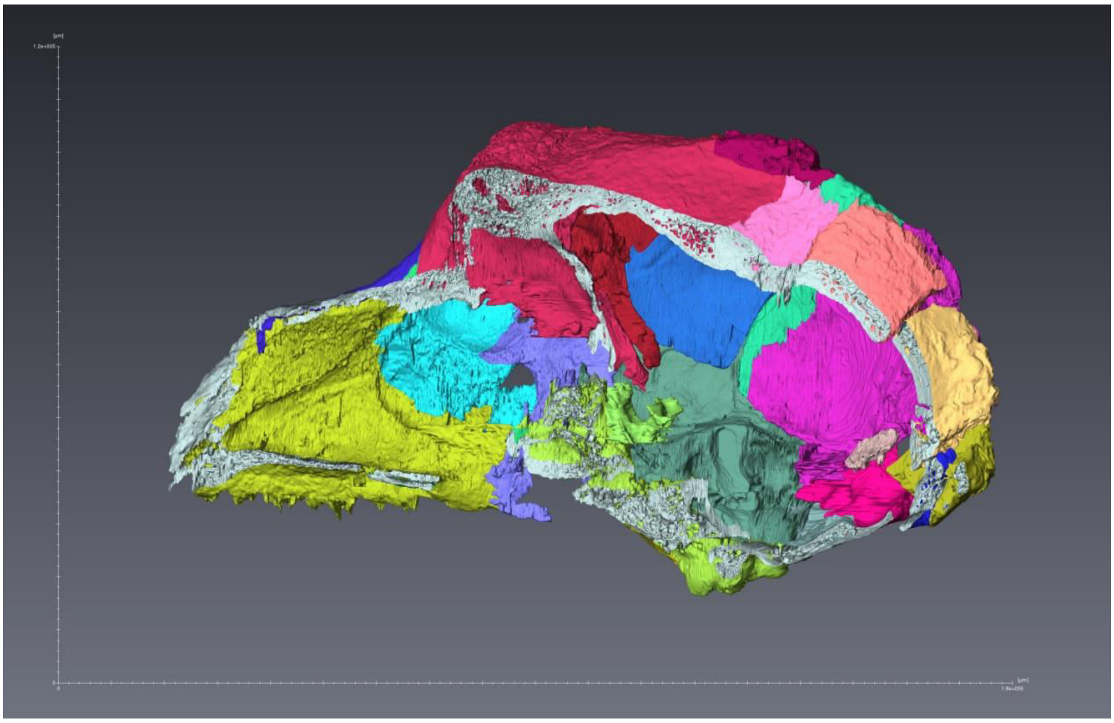

SFigure 11. Sella turcica, (Table 1: **Occ-6**), position in the center of the interior of the cranium. Parasagittal plane on the original model. Left lateral side. Scalebar 12*18 cm.

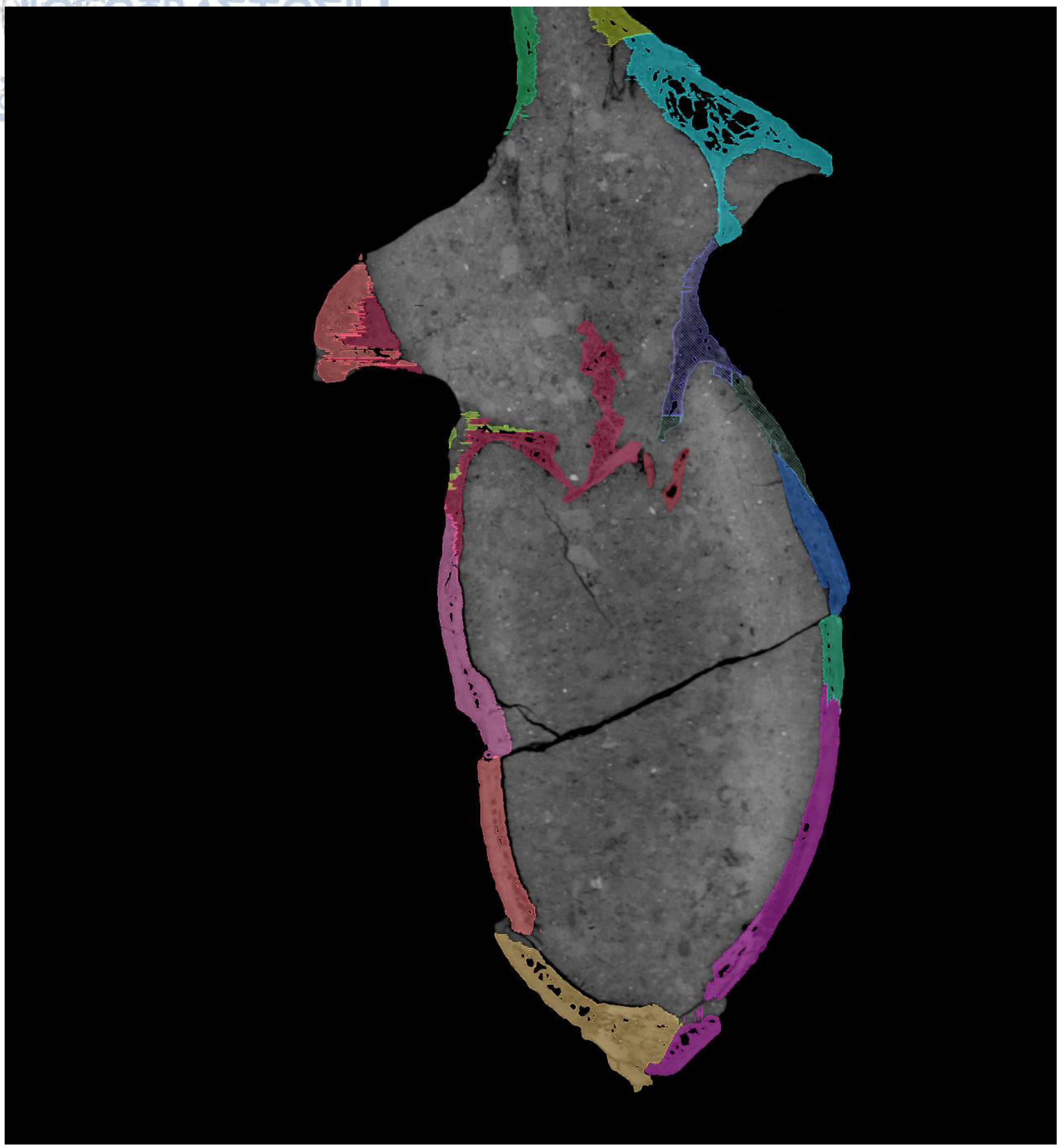

SFigure 12. The globular contour of neurocranium on the right lateral side in comparison to the fragmented left of the neurocranium. Labeled horizontal CT cross section passing through left pterion. Dorsal view.

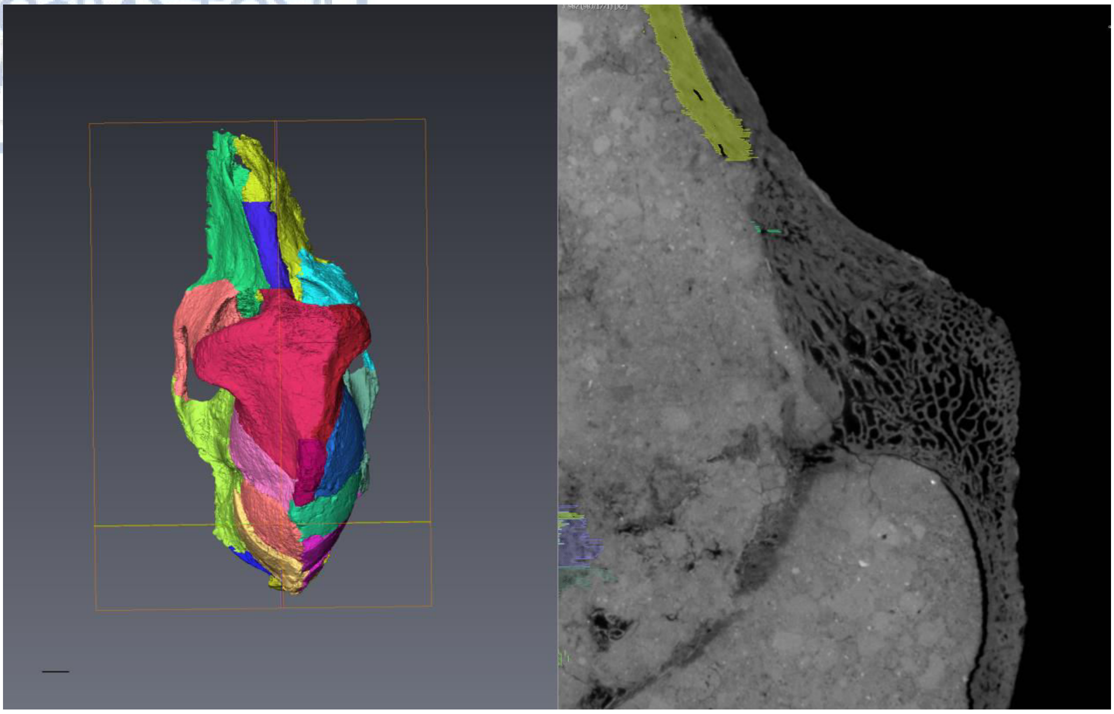

SFigure 13. Diploe transition in Fronto-nasal region as seen on the original model (left) and on a labeled left parasagittal CT cross section. Left image in dorsal view. Scalebar 1 cm.

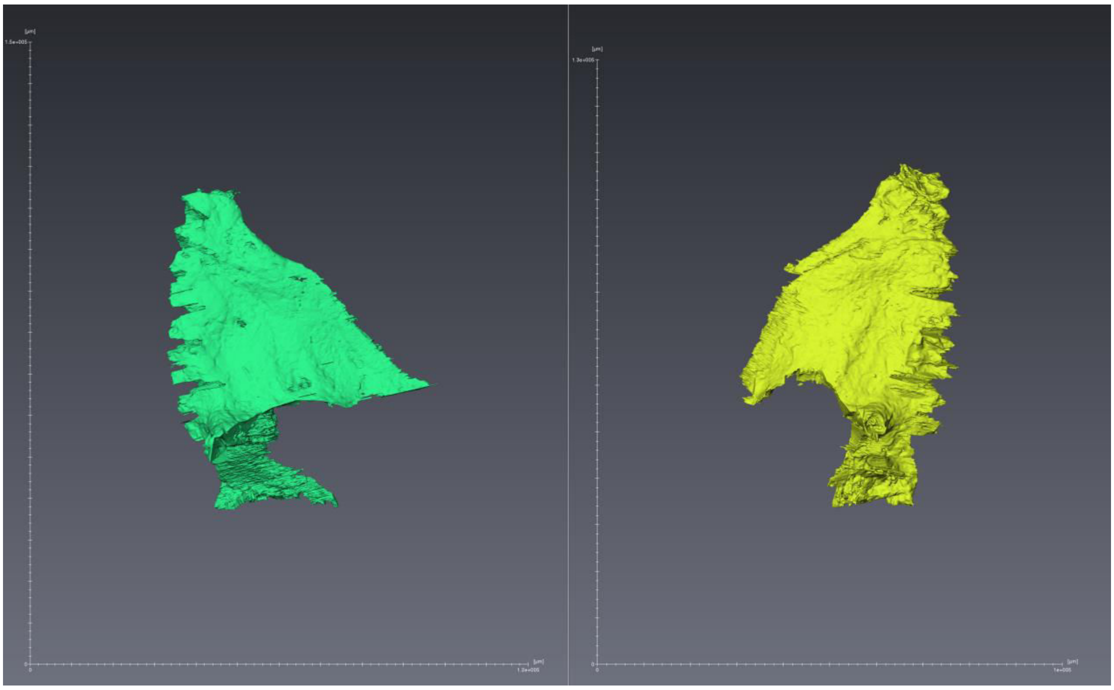

SFigure 14. Left and right maxillae of DFN3-150 original model respectively. Oblique left lateral views. Scalebar 15*12 cm (left), 13*12 cm (right).

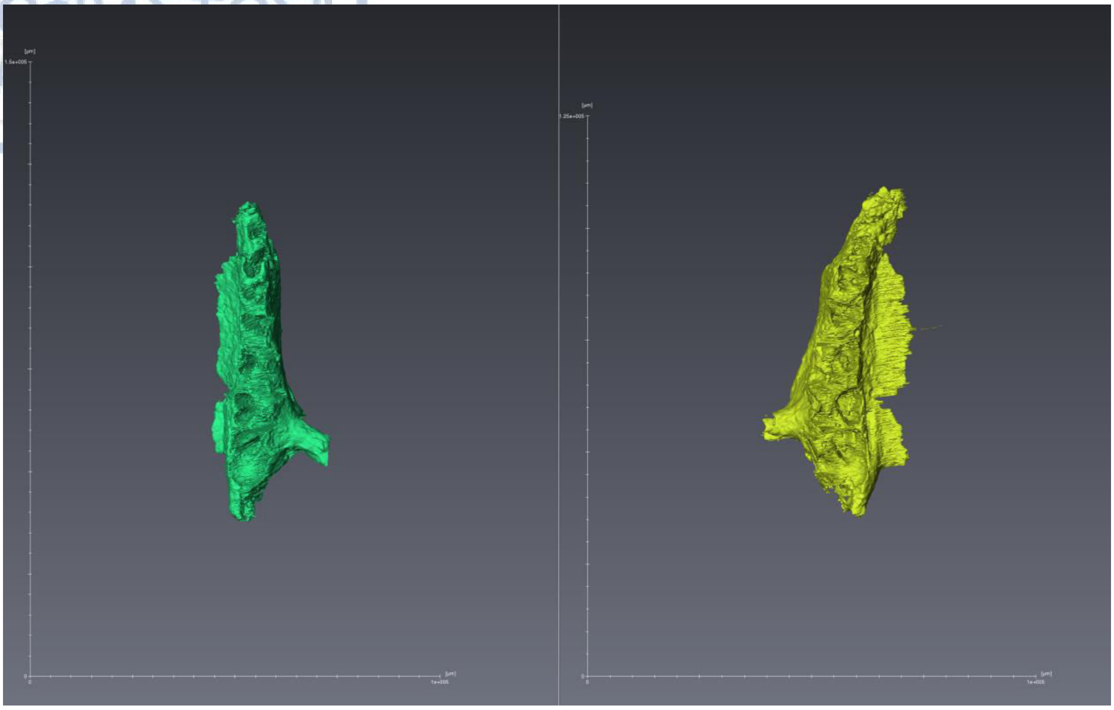

SFigure 15. Left and right maxillae of DFN3-150 original model respectively. Oblique occlusal views. Scalebar 15*10 cm (left). 12.5*10 cm (right).

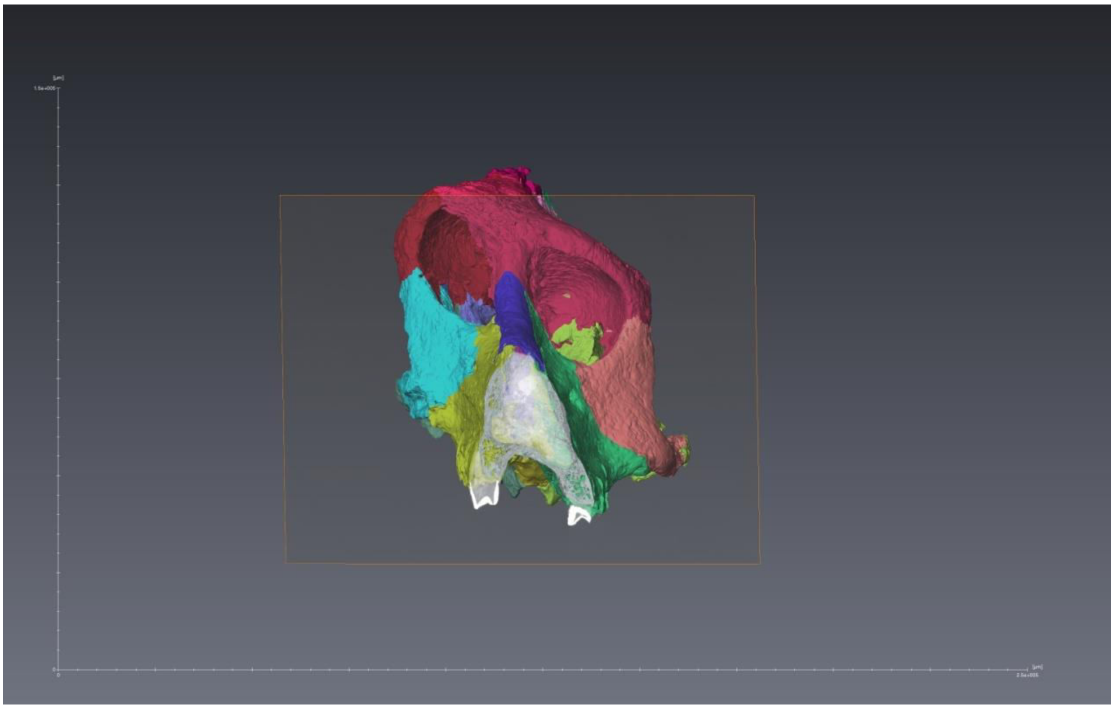

SFigure 16. The palatal overlap at the level of messial left P4. Labeled coronal cross section on the original model with CT data superimposed (blurred). Frontal view. Scalebar 15*25 cm.

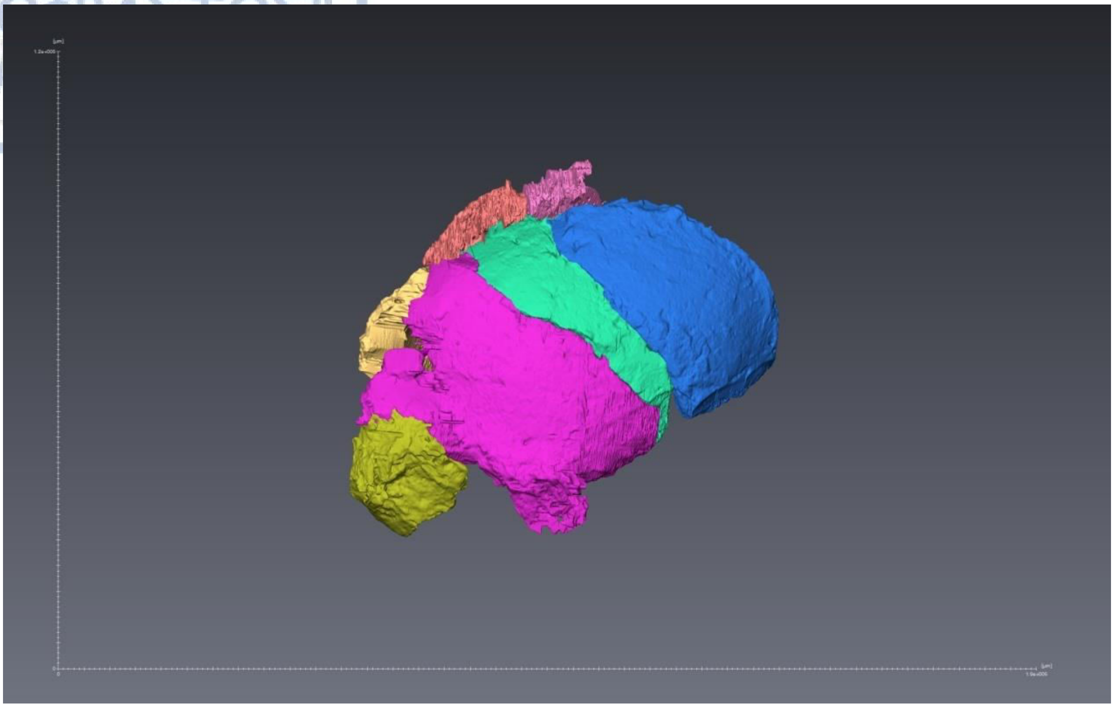

SFigure 17. The exposed view of the left parietals in *Model 1a* in relation to the right ones. Oblique right lateral view. Scalebar 12*19 cm.

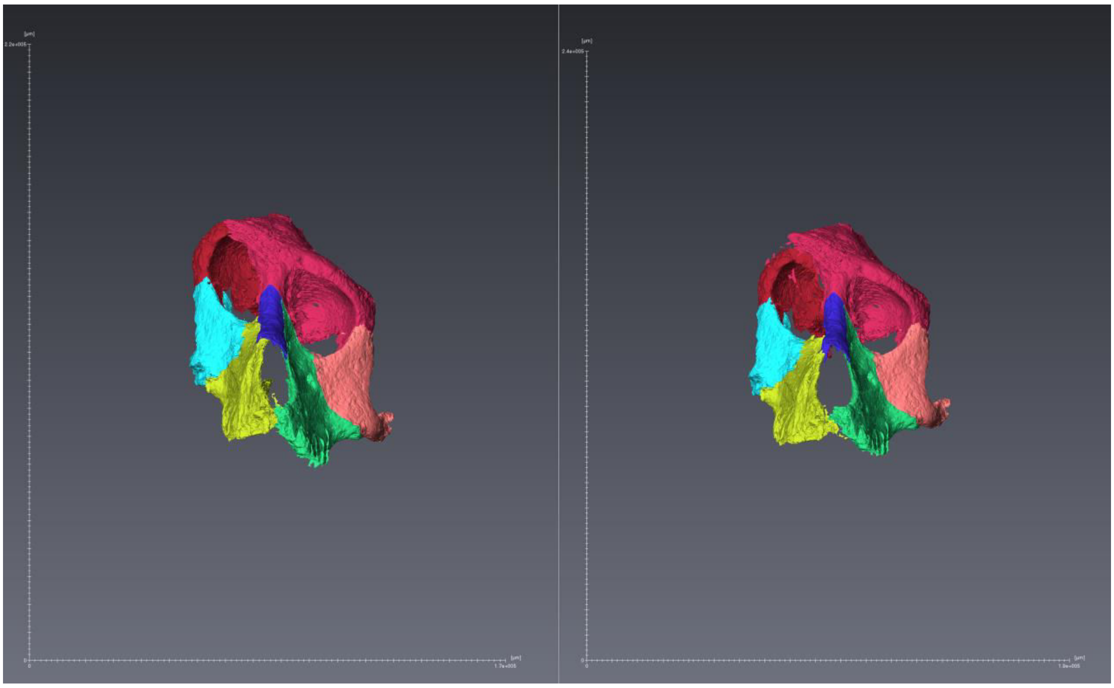

SFigure 18. Comparison between the original model (left) and *Model 1a* (right). Frontal views. Scalebar 22*17 cm (left), 24*19 cm (right).

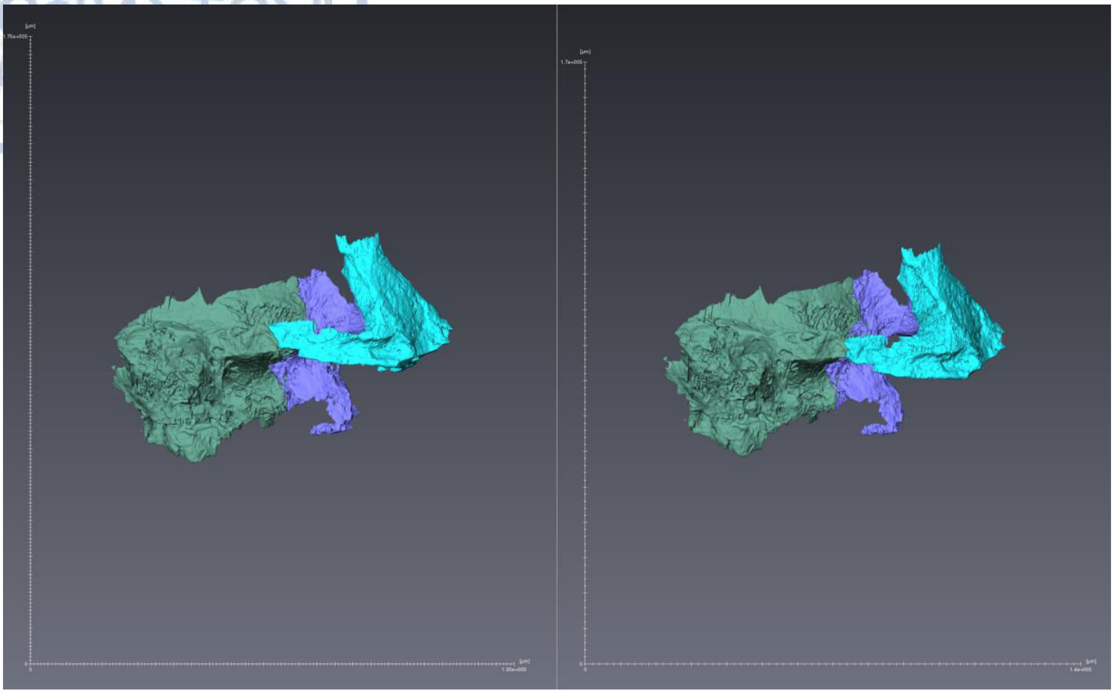

SFigure 19. The disposition of the zygomaticotemporal suture. Comparison between the original model (left) and *Model 1a* (right). Right lateral views. Scalebar 17.5*13.5 cm (left), 17*14 cm (right).

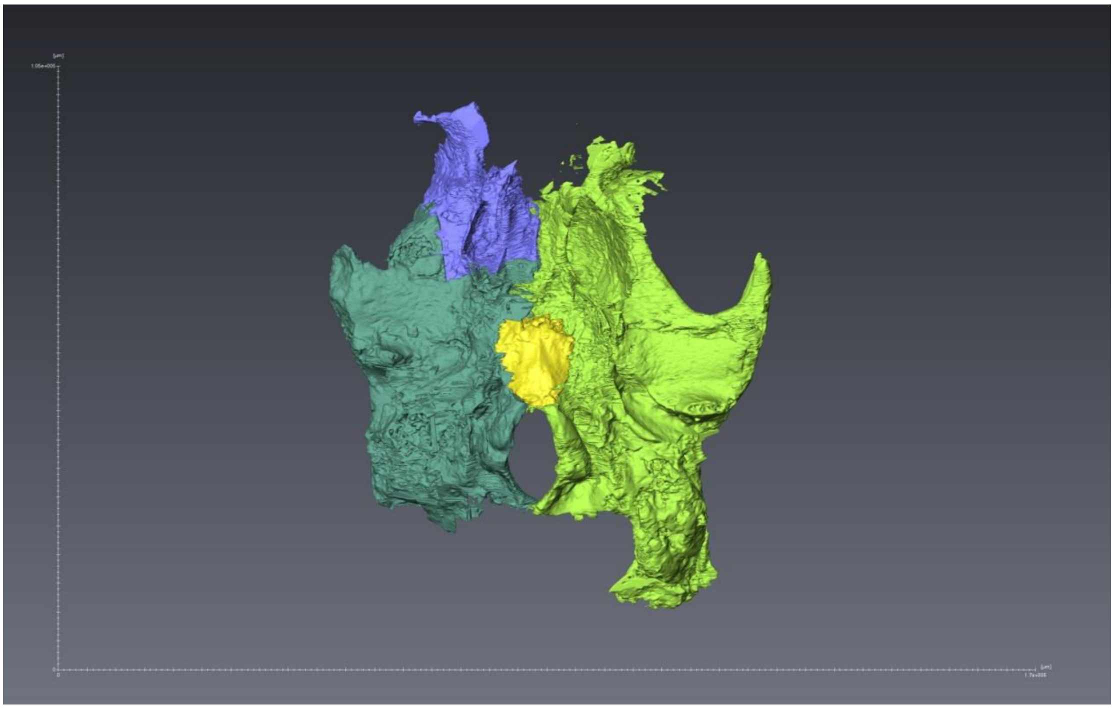

SFigure 20. The “crest” of the pars basilaris of the occipital in the original model. Ventral view. Anterior is upwards. Scalebar 10.5*17 cm.

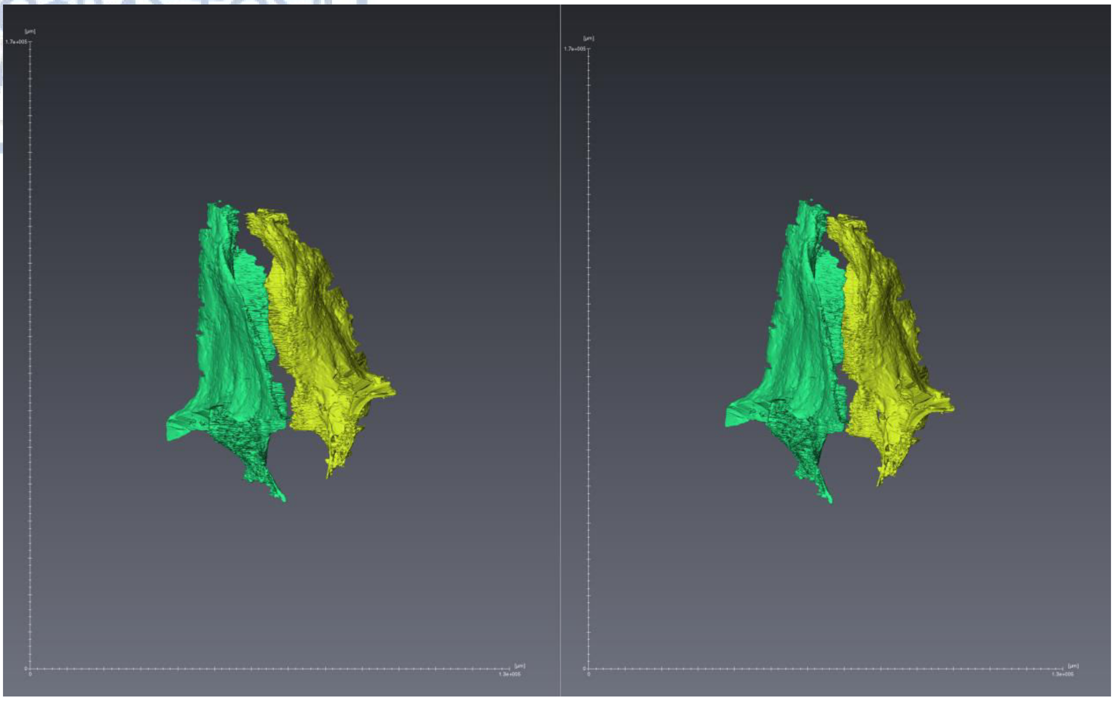

SFigure 21. Comparison of the muzzle between *Model 1a* (left) and *Model 1b* (right). Dorsal views. Scalebar 17*13 cm.

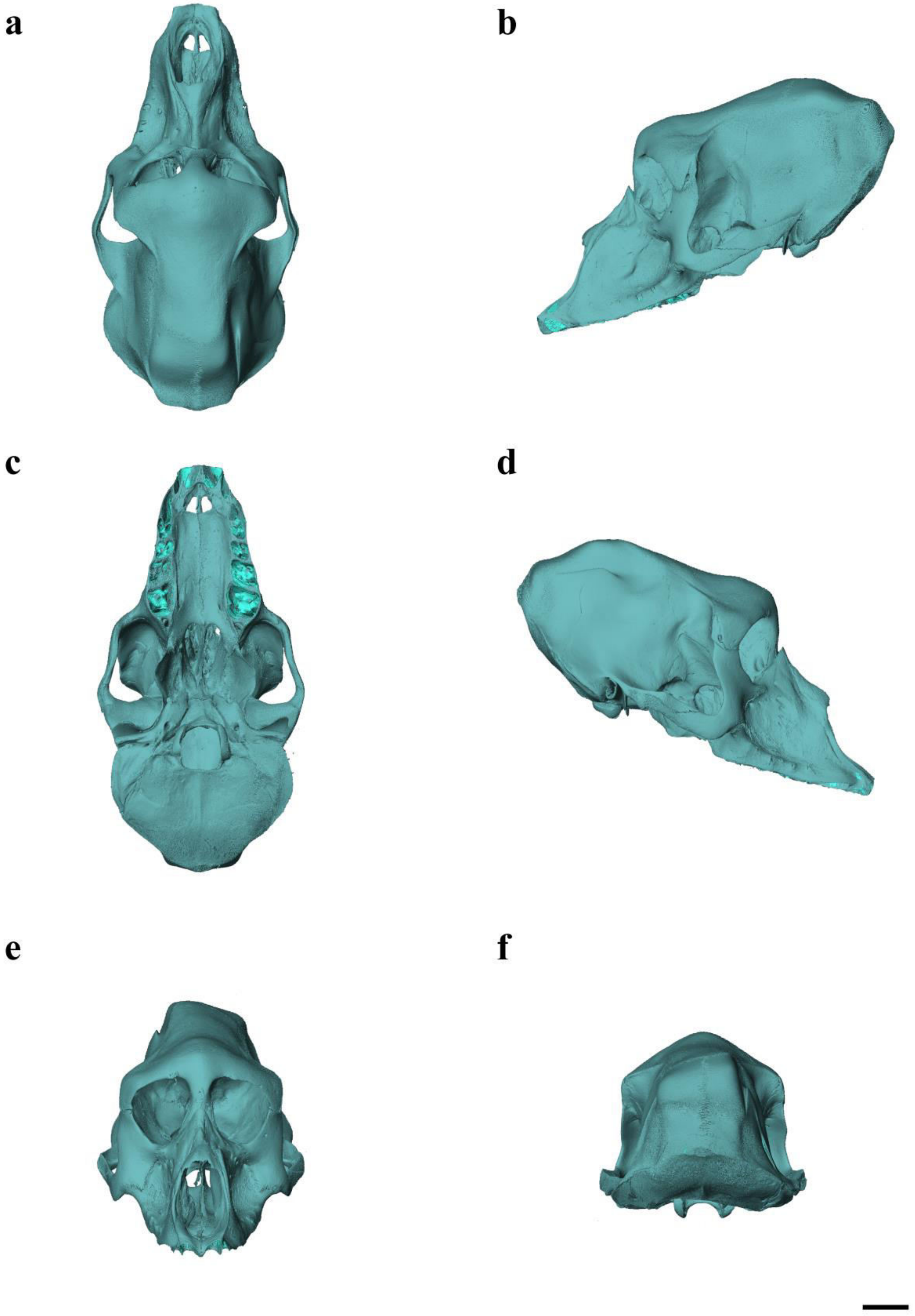

SFigure 22. The *Papio anubis* specimen after taking the shape of LGUPT DFN3-150 cranium in dorsal (a), left lateral (b), ventral (c), right lateral (d), frontal (e) and posterior (f) view. Scalebar 2 cm.

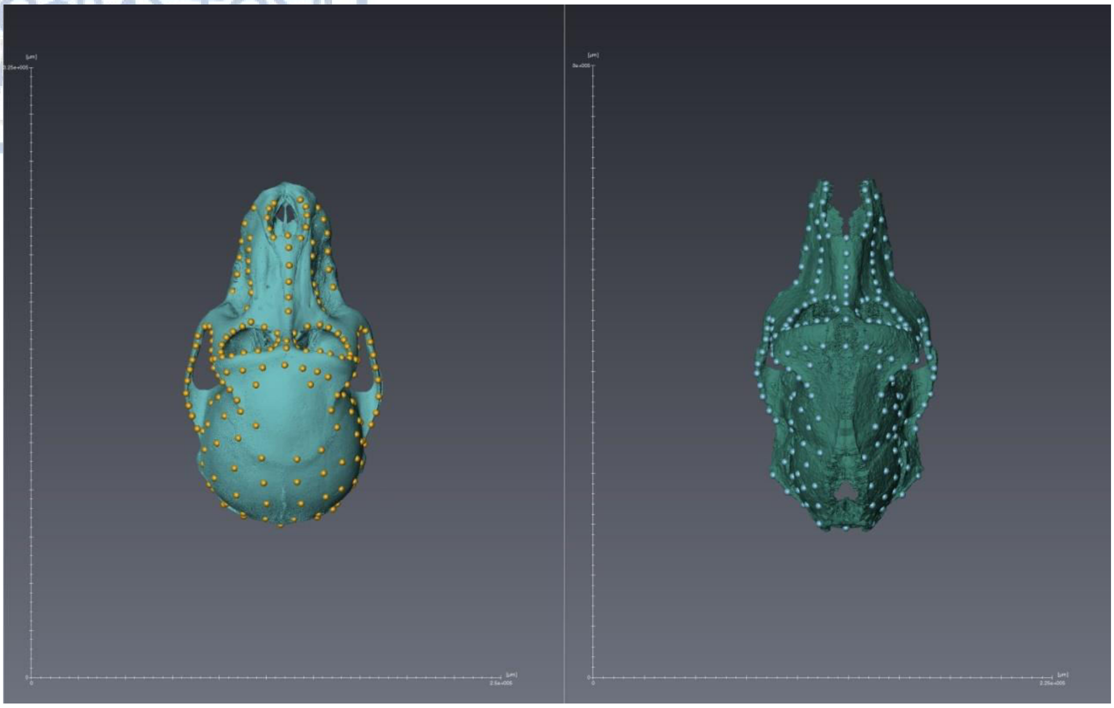

SFigure 23. Anatomical and surface landmarks applied on both extant *Papio anubis* (left) and *Model 2* of LGPUT DFN3-150 (right) crania. Dorsal views. Scalebar 32.5*25 cm (left), 30*22.5 cm (right).

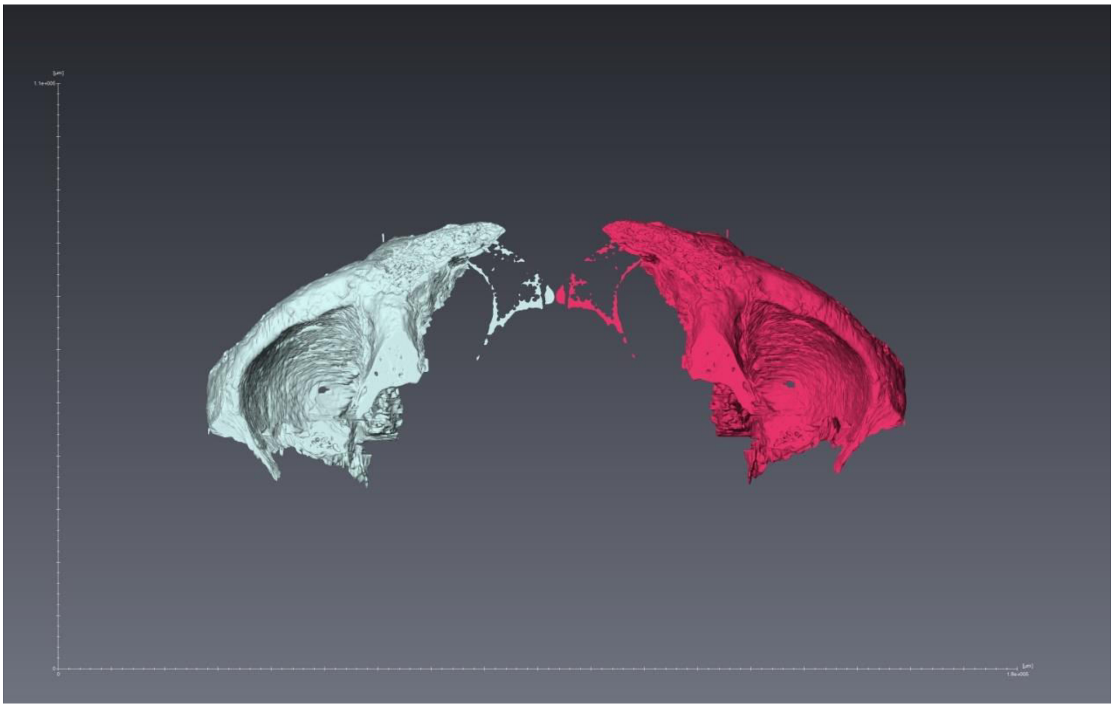

SFigure 24. The left frontal fragment and its mirrored counter frangment. Frontal views. Scalebar 11*18 cm.

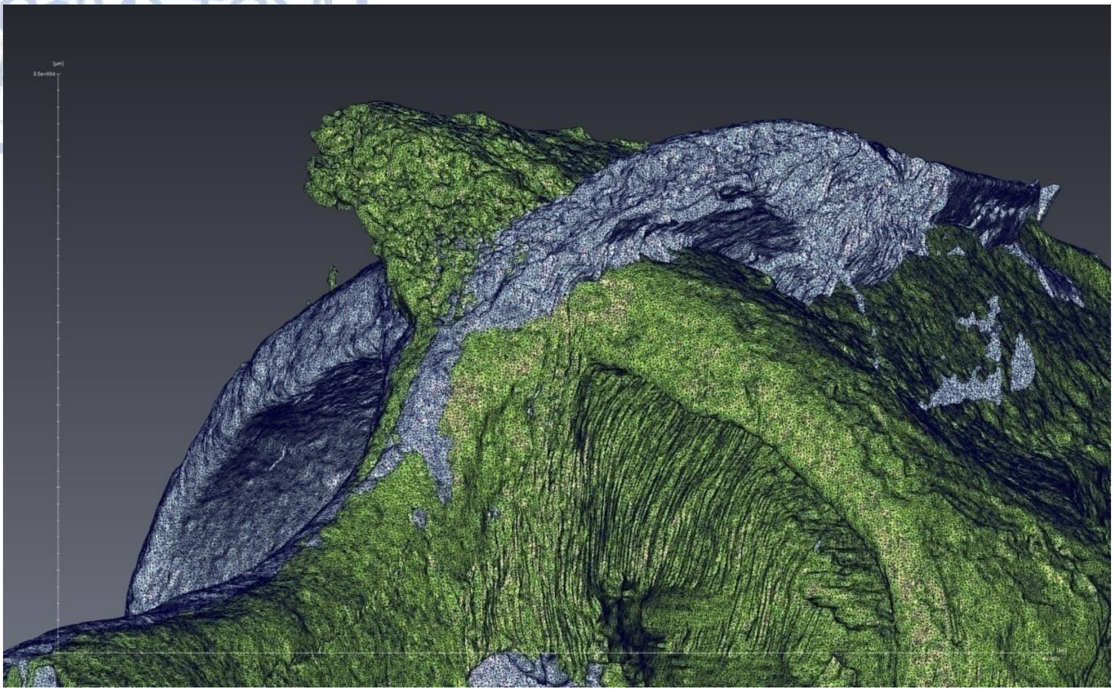

SFigure 25. The mirrored torus with the protruding parts of both frontals. Later modified as in Fig. 11 in the main text. Oblique frontal view. Left bilateral side is in greenish yellow. Scalebar 3.5*6 cm.

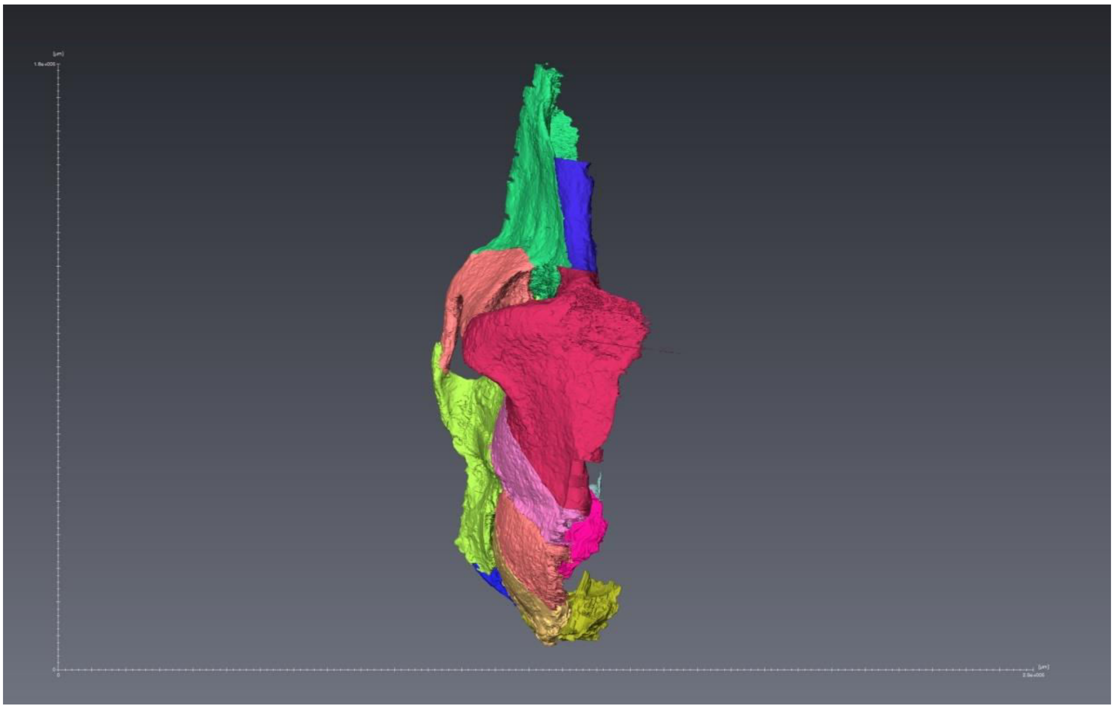

SFigure 26. The left bilateral side configuration used in *Model 2* mirror imaging. Dorsal view. Scalebar 18*29 cm.

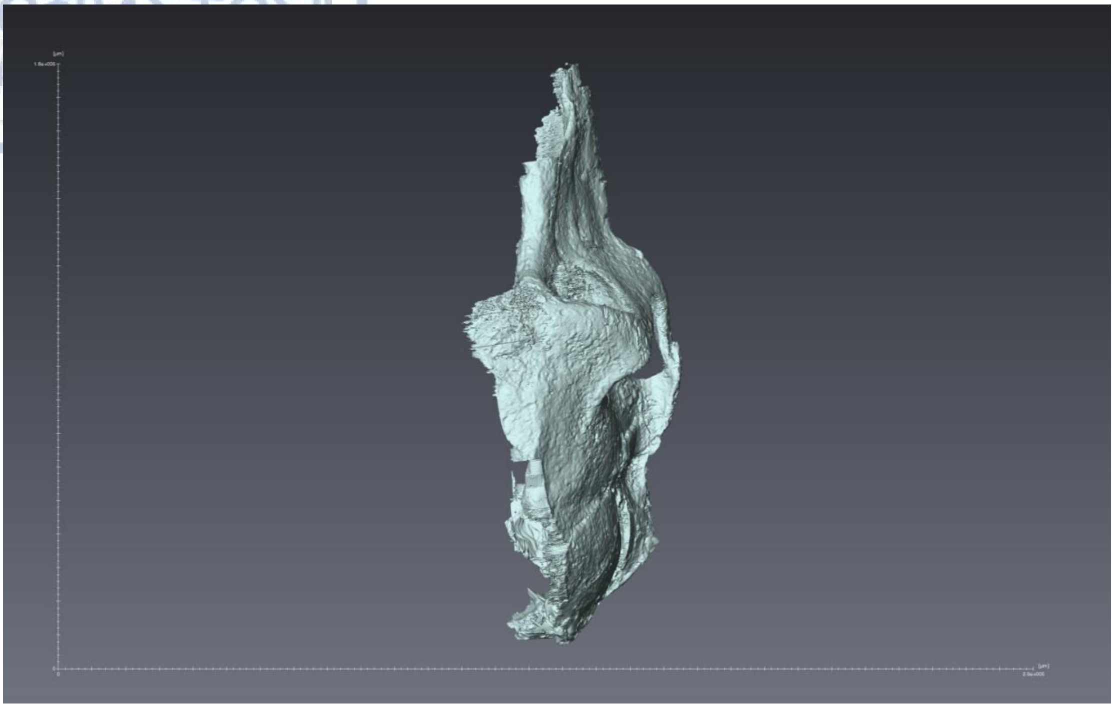

SFigure 27. Each mirrored fragment is manipulated independently so as to fit in the acquired position of the mirrored frontal. Right bilateral mirrored side. Dorsal view. Scalebar 18*29 cm.

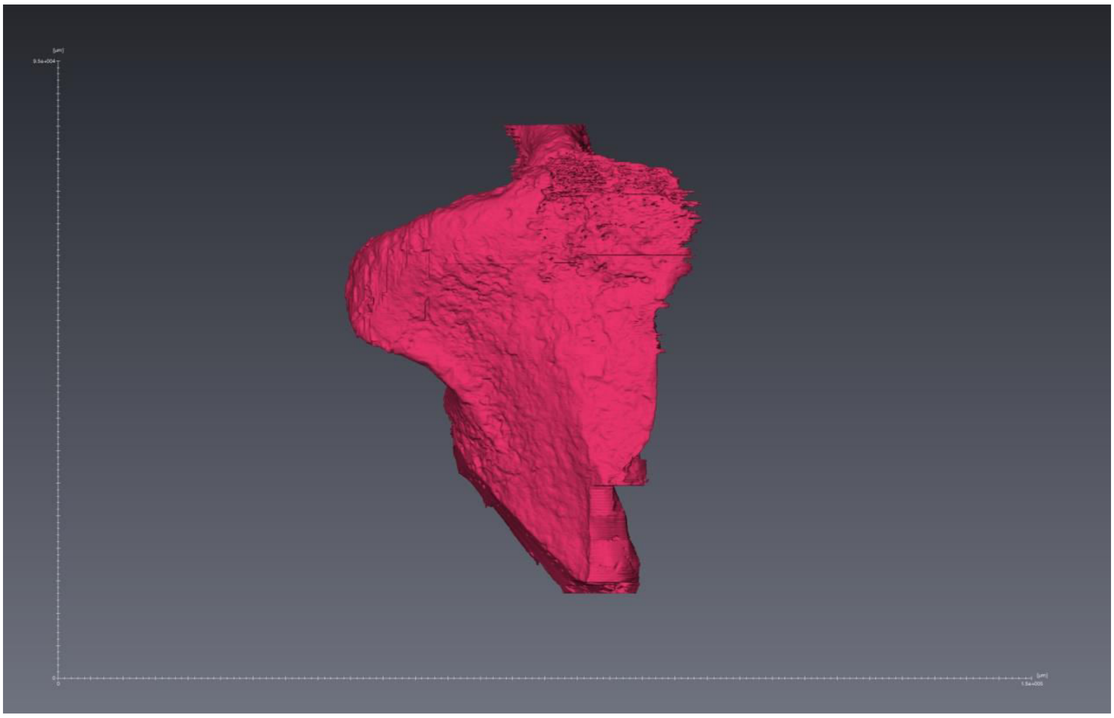

SFigure 28. The left frontal segment and its post torus shape affecting the outcome of mirror imaging creating a new pseudocrest. Dorsal view. Anterior is upwards. Scalebar 9.5*15 cm.

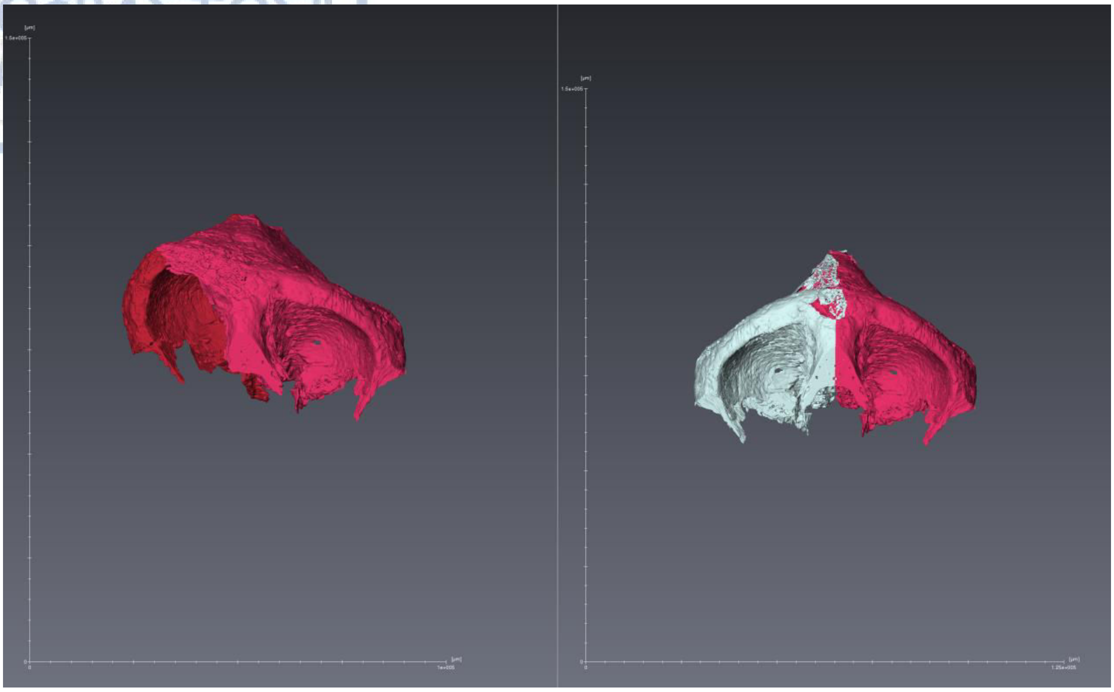

SFigure 29. The contour difference in the supraorbital torus between original (left) and *Model 2* (right) specimens. Frontal views. Scalebar 15*10 cm (left), 15*12.5 cm (right).

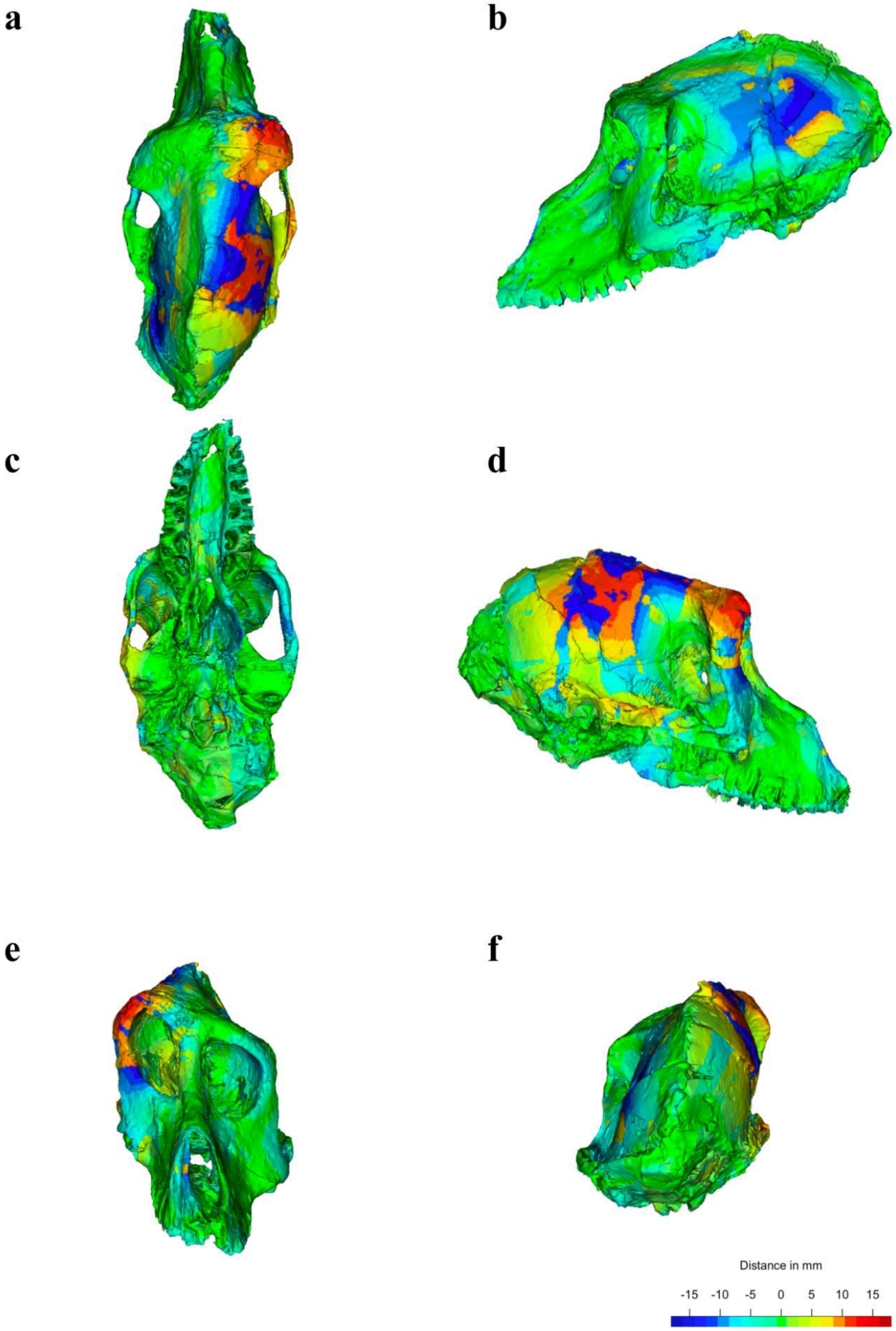

SFigure 30. Vertex-map describing shape differences between the original specimen DFN3-150 and *Model 2*. Provided by Carolin Röding, M.Sc. Differences over exceeding 18 mm are not depicted. Unscaled.